The Dissertation Committee for Liu Wang certifies that this is the approved version of the following dissertation:

Mechanics of Crater-Enabled Dry Adhesives

Committee:

Nanshu Lu, Supervisor

Gregory J. Rodin

Kenneth M. Liechti

K. Ravi-Chandar

Roger T. Bonnecaze

Mechanics of Crater-Enabled Dry Adhesives

by

Liu Wang

Dissertation

Presented to the Faculty of the Graduate School of

The University of Texas at Austin

in Partial Fulfillment

of the Requirements

for the Degree of

Doctor of Philosophy

The University of Texas at Austin

May 2019

Dedicated to my family.

Acknowledgements

I would like to convey my sincere thanks and appreciation to my advisor, Prof. Nanshu Lu, for her professional guidance and financial support in the last five years. Prof. Lu is a dedicated mentor with great patience, who instills into me a love of learning. She is a visionary professor with invaluable resourcefulness, who ignites my creative imagination. She is also a self-assured scholar with sheer enthusiasm, who always encourages me to move forward with confidence.

Great thanks are owed to Professors Gregory J. Rodin, Kenneth M. Liechti, K. Ravi-Chandar and Roger T. Bonnecaze for serving my dissertation committee. Now I should thank Prof. Rodin and Liechti again for the in-depth discussions with them during weekly meetings on the crater project. Their "harsh" questions sometimes really embarrassed me but indeed turned out to deepen my understanding afterward.

I should also appreciate the opportunities of taking courses lectured by Professor Stelios Kyriakides, Thomas J. Hughes, Gregory J. Rodin, Mark E. Mear, Kenneth M. Liechti, Chad M. Landis, Rui Huang, Nanshu Lu, and S. A. Kinnas, whose broad knowledge has helped me form a solid foundation for my research.

I would like to send my special thanks to my big brothers Dr. Shixuan Yang, Dr. Shutao Qiao, and Dr. Dongjie Jiang for helping me set down when I came to UT Austin in Fall 2014. They also assisted me in the finite element simulations in my research. In particular, Dr. Dongjie Jiang served as my teaching assistant twice, from whom I have learned a lot.

I also want to thank all members in Prof. Lu's research group. First, Daniel A Sanchez, who is actually the most "senior" member as he joined the group when he was still an undergrad, taught me numerous expressions in English. I bet he may also witness

my progress in oral presentation. Second, I should say thanks to Korean friends Dr. Taewoo Ha, Hyoyoung Jeong, Kyoung-Ho Ha, and Hongwoo Jang. It is great fun to learn Korean phrases from you! Also, I would thank Siyi Liu, Zhaohe Dai, Xiangxing Yang, for the "happy" E-sport hours.

Last but not least, thank all the friends in Austin, in particular, Chenglin Yang, Kelin Chen, Yu-sheng Lo, Si Chen, Yifu Huang, Yifan Rao, Chen Chen, Tianhao Yang, for the joy and fun with you all.

Financial support for this dissertation from the US National Science Foundation (Grant No. 1301335 and 1663551) and Office of Naval Research (Grant No. N00014-16-2044) is highly appreciated.

Mechanics of Crater-Enabled Dry Adhesives

Liu Wang, Ph.D.

The University of Texas at Austin, 2019

Supervisor: Nanshu Lu

Soft adhesives that can attach to three-dimensional curvilinear surfaces historically have gained a myriad of attention from both scientific and technological perspectives. The rapid advances of bio-integrated devices in recent decades further led to a wealth of research in strategically designing soft adhesives with not only strong bonding capability but also easy-to-detach and reusable merits. The robust conformal contact, nondestructive debonding, and non-degrading repeatability together rule out the employment of chemical-based bonding agent, giving rise to a flurry of study on adhesives solely enabled by van der Waals (vdW) forces and/or suction effect, a.k.a. *dry adhesives*. In this dissertation, I first established an analytical framework for predicting the contact status of a thin elastic membrane conforming to a soft and rough substrate assuming vdW membrane/substrate interaction. Utilizing energy minimization method, I successfully predicted the fully conformed, partially conformed and non-conformed contact results, as validated by experimental observations. It was found that vdW adhesion alone is relatively weak to secure a conformal contact with rough substrates, especially when the system is subjected to external compressive strain. To enhance the interfacial adhesion, polymer surface engineered with concave domes, termed craters, recently emerges as a new type of dry adhesive. To quantitatively reveal adhesion mechanism in a cratered surface, I established a nonlinear elasticity framework for modeling the suction generation through an idealized loading-unloading process. Material properties, crater shape, air vs. liquid ambient, surface

patterns and preloads are systematically investigated using finite element simulation and/or experimental approaches. The optimal topographical feathers of cratered surfaces with highest suction effect have been discovered. This dissertation offers an outlook for future research directions on crater-enabled dry adhesives.

Table of Contents

List of Figures

Chapter 1 Introduction

Conformable electronics that can adapt to curvilinear surfaces represent the next-generation of dynamically malleable microelectronics. Recent advancement of material design, structural optimization, and fabrication techniques have significantly boosted its prosperity in various applications. In this chapter, we offer a mini state-of-the-art review of conformable electronics, followed by an emerging assembly strategy of utilizing soft dry adhesives. Free of chemical bonding agent, dry adhesives are capable of providing strong yet reversible adhesive force, allowing for remarkable conformability and biocompatibility of the conformable electronics.

1.1 CONFORMABLE ELECTRONICS

Conventional electronics are manufactured on two-dimensional (2D) planar and rigid substrates such as silicon wafers, which are intrinsically incompatible with three-dimensional (3D) curvilinear surfaces. This conflict becomes more conspicuous when the surface is dynamically deformable, e.g., the surface of living organisms. Driven by the enormous demand for innovative characteristics and integrated multifunctionalities, conformable electronics that can accommodate 3D complex surfaces have been garnering substantial interests in recent decades. A variety of potential applications for sensory systems such as morphing aircraft monitoring, healthcare diagnostics, and electronics skin (E-skin) have already been demonstrated. For example, utilizing aerosol jet printing, Paulsen *et al* directly printed electronic circuits onto the 3D rigid surface with sharp edges [1]. Such 3D conformal sensors and antennas, known as stereo circuits, can be employed on aircraft wings or fuselages for defect detection, which used to be unmeasurable for lack of curvilinear sensors or circuitry [2]. The epidermal electronics [3-6] and smart implants [7-9] recently have emerged as promising medical devices for both vital signal monitoring and therapeutic purposes. Emulating the perceptions of human skin, E-skin with tactile sensors wrapped on robotics fingers is capable of identifying pressure, temperature, moisture and so on [10-12]. When equipped on prosthetic hands, such E-skin can receive external stimuli during daily activities while simultaneously replicating realistic appearance and physical properties to help hand amputees integrate into social contexts naturally [13, 14]. Aside from basic sensing function, unconventional materials such as InGaZnO [15], graphene [6, 16], quantum dots [17], liquid metal [18], piezoelectric

materials [19-21] and hydrogel [22-24], are also broadly exploited for multifunctional conformable electronics, giving rise to applications in curvilinear electro-optics [25], conformal displays [26, 27], and energy harvesting [28, 29] as shown in Figure 1.1.

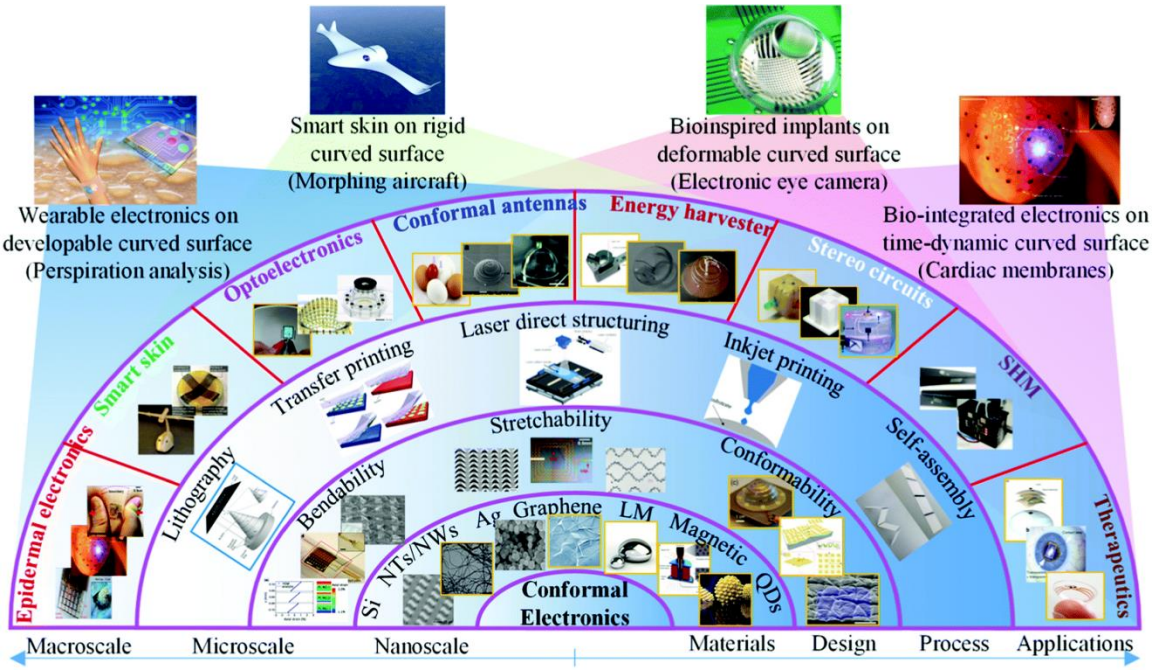

Figure 1.1 Fabrications and applications of 3D conformal electronics on deformable, curved, and time-dynamic surfaces[30].

A crucial reason for the flourish of conformable electronics lies in the rational structural design. The overarching design principle dictates a relatively low structural stiffness, i.e., the strain energy stored in the deformed electronics should be minimized from the energy point of view. If a deformable corrugated surface is encountered, it also requires that the electronics can be easily stretched, compressed, or twisted without detrimental cracks. Towards these two goals, researchers have come up with three strategies by patterning blanket membrane into in-plane meshed structure [31, 32], serpentine ribbons [33, 34], and out-of-plane buckled interconnects [32, 35], as presented in Figure 1.2.

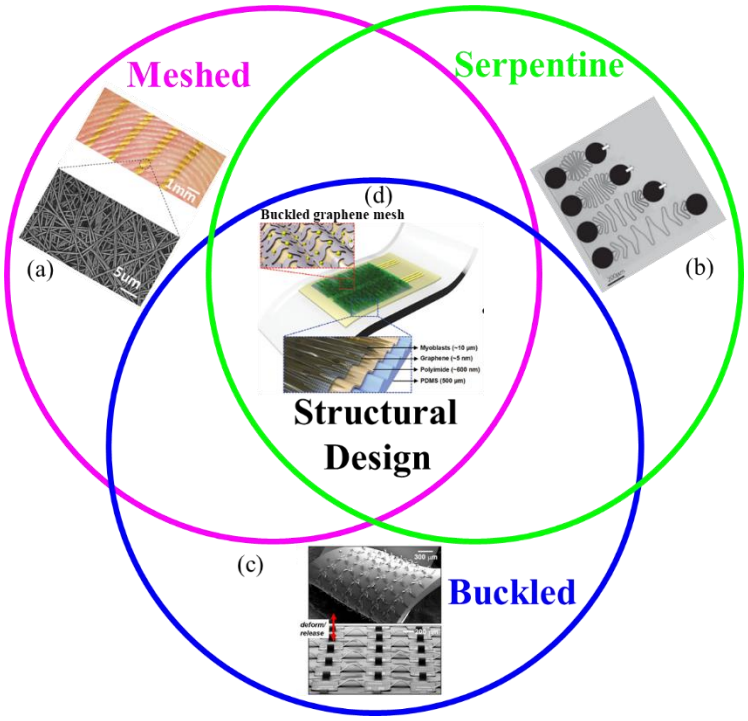

Figure 1.2 Structural design of conformable electronics. (a) Meshed structure [31]; (b) Serpentine structure[33]; (c) Buckled structure[32]; (d) Buckled graphene mesh with serpentine interconnects [5]

The patterned thin membrane reduces the overall structural stiffness, allowing the electronics to follow the morphology of the curvilinear surface with high bendability. The stretchability of serpentine ribbons has been systematically analyzed by Yang *et al* [36] and Zhang *et al* [37, 38] who claimed that the optimized structure can be stretched up to several times of its original length before rupture. In contrast to the tiny rupture strain (~1%) of conventional inorganic semiconductor (e.g., silicon), such remarkable stretchability enables the electronics to firmly attach the rough substrate when subjected to stretching. Actually, these three designs are not mutually exclusive. Instead, hybrid structures have already been widely implemented into smart devices with multifunctionalities [5, 14, 39, 40]. For instance, Figure 1.2(d) is a stretchable medical device with bulked mesh–serpentine graphene electrodes for electrophysiology and therapy of skeletal muscles [5].

1.2 DRY ADHESIVES

In addition to the high bendability and stretchability of the electronics, the interfacial adhesion also plays a significant role in the conformal contact between the electronics and rough surfaces. The interfacial adhesion should be strong enough such that it can provide sufficient driving force for deforming the electronics.

Currently, there is a broad interest in developing imperceptible electronic tattoo (E-tattoo) which are ultra-thin electronics conforming to human skin enabled by pure van der Waals (vdW) adhesion (Figure 1.3 (a)). For example, Ameri *et al* reported a graphene-based electronic tattoo with total thickness ~463 nm [6]. In the same vein, Wang *et al*

fabricated a Au mesh E-tattoo with total thickness ~1 μm [41]. Due to the thin nature, those E-tattoos can firmly stay with the human skin under various body movements while unnoticeably providing high-fidelity sensings, such as electrocardiogram (ECG), skin temperature, and skin hydration. However, vdW adhesion only suffices for sufficiently thin structure. For instance, Ameri *et al* also observed many delaminations in experiments when the thickness of E-tattoo reaches ~700 nm [6]. Therefore, theoretical design guidelines of such ultra-thin imperceptible electronics, e.g., the critical material stiffness and thickness, are indeed of great significance.

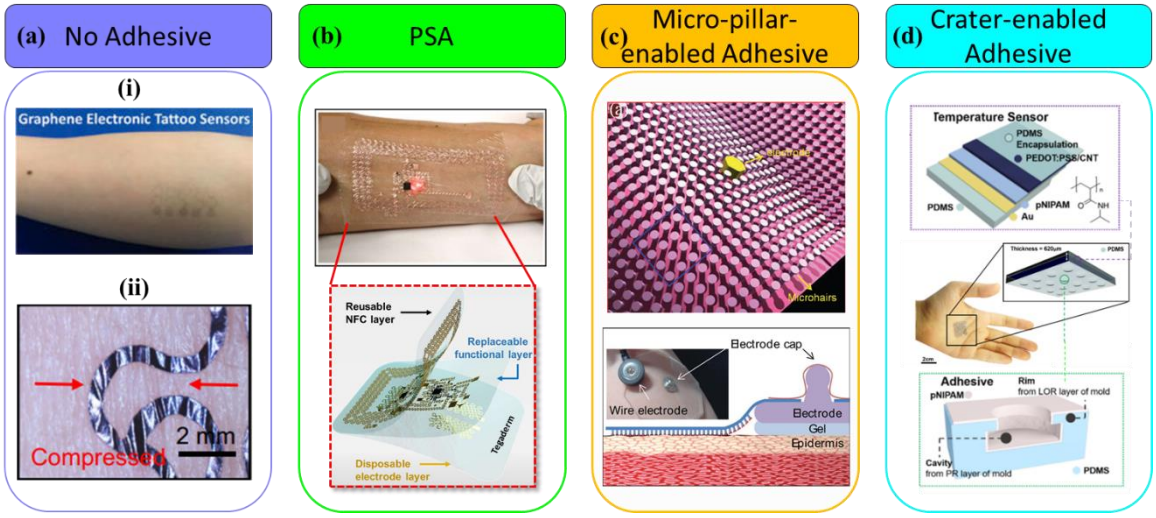

Figure 1.3 Adhesives that used in conformable electronics. (a) No adhesives: (i)[6]; (ii)[41]; (b) Pressure-sensitive adhesives (3M Tegaderm) used for multi-layered electronic patch [42] (c) Micro-pillar-enabled adhesives [43]; (d) Crater-enabled adhesives [44].

When stiff materials are used or multi-layered electronic patches are fabricated (Figure 1.3 (b)), additional adhesive force may be incorporated to secure the conformal contact. An effective candidate for providing strong bonding is so-called pressure-sensitive adhesives (PSA). By employing a viscoelastic bonding agent, PSA can instantaneously form a bond to the rough adherend when pressure is applied [45-48]. As an example, sticky yet highly stretchable, 3M Tegaderm has been extensively used as the supporting substrate for conformable electronics patches [49-52].

Despite the strong bond, PSAs are facing some shortcomings such as degradable tackiness over time, susceptible to impurities, low repositionability, epiderm irritation and skin damage upon peeling [39, 53-55]. To overcome these drawbacks, a wealth of effort has been devoted to exploring alternative chemical-free adhesives, a.k.a *dry adhesives*, in the last two decades, among which gecko-inspired micro-pillars (Figure 1.3 (c)) [43, 56-64] and octopus-inspired craters (Figure 1.3 (d)) [44, 65-71] prevailed. Intrinsically distinct from the chemical-based bonding agent, micro-pillar-enabled and crater-enabled adhesives generate adhesive force via vdW interaction and suction effect, respectively, allowing for superior repeatability to PSAs. By incorporating engineering technologies, dry adhesive can be readily transformed into advanced conformable electronics with integrated functionalities, such as ECG [43, 72] (Figure 1.3 (c)) and temperature [44] (Figure 1.3 (d)) sensing.

To achieve high-strength dry adhesives, extensive studies have been carried out to optimize the structural feather of the micro-pillars [73-81]. Using analytical, numerical, and experimental approaches, different shapes of pillar tip (e.g., round, flat, spatula,

mushroom, and etc.) aspect ratio, material modulus, and other parameters have been systematically investigated. In contrast, even though some have demonstrated crater-enabled dry adhesives exhibit remarkable attachment performance, the suction effect produced by the craters, which may be chiefly responsible for the improved adhesion, has not been properly modeled, not to mention the comprehensive mechanistic understanding of the optimization of a cratered surface.

1.3 OBJECTIVES

There are two objectives for this dissertation. The first is to investigate the contact between the thin membrane electronics and a rough/soft substrate under pure vdW adhesion. After a brief introductory motivation in Chapter 2, we develop an energy minimization framework for quantifying the conformability of a thin membrane laminating onto a deformable substrate with roughness in Chapter 3. Critical parameters such as membrane stiffness, thickness, and interfacial adhesion strength have been revealed for a fully conformed scenario to take place. We also elucidate how the external stretching/compression would alter the conformability in Chapter 4. This study offers a simple analytical guideline for the design and optimization of imperceptibly thin conformable electronics.

The second is to look into the crater-enabled dry adhesives with a particular focus on modeling of the suction effect. In Chapter 5, we offer the motivation for the study of crater-enabled dry adhesives, followed by nonlinear elasticity framework for quantifying the suction force of isolated crater established in Chapter 6. Based on this framework, we

elaborate the effect of surface tension and the aquatic environment on the suction forces of isolated craters in Chapter 7 and Chapter 8, respectively. We also extend the study from isolated craters to crater arrays in Chapter 9 where crater area fraction is considered.

Chapter 2 Motivations for Conformability Study of a Thin Membrane[1]

Conformability describes the degree to which a thin membrane accommodates a corrugated surface. High conformability refers to intimate contact between the thin membrane and the target surface. High conformability can enhance effective membrane-to-substrate adhesion strength and facilitate the signal/heat/mass transfer across the interface, which is of great importance to soft electronics laminated on rough bio-tissues. This chapter will discuss the motivation for the conformability study.

[1]L. Wang and N. Lu, Conformability of a thin elastic membrane laminated on a soft substrate with slightly wavy surface. *Journal of Applied Mechanics*. 2016 Jan 27; 83(4): 041007. (L. Wang conducted the theoretical analysis and wrote the paper)

2.1 CONFORMABILITY

Conformability can be understood as a measure to how large is the true contact area in respect to the nominal contact area between a thin membrane and the rough substrate. When laminating a thin membrane on a substrate with surface roughness, three scenarios can happen: non-conformed, i.e., the membrane remains flat if gravity is not concerned (Figure 2.1(a)); partially conformed i.e., some part of the membrane forms intimate contact with the substrate surface while the other part of the membrane is suspended (Figure 2.1(b)) and fully conformed, i.e., the membrane completely follows the surface morphology of the substrate without any interfacial gap (Figure 2.1(c)). For example, Figure 2.1 (d) shows the angled and cross-sectional scanning electron microscopy (SEM) images of the contact between a silicone replica with different thicknesses (blue) and the surface of a skin (grey), which apparently indicates that a thinner membrane usually exhibits much more conformal attachment onto the curvilinear surfaces [50].

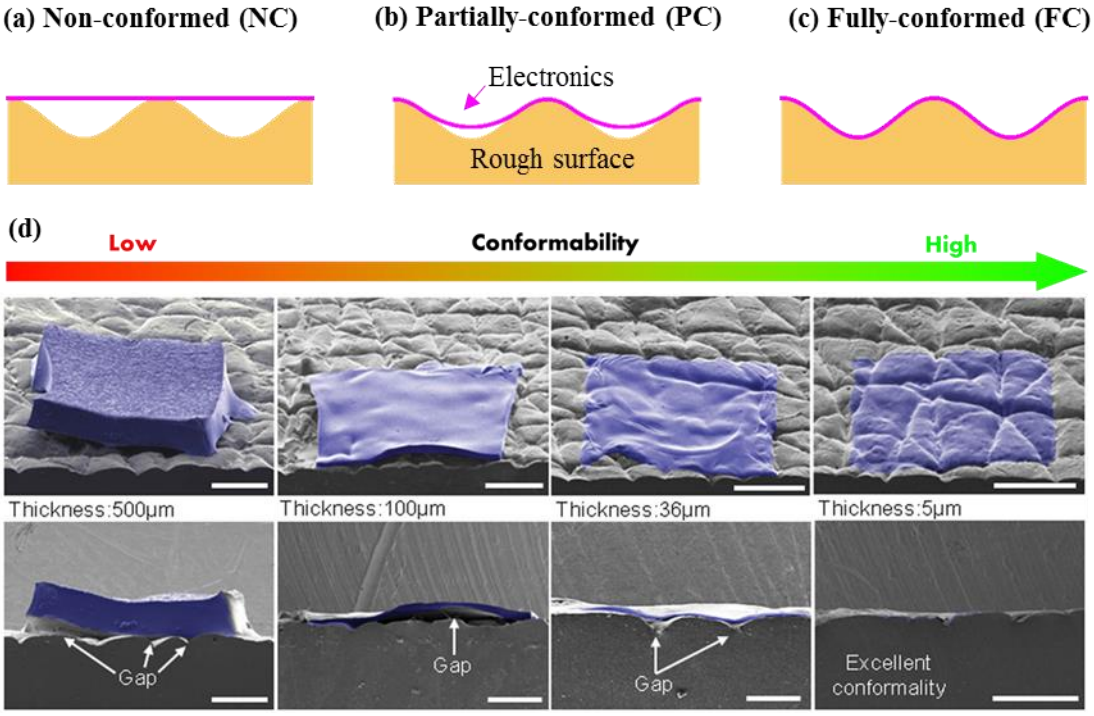

Figure 2.1 (a)-(c) Three possible conformability statuses when a thin membrane is laminated on a corrugated substrate. (d) Angled and cross-sectional SEM images showing the degree of conformal contact between a silicone replica of the surface of the skin and various thicknesses of elastomer membrane substrates [50]

2.2 SIGNIFICANCE OF CONFORMABILITY

Conformability governs the effective adhesion strength between a thin membrane and a rough surface. Higher effective adhesion strength can be achieved by improving membrane-to-substrate conformability, which is chemical-free adhesion is formed due to intermolecular forces known as vdW interactions. These interactions form spontaneously between different molecules, but only if they are close enough to each other i.e., the distance between the molecules has to be in nanometer scale. For example, monolayer graphene to silicon adhesion strength is measured to be higher than few-layer graphene [82], which is attributed to better conformability between monolayer graphene and the silicon substrate [83]. As another example, the feet of geckos and beetles are covered by thin fibers ending with leaf-like plates which can be easily bent to well conform to a rough contacting surface, which considerably enhances the adhesion strength [84, 85]. Moreover, conformability-based metrology has been applied to estimate the adhesion strength between few-layer graphene and a pre-corrugated polydimethylsiloxane (PDMS) [86].

In addition to enhanced adhesion strength, conformability also plays a significant role in the functionality of bio-integrated electronics [87], which have sprung up in recent years due to unlimited potentials in disease monitoring, diagnosis, treatment as well as human-machine interfaces. Contact impedances are minimized between the bio-tissue and the thin film electrode, if the true contact area is as large as possible, giving rise to superior signal-to-noise ratio in both implantable [8, 9, 88] and epidermal [3, 50, 89, 90] electrophysiological (EP) sensors, hydration sensors [91], and temperature detectors [92]. As another example, wearable heaters for thermoregulation and thermal treatment [93, 94]

require uniform and efficient heat transfer at the heater-tissue interface, which fully relies on intimate heater-tissue contact. Moreover, effective device-tissue interface mass exchange for sweat monitoring [95, 96] and on-demand drug delivery [97] would also benefit from conformable device-tissue contact. Therefore, a comprehensive mechanistic understanding of the conformability of thin device sheets on soft bio-tissues can offer important insights into the design of the mechanical properties of the bio-integrated devices.

2.3 THIN MEMBRANE CONFORMING TO A RIGID AND ROUGH SUBSTRATE

The conformability of a thin membrane on a rigid substrate with a corrugated surface has been well studied. For example, in the case of graphene sheets laminated on a silicon substrate, Gao *et al* developed a theoretical model based on van der Waals interaction to reveal how the graphene thickness and the surface roughness of silicon affect the conformability [83]. Wagner *et al* implemented the method of variation of total energy to show that the substrate profile plays a crucial role in determining the transition from partial to full conformability [98]. A snap-through phenomenon has been reported Furthermore, using energy minimization method, Carbone *et al*[99] and Qiao *et al* [100] established a complete theory to predict the FC, PC and NC modes of a thin membrane on a rigid and sinusoidally corrugated substrate. In fact, conformal contact and effective adhesion strength between a thin elastic plate and a rigid and randomly rough (e.g., self-affine fractal) substrate have been studied by Carbone *et al* using contact mechanics [101].

2.4 THIN MEMBRANE CONFORMING TO A SOFT AND ROUGH SUBSTRATE

When the substrate is a soft solid with surface roughness, it can deform due to film-substrate interaction and would also try to conform to the film. Conformability of a thin membrane on rough, deformable substrate still remains veiled so far due to the unclear interaction between the membrane and the soft substrate, especially for partially conformed cases. As a result, the elastic energy stored in the deformed substrate is difficult to obtain unless the corrugated substrate surface deforms from one sinusoidal shape to another sinusoidal shape with the same wavelength but different amplitude, which requires fully conformed contact between membrane and substrate. In this case, analytical solutions of the surface traction and displacement of the substrate are available [102, 103]. Based on those analytical solutions, substrate elastic energy can be computed as the work done to the substrate and hence can be used to predict whether epidermal electronics can fully conform to rough skin surfaces using the energy minimization method [104, 105]. For a general partially conformed scenario, theoretical modeling of conformability is still unavailable.

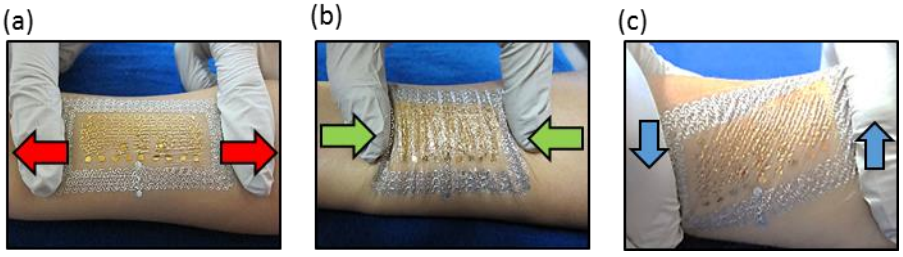

Figure 2.2 Epidermal electronics on human skin demonstrating excellent conformability during (a) stretch (b) compression, and (c) torsion[89].

In addition, equilibrium analysis between membrane and a relaxed substrate is not sufficient for bio-integrated electronics because bio-tissues are dynamic in reality. The degree of conformability can be easily changed by the contraction and expansion of the bio-tissues (Figure 2.2). Therefore, being able to understand and to further control the quality of contact between the thin film device and the dynamic bio-tissue is of practical significance. Actually, the conformability of a thin elastic membrane laminated on a soft corrugated substrate subjected to stretching/compression has been analyzed using the FC theory [105, 106]. But such FC theory failed to draw convincing conclusions for the following reasons. First, it dismisses the possibility of the PC mode and the minimization of the total energy is implemented only within the FC and NC modes. As a result, the energy minimum found by the FC theory may not be the global minimum and the predicted critical conditions for FC may not be enough to reach actual FC. Second, in [105, 106] the substrate energy is miscalculated by adopting a positive sign in front of the applied strain ϵ_0 ($\epsilon_0 > 0$ for tension and $\epsilon_0 < 0$ for compression), which should have been a negative sign according to [103, 107]. Herein, we develop a new theory to account for both partially conformed scenario and external stretching/compression, as will be elaborated in the next chapter.

Chapter 3 Conformability of a Thin Elastic Membrane on Soft and Rough Substrate[2]

The vdW adhesion plays a significant role in enhancing the conformability of the imperceptible membrane-like E-tattoos. In this chapter, we will discuss the conformability of a thin membrane conforming to a soft and rough substrate under pure vdW adhesion. To reveal governing parameters in this problem and to predict conformability, energy minimization is implemented after successfully finding the substrate elastic energy under partially conformable contact. Four dimensionless governing parameters involving the substrate roughness, membrane thickness, membrane and substrate elastic moduli, and membrane-to-substrate intrinsic work of adhesion have been identified to analytically predict the conformability status and the area of contact. The analytical prediction has found excellent agreement with experimental observations.

[2]L. Wang and N. Lu, Conformability of a thin elastic membrane laminated on a soft substrate with slightly wavy surface. *Journal of Applied Mechanics*. 2016 Jan 27; 83(4): 041007. (L. Wang conducted the theoretical analysis and wrote the paper)

3.1 THEORETICAL MODEL

A 2D schematic for the partially conformed configuration is given in Figure 3.1. For simplicity, the membrane is modeled as a uniform linear elastic membrane with plane strain modulus $\bar{E}_m$ and thickness t. The soft substrate is assumed to be a pre-corrugated linear elastic half space with plane strain modulus $\bar{E}_s$. Within the Cartesian coordinate system *xy* as defined in Figure 3.1, the surface profile of the undeformed substrate is simply characterized by a sinusoidal equation

$$w_0(x) = h_0\left(1 + cos\frac{2\pi x}{\lambda}\right) \tag{3.1}$$

where h_0 and λ denote the semi-amplitude and wavelength of the undeformed substrate surface, respectively.

When an elastic membrane is laminated on the soft substrate and starts to conform to the substrate due to interface adhesion, a contact zone with horizontal projection denoted as x_c is labeled in Figure 3.1. Therefore $x_c = \lambda/2$ represents FC scenario, $0 < x_c < \lambda/2$ PC scenario, and $x_c = 0$ NC scenario. Due to the membrane-substrate interaction, the soft substrate deforms. Here, we simply postulate that the surface profile of the substrate within the contact zone deforms from the initial sinusoidal shape to a new sinusoidal shape with the same wavelength but a different amplitude, which can be captured by

$$w_1(x) = h_1\left(1 + cos\frac{2\pi x}{\lambda}\right), \qquad 0 \le x \le x_c \tag{3.2}$$

where h_1 denotes the deformed semi-amplitude while the wavelength λ remains the same as the initial profile. This assumption holds all the way till $x_c = \lambda/2$, which means

in the FC mode, the overall substrate surface deforms from one sinusoidal profile to another with the same wavelength but different amplitude.

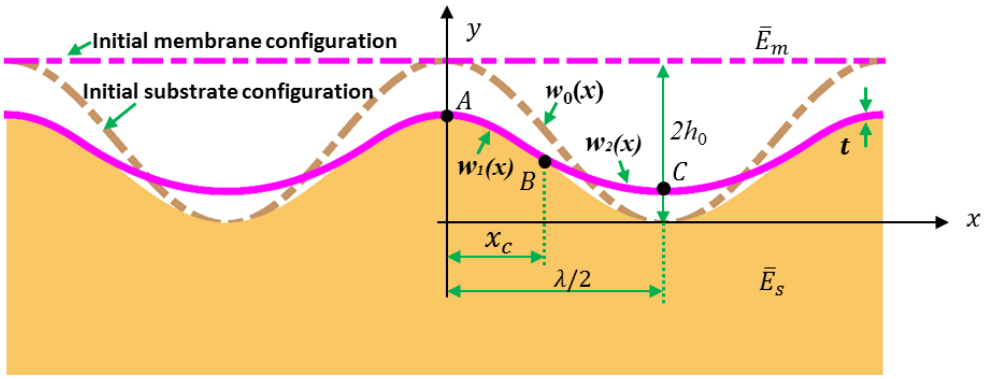

Figure 3.1 Schematic of partially conformed scenario with geometric parameters and characteristic points labeled: the initial amplitude and wavelength of the substrate is $2h_0$ and λ, respectively; after membrane lamination, the substrate surface within the contact zone deforms to a new sinusoidal shape with amplitude $2h_1$ (not labeled in the figure) and unchanged wavelength; x_c is the horizontal projection of the contact zone; Point B denotes the delaminating point.

The profile of a partially conformed membrane, $w_2(x)$ as depicted in Figure 3.1, is sectional: from A to B, i.e., when $0 \le x \le x_c$, the membrane fully conforms to the substrate and thus $w_2(x) = w_1(x)$; from B to C, i.e., when $x_c \le x \le \lambda/2$, the membrane is suspended and $w_2(x)$ is taking a modified hyperbolic shape which will decay to a parabolic shape when normal strain in the membrane is small, i.e., a pure bending condition is assumed [98, 100]. Therefore, $w_2(x)$ can be expressed as

$$w_2(x) = \begin{cases} h_1\left(1 + cos\frac{2\pi x}{\lambda}\right), & 0 \le x \le x_c \\ m\left(x - \frac{\lambda}{2}\right)^2 + n\ , & x_c \le x \le \lambda/2 \end{cases} \tag{3.3}$$

where *m* and *n* are two coefficients to be determined by the continuity condition. Applying the continuity condition at Point B where both the profile and the slope of the membrane should be continuous, i.e., $w_2(x_c) = w_1(x_c)$ and $w_2{}'(x_c) = w_1{}'(x_c)$, we can solve the coefficients *a* and *b* to obtain the profile of the membrane from B to C as

$$w_2(x) = h_1\left[\frac{\pi}{\lambda(\frac{\lambda}{2} - x_c)} sin\left(\frac{2\pi x_c}{\lambda}\right)\left[\left(x - \frac{\lambda}{2}\right)^2 - \left(x_c - \frac{\lambda}{2}\right)^2\right] + 1 + cos\left(\frac{2\pi x_c}{\lambda}\right)\right],\ x_c \le x \le \lambda/2 \tag{3.4}$$

To solve for x_c and h_1 in Eq. (4), energy minimization method is adopted. The total energy of the system U consists of the following four energies:

$$U = U_b + U_m + U_{ad} + U_s \tag{3.5}$$

where U_b is the bending energy of the membrane, U_m is the membrane energy associated with tensile strain in the membrane, U_{ad} is the interface adhesion energy between the membrane and the substrate, and U_s is the elastic energy stored in the substrate, will have to be obtained through contact mechanics analysis. None of the four energies can be neglected in our analysis. Both bending and membrane energies are making significant contributions according to our recent paper of elastic membranes laminated on rigid corrugated substrate [100]. Adhesion energy helps reduce the total energy of the system and is the only negative component out of the four. Nonzero elastic energy stored in the substrate indicates that the substrate is a deformable object.

The bending energy of the membrane (per unit arc length) is given by

$$U_b = \frac{2}{\lambda}\left[\frac{1}{2}\int_A^B \bar{E}_m I\, {\kappa_1}^2 ds + \frac{1}{2}\int_B^C \bar{E}_m I\, {\kappa_2}^2 ds\right] \tag{3.6}$$

where $\bar{E}_m I = \bar{E}_m t^3/12$ is the plane strain bending stiffness of the membrane, κ is its curvature, and ds is the infinitesimal arc length. We use subscript 1 to represent the contact zone, i.e., from A to B, and subscript 2 to denote the non-contacting zone, i.e., from B to C, as labeled in Figure 3.1. The membrane energy per unit arc length can be written as:

$$U_m = \frac{2}{\lambda}\left[\frac{1}{2}\int_A^B \bar{E}_m\, t{\varepsilon_1}^2 ds + \frac{1}{2}\int_B^C \bar{E}_m t\, {\varepsilon_2}^2 ds\right] \tag{3.7}$$

where $\varepsilon_1(x) = \sqrt{1 + {w_1}'^2} - 1$ and $\varepsilon_2(x) = \sqrt{1 + {w_2}'^2} - 1$ are the tensile strains in the adhered and non-contacting zones of the membrane, respectively. Adhesion between the

membrane and the substrate actually reduces system energy so it should be negative. Given the membrane-substrate interface work of adhesion γ, adhesion energy per arc length becomes

$$U_{ad} = -\frac{2}{\lambda}\int_A^B \gamma ds \tag{3.8}$$

For analytical computation of these energies, simplification and nondimensionalization are implemented. Since a slightly wavy surface is considered, the deflection of the membrane is assumed to be small. Therefore, approximations can be applied to simplify the computation of bending energy, which are $\kappa_i \approx w_i''$ (i = 1, 2) and $ds \approx dx$. Hence, the bending energy can be written as:

$$\begin{aligned} U_b &= \frac{2}{\lambda}\left[\frac{1}{2}\int_0^{x_c} \bar{E}_m I\,(w_1'')^2 dx + \frac{1}{2}\int_{x_c}^{\frac{\lambda}{2}} \bar{E}_m I\,(w_2'')^2 dx\right] \\ &= \frac{4\pi^2 h_1^2 \bar{E}_m I}{\lambda^4} D(\hat{x}_c) \end{aligned} \tag{3.9}$$

where

$$D(\hat{x}_c) = \frac{2}{1-\hat{x}_c} sin^2(\pi\hat{x}_c) + \pi^2\hat{x}_c + \frac{\pi}{2} sin(2\pi\hat{x}_c) \tag{3.10}$$

and $\hat{x}_c = 2x_c/\lambda$ is the dimensionless parameter that describes the degree of conformability: $\hat{x}_c = 0$ represents non-conformed, $0 < \hat{x}_c < 1$ means partially conformed, and $\hat{x}_c = 1$ denotes fully conformed. If we define three more dimensionless parameters $\beta = 2\pi h_0/\lambda$, $\eta = t/\lambda$, and $\xi = h_1/h_0$, and substitute $\bar{E}_m I = \bar{E}_m t^3/12$, we can further express bending energy per unit arc length as:

$$U_b = \frac{4\pi^2 h_1^2 \bar{E}_m I}{\lambda^4} D(\hat{x}_c) = \bar{E}_m \lambda \frac{\beta^2 \xi^2}{12}\ \eta^3 D(\hat{x}_c) \tag{3.11}$$

As for the computation of membrane energy and adhesion energy, arc length is taken as $ds \approx \sqrt{1+(w_i{'})^2}dx \approx [1+\frac{1}{2}(w_i{'})^2]dx$ (otherwise, strain $\varepsilon_i(x) = (ds-dx)/dx$ is zero if $ds \approx dx$). Hence membrane energy becomes:

$$\begin{aligned} U_m = \frac{1}{\lambda}\Bigg[& \int_0^{x_c} \bar{E}_m t \left(\frac{1}{2}(w_2{'})^2\right)^2 \left(1+\frac{1}{2}(w_2{'})^2\right) dx \\ & + \int_{x_c}^{\frac{\lambda}{2}} \bar{E}_m t \left(\frac{1}{2}(w_2{'})^2\right)^2 \left(1+\frac{1}{2}(w_2{'})^2\right) dx \Bigg] \\ & = \bar{E}_m \lambda \eta (\beta\xi)^4 K(\hat{x}_c, \xi\beta) \end{aligned} \tag{3.12}$$

where

$$\begin{aligned} K(\hat{x}_c, \xi\beta) = \frac{\beta^2}{107520\pi}\big(& 96\pi(-1+\hat{x}_c)(-28-5\beta^2 \\ & + 5\beta^2\cos(2\pi\hat{x}_c))\, sin(\pi\hat{x}_c)^4 \\ & + 35(144\pi\hat{x}_c + 60\beta^2\pi\hat{x}_c - 3(32+15\beta^2)\sin(2\pi\hat{x}_c) \\ & + 3(4+3\beta^2)\sin(4\pi\hat{x}_c) - \beta^2\sin(6\pi\hat{x}_c))\big) \end{aligned} \tag{3.13}$$

And adhesion energy can be calculated as:

$$U_{ad} \approx -\frac{2\gamma}{\lambda}\int_0^{x_c}\left(1+\frac{1}{2}(w_2')^2\right) \quad dx = -\gamma E(\hat{x}_c,\, \xi\beta) \tag{3.14}$$

where

$$E(\hat{x}_c,\, \xi\beta) = \hat{x}_c\left(1+\frac{(\xi\beta)^2}{4}\right) - \frac{(\xi\beta)^2}{8\pi}\ \ sin(2\pi\hat{x}_c) \tag{3.15}$$

The calculation of the elastic energy stored in the substrate U_s is not as straightforward because the traction between membrane and substrate is not readily known. According to

assumption (ii), displacement of the substrate surface within the contact zone can be calculated as

$$u(x) = w_1(x) - w_0(x) = (h_1 - h_0)\left(1 + cos\frac{2\pi x}{\lambda}\right), \qquad 0 \le x \le x_c \tag{3.16}$$

For the surface traction $P(x)$ over the contact zone as labeled in Figure 3.2, if we just focus on the elastic substrate with a slightly wavy surface, *Johnson* [108] has a conclusion that is directly applicable to our situation. He claimed that $P(x)$ can be comprehended by the superposition of a compressive pressure $P_1(x)$ and a tensile pressure $P_2(x)$, which follows as

$$P(x) = P_1(x) + P_2(x), 0 \le x \le x_c \tag{3.17}$$

Here, $P_1(x)$ is the so called "bearing pressure" which induces a sinusoidal surface displacement $u(x)$ on a soft substrate with either flat or a slightly wavy surface.

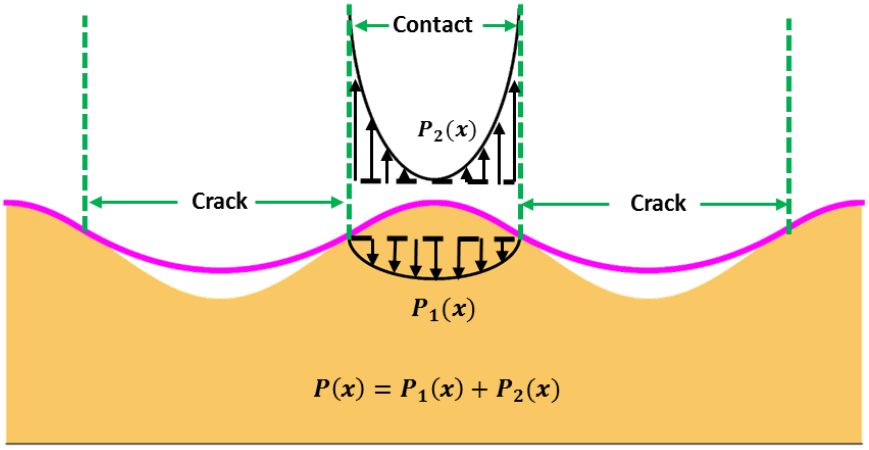

Figure 3.2 Schematic of traction over the contact area in the presence of adhesion by superposition $P(x)=P_1(x)+P_2(x)$.

The contact of two slightly wavy half-planes in the absence of adhesion (Figure 3.3 (a)) was first analyzed by Westergaard [109]. When a rigid body with a slightly wavy surface is compressed against an infinitely large elastic substrate with flat surface as depicted in Figure 3.2(b), contact occurs over width 2a near the crests of the waves. For small amplitude corrugation, following Westergaard's solution [109], the bearing pressure distribution over contact zone, i.e., $0 \le x \le x_c$ in our case, can be expressed as

$$P_1(x) = -2\pi\bar{E}_s \frac{h_0 - h_1}{\lambda} cos\frac{\pi x}{\lambda} \sqrt{\left(sin\frac{\pi x_c}{\lambda}\right)^2 - \left(sin\frac{\pi x}{\lambda}\right)^2}, \qquad (3.18)$$

$$0 \le x \le x_c$$

where the forefront negative sign suggests that $P_1(x)$ is a compressive pressure. The profile of $P_1(x)$ is depicted in (c). When adhesion is taken into account, it will facilitate the two contacting surfaces to be attracted to each other, hence we expect $P_2(x)$ to be a tensile (or positive) pressure. *Johnson* [108] suggested that $P_2(x)$ can be comprehended as the stress distributed across the ligament $(-a < x < a)$ on a plane of collinear, periodic cracks each of length *2b* under remote tensile loading σ_0 (Figure 3.4(a)). In this drawing, the ligament represents the contact zone and the crack represents the non-contact zone as shown in Figure 3.2.

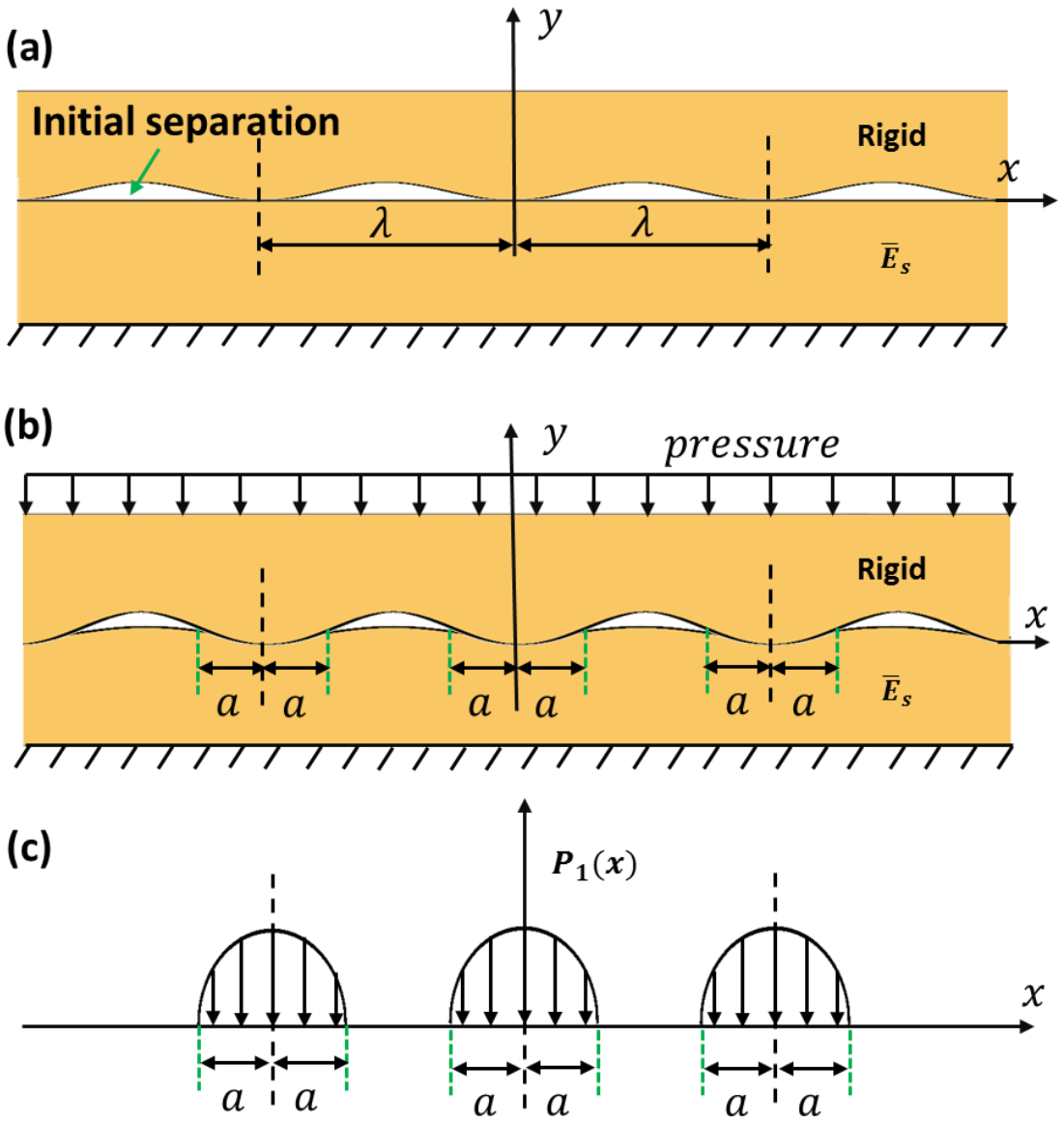

Figure 3.3 (a) Schematic of a rigid, slightly wavy surface with periodicity λ touching a flat elastic surface before any deformation. (b) When subjected to uniform external pressure periodic, sinusoidal displacement is induced in the contact zone ($-x_c<x<x_c$). (c) Distribution of the bearing pressure, $P_1(x)$ within the contact zone.

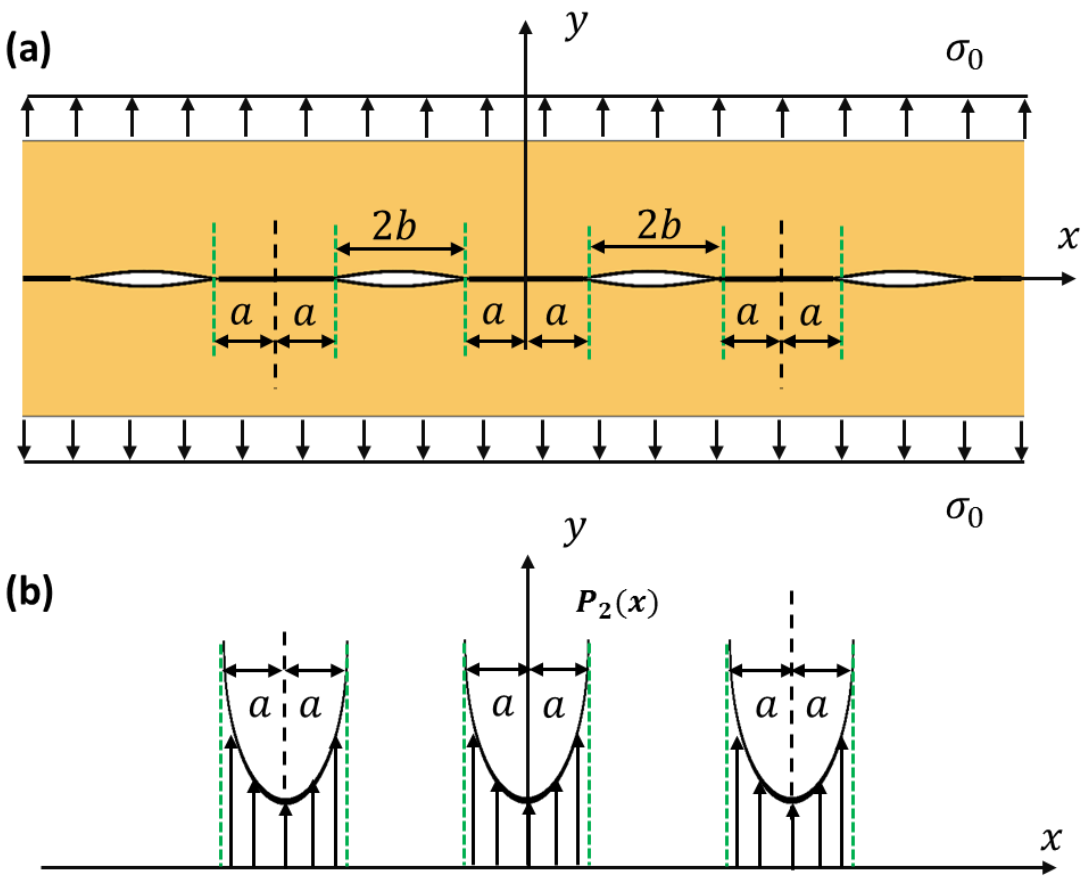

Figure 3.4 (a) A row of collinear cracks in an infinite elastic sheet with crack length 2*a* and interval 2*b*, subjected to remote tensile stress σ_0; (b) Stress distribution over the ligament represents the adhesion stress $P_2(x)$.

The problem of collinear cracks in an infinite elastic sheet was analyzed by *Koiter* [110], who offered the stress distribution over the contact zone, i.e., $0 \le x \le x_c$ in our case, as

$$P_2(x) = \sigma_0 \cos\frac{\pi x}{\lambda}\left[\sqrt{\left(\cos\frac{\pi x}{\lambda}\right)^2 - \left(\cos\frac{\pi x_c}{\lambda}\right)^2}\right]^{-1}, 0 \le x \le x_c \tag{3.19}$$

whose profile is drawn in Figure 3.4 (b). Here σ_0 can be determined by letting the averaged overall traction $\bar{P}$ (Figure 3.3) go zero as the membrane spontaneously conforms to the substrate without any external load [111]:

$$\bar{P} = \int_{-x_c}^{x_c} P(x)dx = \int_{-x_c}^{x_c} [P_1(x) + P_2(x)]dx = 0 \tag{3.20}$$

Solving Eq. (3.20) yields

$$\sigma_0 = \pi \bar{E}_s \frac{h_0 - h_1}{\lambda}\left(\sin\frac{\pi x_c}{\lambda}\right)^2 \tag{3.21}$$

which means that the total traction within contact zone in the presence of adhesion as given by Eq. (3.17) is now fully solved. Hence elastic energy stored in the substrate $U_{substrate}$ per unit arc length can be obtained as the product of traction and displacement:

$$\begin{aligned} U_s &= \frac{2}{\lambda}\int_0^{x_c}\frac{1}{2}u(x)\,P(x)dx = \frac{1}{\lambda}\int_0^{x_c} u(x)\,[P_1(x) + P_2(x)]dx \\ &= \frac{(h_0 - h_1)^2 \bar{E}_s \pi}{4\lambda}\sin^4\left(\frac{\pi \hat{x}_c}{2}\right) \end{aligned} \tag{3.22}$$

Hence the total energy of the system can be explicitly expresses as

$$U = \bar{E}_m\lambda\frac{\beta^2\xi^2}{12}\ \eta^3 D(\hat{x}_c) + \bar{E}_m\lambda\ \eta\ (\beta\xi)^4 K(\hat{x}_c, \xi\beta) - \gamma E(\hat{x}_c,\ \xi\beta) + \frac{\bar{E}_s\lambda\beta^2(1-\xi)^2}{4\pi} sin^4(\frac{\pi\hat{x}_c}{2}) \tag{3.23}$$

Through dimensional analysis, we want to introduce two additional dimensionless parameters $\alpha = \bar{E}_m/\bar{E}_s$ and $\mu = \gamma/(\bar{E}_s\lambda)$, which are membrane-to-substrate modulus ratio and normalized interface intrinsic work of adhesion. Finally, the normalized total energy becomes

$$\widehat{U} = \frac{U}{\bar{E}_s\lambda\beta^2} = \alpha\frac{\xi^2}{12}\ \eta^3 D(\hat{x}_c) + \alpha\ \eta\quad \xi^4\beta^2 K(\hat{x}_c, \xi\beta) - \frac{\mu}{\beta^2}E(\hat{x}_c,\ \xi\beta) + \frac{(1-\xi)^2}{4\pi} sin^4(\frac{\pi\hat{x}_c}{2}) \tag{3.24}$$

which is a function of four dimensionless input parameters: $\beta = 2\pi h_0/\lambda$, $\eta = t/\lambda$, $\alpha = \bar{E}_m/\bar{E}_s$, and $\mu = \gamma/(\bar{E}_s\lambda)$, which are physically interpreted as normalized roughness of the corrugated substrate (β), normalized membrane thickness (η), membrane-to-substrate modulus ratio (α), and normalized membrane-substrate intrinsic work of adhesion (μ), respectively. In addition, there are two unknown dimensionless parameters: $\hat{x}_c = 2x_c/\lambda$ and $\xi = h_1/h_0$, which once solved can yield the contact zone and the amplitude of the deformed substrate. By fixing $\beta, \alpha, \mu,$ and η, minimization of Eq. (3.24) with respect to $\hat{x}_c$ and ξ within the domain confined by $0 \le \hat{x}_c \le 1$ and $0 \le \xi \le 1$ will give us the equilibrium solution, which can be visualized as the global minimum of the 3D plot of the normalized total energy landscape as a function of $\hat{x}_c$ and ξ.

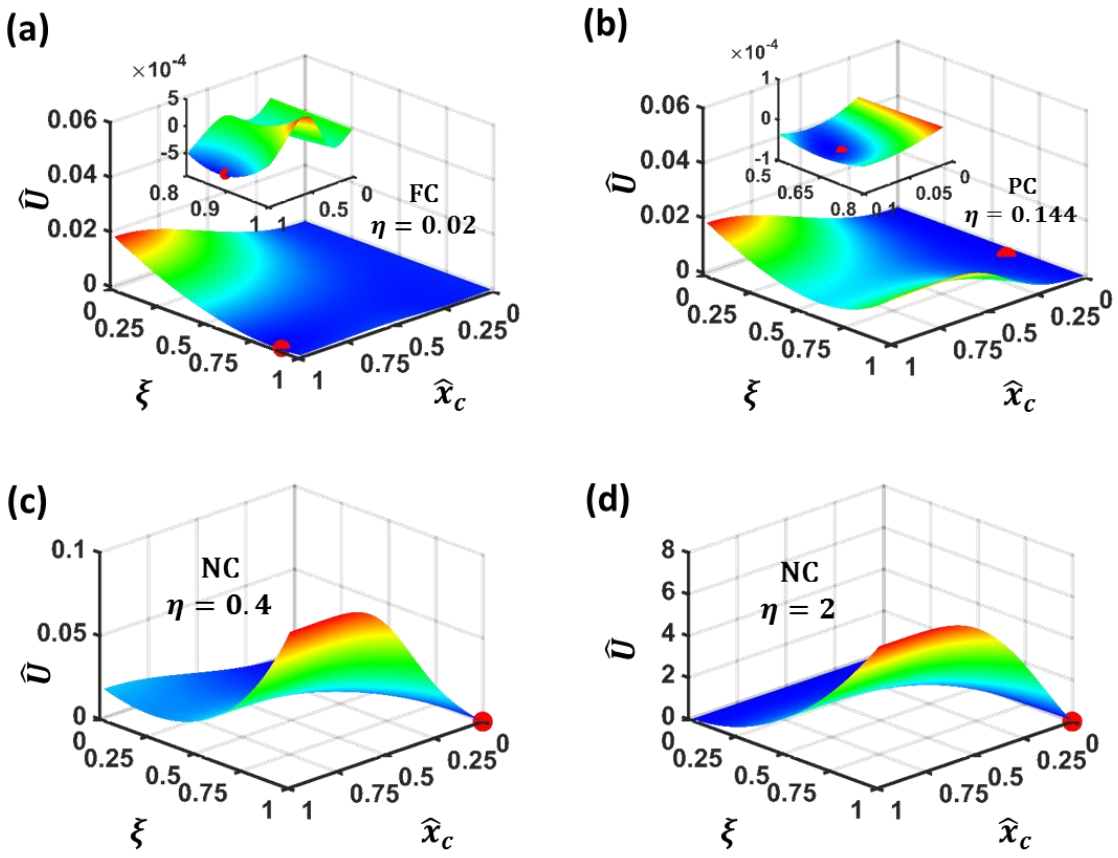

Figure 3.5 (a) Normalized total energy landscape of Ecoflex membrane of four different thicknesses (four different η's) laminating on Ecoflex skin replica where $\alpha = 1, \beta = 1.2, \mu = 0.003$. Global minima are labeled by red dots. (a) When $\eta = 0.02$, $\hat{x}_c = 1$ and $\xi = 0.88$, which indicates FC. (b) When $\eta = 0.0144$, $\hat{x}_c = 0.09, \xi = 0.65$, which predicts PC. (c) When $\eta = 0.4$ and (d) when $\eta = 2$, $\hat{x}_c = 0, \xi = 1$, which suggests NC.

3.2 EXPERIMENTAL VALIDATION

With the total energy obtained in Eq. (3.24), we are now ready to implement the energy minimization method to predict conformability conditions of thin membranes laminated on soft, corrugated substrates. Two experiments in the literature are adopted to validate our model.

3.2.1 Ecoflex Membrane on Skin-like Substrate

Epidermal electronics can be exploited for many clinical and research purposes. Due to the ultimate thinness and softness of epidermal sensors, laminating them on microscopically rough skin surface leads to fully conformal contact, which can maximize the signal-to-noise ratio while minimizing motion artifacts, as evidenced in [112]. To optimize the design of epidermal electronics for human-machine interface, Jeong *et al* [50] tested the conformability of elastomer membranes (Ecoflex, Smooth-On, USA) of various thicknesses on an Ecoflex replica of the surface of human skin. Membrane-substrate conformability is clearly revealed by the cross-sectional scanning electron microscopy (SEM) images : 5 μm thick membrane can achieve full conformability to the substrate, 36 μm thick membrane only partially conformed to the substrate, whereas membranes with thickness of 100 μm and 500 μm remained non-conformed at all (See Figure 2.1 (b)) . Basic parameters that can be extracted from the experiments are: substrate roughness $h_0 = 50\ \mu\text{m}, \lambda = 250\ \mu\text{m}$, plane strain moduli of membrane and substrate $\bar{E}_s = \bar{E}_m = 92$ kPa [50]. Since the conformability experiments were carried by placing Ecoflex membrane on Ecoflex-based skin replica, we assume the interface intrinsic work of adhesion to be

$\gamma = 50\,\mathrm{mJ/m^2}$ according to our recent experimental measurements on the work of adhesion between different types of elastomers [113]. Based on those given parameters, the four dimensionless parameters are computed as follows: $\beta = 1.2, \alpha = 1, \mu = 0.003$, and η =0.02, 0.144, 0.04, and 2, which corresponds to the four different experimental thicknesses of the membrane t = 5 μm, 36 μm, 100 μm, 500 μm, respectively. Normalized total energy given by Eq. (3.24) of each η is calculated and the energy landscape $\widehat{U}$ versus $\hat{x}_c$ and ξ is plotted in Figure 3.5 (a)-(d). When $\eta = 0.02$ (Figure 3.5 (a)), the global minimum falls at $\hat{x}_c = 1$ and $\xi = 0.88$, as highlighted by the red dot in the figure and the inset. $\hat{x}_c = 1$ indicates full confirmability and $\xi = 0.88$ suggests that the substrate is flattened to a new amplitude of $h_1 = 0.88h_0$. When $\eta = 0.144$ (Figure 3.5 (b)), the minimal energy locates at $\hat{x}_c = 0.09, \xi = 0.65$, indicating a partially conformed scenario where contact zone only covers about 9% of the wavelength; As for $\eta = 0.4$ (Figure 3.5 (c)) and $\eta = 2$ (Figure 3.5 (d)) the minimal energy points are both at $\hat{x}_c = 0, \xi = 1$, suggesting that the membrane is non-conformal to the substrate and the substrate is not deformed at all. Therefore, our predictions of conformability for four different membrane thicknesses are in excellent agreement with the experimental findings.

By fixing the substrate morphology $\beta = 1.2$ (i.e., $h_0 = 50$ μm , $\lambda = 250$ μm), Figure 3.6 predicts the conformability as a function of the other three parameters α, μ and η. By numerically solving the minimization problem above, a 3D plot in Figure 3.6 (a) shows two critical surfaces dividing FC/PC and PC/NC. It is obvious that the FC condition can be achieved at small η, i.e., thinner membrane, small , i.e., softer membrane

compared to the substrate, and large μ, i.e., strong membrane-substrate intrinsic work of adhesion. On the contrary, NC condition most likely occurs at large α, large η, and small μ.

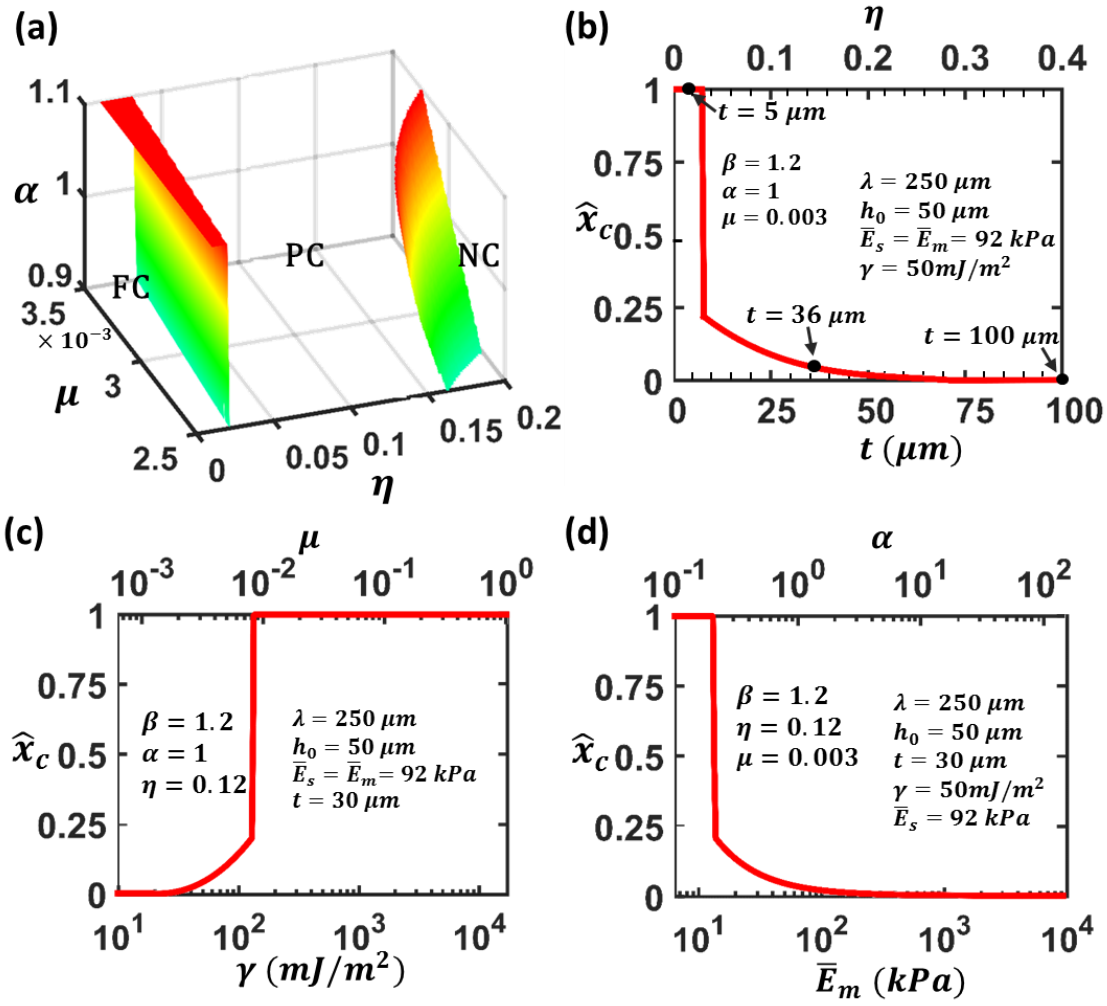

Figure 3.6 (a) Surfaces dividing FC/PC and PC/NC when $\beta = 1.2$ (i.e., $h_0 = 50$ μm , $\lambda = 250$ μm) is fixed. (b) Contact area $\hat{x}_c$ versus η on the top or t in the bottom when $\beta = 1.2, \alpha = 1, \mu = 0.003$. (c) Contact area $\hat{x}_c$ versus μ when $\beta = 1.2, \alpha = 1, \eta = 0.12$. (d) Contact area $\hat{x}_c$ versus α when $\beta = 1.2$, $\mu = 0.003, \eta = 0.12$.

To better illustrate the effect of individual variables, we choose to fix three variables and only change one at a time. For example, in Figure 3.6 (b), $\hat{x}_c$ is plotted as a function of η in the top axis and t in the bottom axis with $\beta = 1.2, \alpha = 1, \mu = 0.003$ fixed. It is evident that as the film thickness grows from 0, the conformability goes from FC to PC and finally NC. While the transition from PC to NC is smooth, the transition from FC to PC is abrupt, which suggests a significant drop (> 77%) of contact area from FC to PC. Similar jump has been observed for few layer graphene (FLG) conforming to silicon substrate [114] and elastic membrane laminated on rigid, corrugated substrate [100]. More analysis on how different substrate morphologies affect snap-through transition can be found in [98]. Quantitatively, full conformability requires $\eta < 0.03$, i.e., $t < 7.5$ μm. When $\eta > 0.28$, i.e., $t > 70$ μm, there is no conformability at all. When $0.03 < \eta < 0.28$, i.e., when 7.5 μm $< t < 70$ μm, the contact area of the PC scenario can be determined. The three black dots indicate the three different membrane thicknesses tested in the experiments by Jeong *et al* [50], which are fully consistent with our prediction.

Since the original epidermal electronics was fabricated on 30 μm thick Ecoflex [3] the conformability of a 30 μm thick membrane on an Ecoflex skin replica substrate has been predicted. In order to show the effect of adhesion energy and membrane modulus over wide range, $\hat{x}_c$ versus μ (or γ) and $\hat{x}_c$ versus α (or $\bar{E}_m$) are plotted with *logx* scale in Figure 3.6 (c) and Figure 3.6 (d), respectively, with the other three variables fixed. In Figure 3.6 (c), it is evident that when $\mu > 0.008$, i.e., $\gamma > 138\ mJ/m^2$, FC mode can be achieved but when $\mu < 0.0016$, i.e., $\gamma < 30\ mJ/m^2$, the membrane would not conform to the substrate at all. Figure 3.6 (d) indicates that when $\alpha < 0.2$, i.e., $\bar{E}_m < 10$ kPa, FC

happens but when $\alpha > 2.5$, i.e., $\bar{E}_m > 125$ kPa, there is no conformability. It is also noted that the abrupt transition from FC to PC is also present in Figure 3.6 (c) and Figure 3.6 (d), with the same maximum contact area (23% of total surface area) under PC. In summary, Figure 3.6 offers a quantitative guideline towards conformable skin-mounted electronics in the four-parameter design space.

3.2.2 Polyimide (PI) Membrane on a Feline Brain *in vivo*

In addition to human skin, brain is another soft organ with surface roughness that can prevent intracranial electrodes from conformal contact with the cortex. To retrieve electrocorticography (ECoG) with high spatial-temporal resolution, Kim *et al* [9] have fabricated ultrathin polyimide supported gold electrode arrays on a bioabsorbable film of silk fibroin. The silk substrate was gradually dissolved after being mounted on the cortex and hence left the ultrathin electrodes wrapping the cortex tissue due to the capillary adhesion. Since the gold layer is only 150 nm thick, which is much thinner than the thinnest polyimide they used (2.5 μm), the gold layer is neglected in the following conformability discussion. The conformability of electrodes with two different polyimide thicknesses (2.5μm and 76 μm) were tested on a feline brain *in vivo*. It turned out that the 2.5 μm thickness electrodes achieved full conformability to the feline brain while the 76 μm thick electrode was not able to conform at all. According to the experimental pictures [9], roughness of the brain gyrus is determined to be $h_0 = 0.24$ mm and $\lambda = 11.86$ mm, which yields $\beta = 0.13$. By neglecting the gold layer, the modulus of the electrodes is given by polyimide modulus: $\bar{E}_m = 2.8$ GPa [9]. The modulus of the brain is found in literature as $\bar{E}_s = 50$ kPa [115]. Hence the membrane-substrate modulus ratio is computed as $\alpha = 56000$. As for the interface intrinsic work of adhesion, since the polyimide substrate is washed by saline solution in the experiment and placed on the wet brain surface, we simply assume the work of adhesion is twice of the surface energy of water at room temperature: $\gamma = 144$ $\mathrm{mJ/m^2}$ which yields $\mu = 0.00024$.

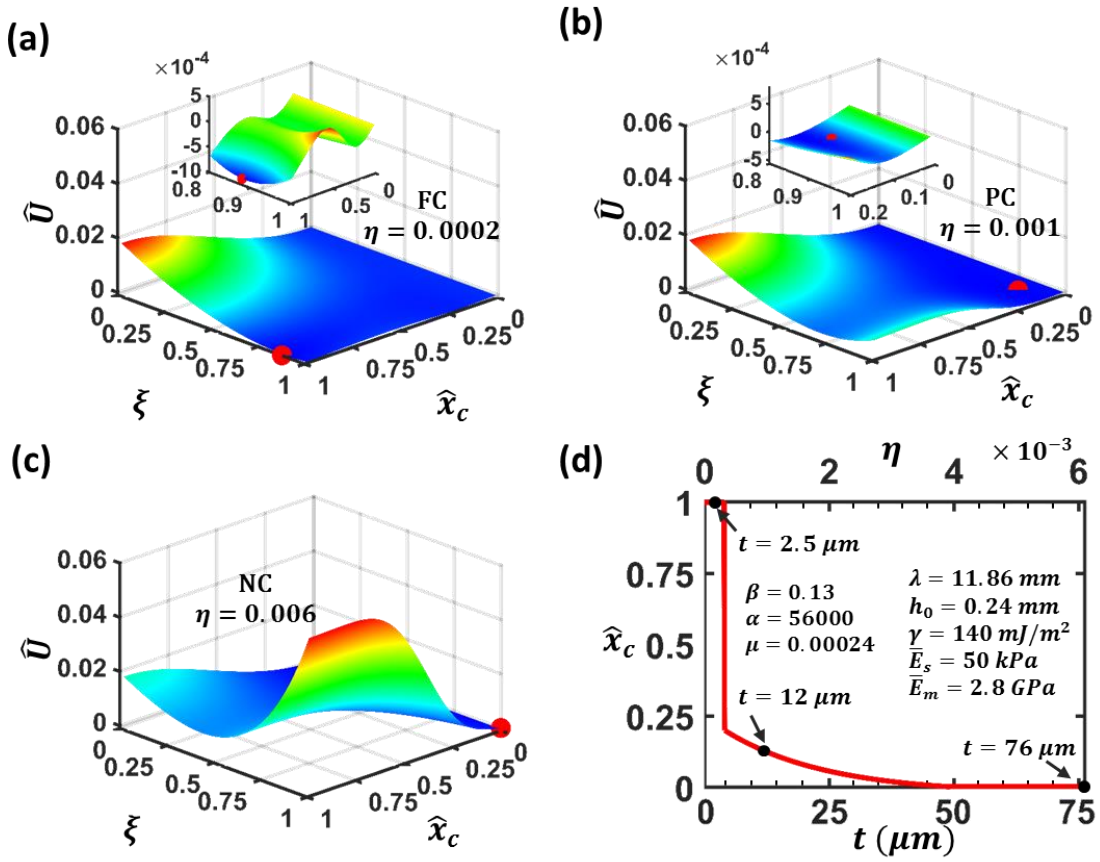

Figure 3.7 (a)-(c) Normalized total energy landscape of polyimide supported electrodes of three different thicknesses (i.e., three different η's) laminated on feline cortex when $\beta = 0.12, \alpha = 56000, \mu = 2.4 \times 10^{-4}$. (a) When $\eta = 0.0002$, $\hat{x}_c = 1, \xi = 0.9$, which indicates FC. (b) When $\eta = 0.001$, $\hat{x}_c = 0.12, \xi = 0.86$, which predicts PC. (c) When $\eta = 0.006$, $\hat{x}_c = 0, \xi = 1$, which suggests NC. (d) Contact area $\hat{x}_c$ versus η on the top or t in the bottom when $\beta = 0.06, \alpha = 56000, = 2.4 \times 10^{-4}$.

The conformability of electrodes with three different thicknesses (2.5 μm, 12 μm, 76 μm) laminated on cortex can be predicted by our theory by substituting $\beta = 0.13, \alpha = 56000, \mu = 0.00024,$ and $\eta = 0.0002, 0.001,$ and 0.006 into Eq. (3.24). The normalized total energy $\widehat{U}$ versus $\hat{x}_c$ and ξ is plotted in Figure 3.7 (a)-(c). When $\eta = 0.0002$ (i.e., *t* = 2.5 μm) (Figure 3.7 (a)), global minimal energy falls at $\hat{x}_c = 1, \xi = 0.9$ as labeled by the red dot. It means the electrode is predicted to fully conform to the brain while the brain was slightly flattened by reducing the amplitude to $h_1 = 0.9h_0$.

When $\eta = 0.001$ (i.e., *t* = 12 μm) (Figure 3.7 (b)), the global minimal minimum locates at $\hat{x}_c = 0.12,\ \xi = 0.86$, as highlighted by the red dot in the figure, which indicates a partially conformed scenario. When $\eta = 0.006$ (i.e., *t* = 76 μm) (Figure 3.7 (c)) the minimal energy occurs at $\hat{x}_c = 0, \xi = 1$, suggesting that the membrane is not able to conform to the cortex at all. To offer a holistic picture of the effect of electrode thickness on conformability, Figure 3.7 (d) plots $\hat{x}_c$ as a function of η as the top axis and *t* as the bottom axis when $\beta = 0.13, \alpha = 56000,$ and $\mu = 0.00024$ are fixed. We use three black dots to represent the three different thicknesses of electrodes. Again, our prediction of conformability agrees well with the experimental findings. Figure 3.7 (d) also tells that full conformability can only be achieved when $\eta < 0.0042$, i.e., the thickness of polyimide should be smaller than 5 μm. The sharp transition from FC to PC modes again suggests that there is an upper limit in the maximum contact area (23% of the total surface area) under the PC condition and hence FC mode is strongly preferred for effective measurements and treatments.

3.3 DISCUSSIONS

3.3.1 Double-checking Assumption (ii) under fully conformed condition

Assumption (ii) dictates that the substrate surface deforms from one sinusoidal shape to another sinusoidal shape over the contact zone. This is inspired by the fully conformed scenario in which the substrate surface undergoes a sinusoidal deformation over the entire wavelength when the membrane is fully attached on it, in which case the traction exerted on the substrate is also sinusoidal and the substrate energy can be readily calculate [104]. Here we would like to double check whether the surface displacement and traction are both sinusoidal under FC mode and whether our substrate energy can recover the result given in [104]. By setting $x_c = \lambda/2$, the elastic energy in the substrate U_s (per unit arc length) can be calculated through the work done by the traction

$$U_s = \frac{1}{2\lambda}\int_0^{\lambda} P(x)u(x)dx = \frac{1}{4}\ \pi\bar{E}_s\frac{(h_0 - h_1)^2}{\lambda} \tag{3.25}$$

which is exactly the same as that obtained by nonlinear analysis of wrinkles [102] and linear perturbation method [103]. This outcome proves that from the energy point of view, our method is validated as it can successfully decay to the fully conformed solution.

3.3.2 Displacement of Substrate Surface in Non-contacting Zone

Displacement of the substrate surface within the contact zone $(0 \le x \le x_c)$ is assumed to be Eq. (3.16) and corthe responding traction with adhesion taken into account is given by Eqs.(3.17)-(3.20) whereas the non-contacting zone $(x_c \le x \le \lambda/2)$ has traction free surface. Then displacement over the non-contacting zone can be written as $u(x) = u_1(x) + u_2(x)$ where the displacement of $u_1(x)$ induced by $P_1(x)$ is given as [111]

$$u_1(x) = (h_1 - h_0)[1 + \cos\frac{2\pi x}{\lambda} + 2\left(\sin\frac{\pi x_c}{\lambda}\right)^2 G(x)], \qquad x_c \le x \le \lambda/2 \tag{3.26}$$

where

$$G(x) = \zeta\sqrt{\zeta^2 - 1} - \ln[\zeta + \sqrt{\zeta^2 - 1}], \qquad x_c \le x \le \lambda/2 \tag{3.27}$$

with $\zeta(x) = (\sin\pi x/\lambda)/(\sin(\pi x_c)/\lambda)$. Since $u_2(x)$ induced by $P_2(x)$ is given as [111]

$$u_2(x) = 2(h_0 - h_1)\left(\sin\frac{\pi x_c}{\lambda}\right)^2 \ln[\zeta + \sqrt{\zeta^2 - 1}], \qquad x_c \le x \le \lambda/2 \tag{3.28}$$

As a result, the non-contacting substrate surface displacement can be analytically expressed.

3.3.3 Thin Membrane versus Thick Slab

In our 2D plane strain theory, the membrane is modeled as a *Bernoulli-Euler* beam (for 2D case, von Karman plate theory should be applied) which undergoes bending and stretching when laminated onto a corrugated substrate. This assumption is valid as long as the thickness of the membrane is much smaller than the wavelength of the corrugated substrate, i.e., $\eta = t/\lambda \ll 1$. However, when the thickness of the film is comparable or even larger than the wavelength of the substrate, this assumption no longer holds, which is referred as a thick slab. When a thick but soft slab is laminated on a corrugated substrate, the lower surface of the slab will deform to fill the cavity between the substrate while the upper surface of the slab will stay almost flat. As a result, the slab needs to be modeled as an elastic body instead of a beam (or plate). Hence, the total energy given by Eq. (3.25) is no longer reliable when for example η = 2 (i.e., t = 500 μm). The contact problems of a thin elastic plate and an elastic body making contact with a randomly rough hard surface were studied by *Perrsson* [101], in which the elastic energy needed to deform a large thin plate U_{plate} and to deform a semi-infinite elastic solid U_{solid} so that they make full contact with a substrate cavity of diameter λ and height h are given as

$$U_{plate} \sim Et^3\left(\frac{h}{\lambda}\right)^2$$
$$U_{solid} \sim E\lambda^3\left(\frac{h}{\lambda}\right)^2 \tag{3.29}$$

respectively, where E is the Young's modulus of the plate or solid on the top. If $t \ll \lambda$ the elastic energy stored in plate is much smaller than the elastic energy stored in a thick

solid. Therefore, the thin plate is elastically softer than a thick slab and hence easier to conform to the substrate.

3.4 CHAPTER SUMMARY

Using the method of energy minimization, this paper develops an analytical model to determine the conformability of a thin elastic membrane placed on a soft substrate with a slightly wavy surface. Four dimensionless governing parameters have been identified. Although the effect of each parameter is monotonic, abrupt transition from FC to PC has been observed for all parameters. Analytical predictions of the conformability of Ecoflex membrane on Ecoflex-based skin replica and polyimide membrane on an *in vivo* feline brain have found excellent agreement with the experimental observations of conformability. Furthermore, critical membrane thickness, membrane-substrate intrinsic work of adhesion, and membrane to substrate stiffness ratio are identified for full conformability. This model hence provides a viable method to predict the conformability and contact area between thin elastic membrane and soft substrate with slightly wavy surface. It also offers a guideline for the design of the electronic membrane as well as the bio-electronic interface to achieve high conformability.

Chapter 4 A Thin Elastic Membrane Conformed to a Soft and Rough Substrate subjected to Stretching/Compression[3]

When the rough surface is dynamically deforming, for example the skin contracts, the deformation may lead to changes in conformability of thin electronics. In this chapter, we will reveal how stretching/compression would affect the conformability. Taking advantage of the path-independent feature of elastic deformation, we find that the total energy of a partially conformed system subjected to stretching or compression can be analytically expressed and minimized. Our results reveal that stretching enhances conformability while compression degrades it. In addition to predicting the critical parameters to maintain fully conformed under deformation, our PC theory can also be applied to predict the critical compressive strain beyond which fully conformed is lost.

[3]L. Wang, S. Qiao, A. Kabri, H Jeong, N. Lu, A Thin Elastic Membrane Conformed to a Soft and Rough Substrate Subjected to Stretching/Compression. *Journal of Applied Mechanics*. 84(11): 111003.2017 Sep 12; (L. Wang conducted the theoretical analysis and wrote the paper).

4.1 THEORETICAL ANALYSIS

4.1.1 Fully Conformed Theory: Loading Path (a)

For simplicity, the membrane is modeled as a uniform linear elastic membrane with plane strain modulus $\bar{E}_m$ and thickness *t*. The soft substrate is assumed to be a pre-corrugated linear elastic half space with plane strain modulus $\bar{E}_s$. Initially, i.e. at State 0 in Figure 4.1, the surface profile of the undeformed substrate is simply characterized by a sinusoidal equation

$$w_0(x) = h_0\left(1 + cos\frac{2\pi x}{\lambda_0}\right) \tag{4.1}$$

where h_0 and λ_0 denote the semi-amplitude and wavelength of the undeformed substrate surface, respectively. Both the membrane and the substrate are stress free in State 0.

4.1.1.1 State 1 in Loading Path (a)

When the membrane is laminated on the soft substrate, it starts to conform to the substrate driven by the membrane-substrate interfacial adhesion. If FC is achieved, i.e. State 1 in Figure 4.1(a), the profiles of both the substrate and the membrane are the same:

$$w_1(x) = h_1(1 + cos\frac{2\pi x}{\lambda_1}) \tag{4.2}$$

where h_1 and λ_1 are the semi-amplitude and wavelength. Since no lateral deformation is applied in State 1 of Figure 4.1 (a), the wavelength remains unchanged, i.e. $\lambda_1 = \lambda_0$. In addition, since the interfacial shear stress can be neglected when the membrane is reasonably stiff [102], the membrane energy can neglected at State 1, i.e. $U_m \approx 0$.

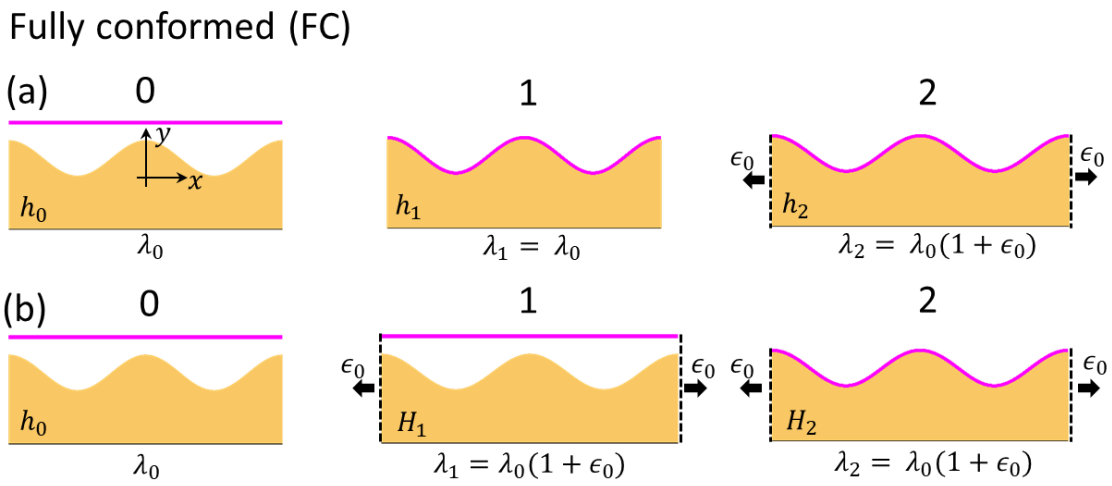

Figure 4.1 Schematics of a thin elastic membrane fully conformed to a soft corrugated substrate following two different loading paths: (a) The laminate-stretching path: the membrane first laminates on the substrate and the system is then subjected to lateral strain ϵ_0. At equilibrium, the substrate surface is characterized by its semi-amplitude and wavelength, i.e. (h_0, λ_0) at State 0; (h_1, λ_1) at State 1; (h_2, λ_2) at State 2. (b) The stretch-laminating path: the membrane and substrate are first subjected to ϵ_0 and then laminated together with ϵ_0 still applied. At equilibrium, the substrate surface is characterized by (h_0, λ_0) at State 0; (H_1, λ_1) at State 1; (H_2, λ_2) at State 2.

Hence, the total energy of the system at State 1 in Figure 4.1(a), U_1^a, consists of the following three energies:

$$U_1^a = U_{b1}^a + U_{ad1}^a + U_{s1}^a \tag{4.3}$$

where superscript "a" represents Loading Path (a), subscript "1" denotes State 1, U_{b1}^a is the bending energy of the membrane, U_{ad1}^a is the interfacial adhesion energy between the membrane and the substrate, and U_{s1}^a is the elastic energy stored in the substrate. Bending energy and adhesion energy per wavelength can be readily written as:

$$\begin{aligned} U_{b1} &= \frac{1}{2\lambda_1}\int_0^{\lambda_1} \bar{E}_m I\, {\kappa_1}^2 dx \approx \frac{1}{2\lambda_1}\int_0^{\lambda_1} \bar{E}_m I\, (w_1'')^2 dx = \frac{4h_1^2\pi^4}{\lambda_1^4}\bar{E}_m I \\ U_{ad1} &= -\frac{1}{\lambda_1}\int_0^{\lambda_1} \gamma ds \approx -\frac{\gamma}{\lambda_1}\int_0^{\lambda_1} [1+\frac{1}{2}(w_1')^2]dx = -\gamma(1+\frac{\pi^2 h_1^2}{\lambda_1^2}) \end{aligned} \tag{4.4}$$

where $\bar{E}_m I = \bar{E}_m t^3/12$ is the plane strain bending stiffness of the membrane, $\kappa_1 \approx w_1''$ is its curvature assuming slight waviness, γ is the membrane-substrate work of adhesion, $ds \approx (1 + 1/2(w_1')^2)dx$ is an infinitesimal segment of the curve.

As for the substrate energy (U_{s1}^a), it should equal to the work done by the surface tractions on the substrate. The surface displacement of the substrate is given by $u(x) = w_1(x) - w_0(x)$ and the surface traction to induce such a surface displacement is found to be $p(x) = -\pi\bar{E}_s/\lambda_1(h_1 - h_0)\cos(2\pi x/\lambda_1)$ [102, 103], which yields the following substrate energy per wavelength:

$$U_{s1}^a = \frac{1}{\lambda_1}\int_0^{\lambda_1}\frac{1}{2}u(x)\,p(x)dx = \bar{E}_s\frac{\pi}{4}\frac{(h_0-h_1)^2}{\lambda_1} \tag{4.5}$$

After introducing five non-dimensional parameters $\alpha = \bar{E}_m/\bar{E}_s$, $\beta = 2\pi h_0/\lambda_0$, $\eta = t/\lambda_0$, $\mu = \gamma/\bar{E}_s\lambda_0$ and $\xi = h_1/h_0$, which are normalized membrane stiffness, substrate roughness, membrane thickness, work of adhesion, and substrate amplitude, respectively, the normalized total energy of the system in State 1 can be rewritten as

$$\widehat{U}_1^a = \frac{U_1^a}{\bar{E}_s\lambda_0\beta^2} = \frac{\pi^2}{12}\xi_1^2\alpha\eta^3 + \frac{1}{16\pi}(1-\xi_1)^2 - \mu\left(\frac{1}{\beta^2} + \frac{1}{4}\xi_1^2\right) \tag{4.6}$$

where $\widehat{U}_1^a$ is a function of five variables α, β, η, μ and ξ_1. If α, β, η and μ are given, minimization of $\widehat{U}_1^a$ with respect to ξ_1, i.e. $\partial\widehat{U}_1^a/\partial\xi_1 = 0$, gives the equilibrium state, which is achieved when

$$\xi_1 = \frac{h_1}{h_0} = \frac{3}{3 + 4\pi^3\alpha\,\eta^3 - 12\pi\mu} \tag{4.7}$$

The FC theory in [104, 105] claims that the criterion for FC is that the total energy of the system at State 1 is lower than that of NC, i.e.

$$\widehat{U}_1|_{\xi_1} < \widehat{U}_1|_{NC} = 0 \tag{4.8}$$

Solving the inequality in Eq. (4.8) yields

$$\alpha\eta^3 < \frac{3(4\mu + \beta^2\mu - 16\pi\mu^2)}{\pi^2(\beta^2 - 16\pi\mu)} \tag{4.9}$$

When β and μ are given, Eq. (4.9) gives a condition that α and η should satisfy for FC.

4.1.1.2 State 2 in Loading Path (a)

Section 4.1.1.1 analyzed the contact between a thin elastic membrane and a relaxed soft substrate with wavy surface, i.e. State 1 in Figure 4.1(a). After that, a lateral strain ϵ_0 is applied on both the substrate and the membrane, as illustrated by State 2 of Figure 4.1 (a). Assuming that the membrane still fully conforms to the substrate after the lateral strain is applied, the substrate will deform to State 2 with the following surface profile:

$$w_2(x) = h_2(1 + cos\frac{2\pi x}{\lambda_2}) \tag{4.10}$$

where the subscript "2" indicates the State 2, h_2 is the new semi-amplitude, and $\lambda_2 = \lambda_0(1 + \epsilon_0)$ is the new wavelength.

Similarly, the bending energy of the membrane and the interfacial adhesion energy per wavelength at State 2 can be found as

$$\begin{aligned} U_{b2}^a &= \frac{4h_2^2\pi^4}{\lambda_2^4}\bar{E}_m I \\ U_{ad2}^a &= -\gamma(1 + \frac{\pi^2 h_2^2}{\lambda_2^2}) \end{aligned} \tag{4.11}$$

while the substrate energy per wavelength becomes [103, 107]

$$U_{s2}^a = \frac{\pi}{4\lambda_2}\bar{E}_s[(h_0 - h_2)^2 + 2h_0(h_2 - h_0)\epsilon_0] + C \tag{4.12}$$

The first term of Eq. (4.12) is the energy associated with the variation of the wavy surface while the second term C is a constant which is independent of h_2 (See Section 4.4.1 for the derivation of C). The membrane energy due to stretching is also a constant, i.e. $U_{m2}^a = \bar{E}_m t\epsilon_0^2/(2\lambda_2) \equiv D$. Since the total energy will be minimized by taking the variation with

respect to h_2, the constant terms C and D can be dropped. Therefore, the normalized total energy at Stage 2 of Figure 4.1(a) is

$$\widehat{U}_2^a = \frac{U_{t2}^a}{\bar{E}_s \lambda_2 \beta'^2} = \frac{\pi^2}{12}\xi_2^2 \alpha \eta'^3 + \frac{1}{16\pi}[(1-\xi_2)^2 + 2(\xi_2 - 1)\epsilon_0] - \mu'\left(\frac{1}{\beta'^2} + \frac{1}{4}\xi_2^2\right) \tag{4.13}$$

where $\beta' = \beta/(1+\epsilon_0)$, $\eta' = \eta/(1+\epsilon_0)$, $\mu' = \mu/(1+\epsilon_0)$ and $\xi_2 = h_2/h_0$. Minimization of $\widehat{U}_2^a$ with respect to ξ_2, i.e. $\partial \widehat{U}_2^a / \partial \xi_2 = 0$, gives the equilibrium substrate semi-amplitude of State 2

$$\xi_2 = \frac{h_2}{h_0} = \frac{3(1-\epsilon_0)}{3 + 4\pi^3 \alpha\, \eta'^3 - 12\pi\mu'} \tag{4.14}$$

Again, solving

$$\widehat{U}_2^a|_{\xi_2} < \widehat{U}_2^a|_{NC} = 0 \tag{4.15}$$

yields a new criterion for FC when lateral tension or compression is applied

$$\alpha \eta'^3 < \frac{3(4\mu' + \beta'^2\mu' - 16\pi\mu'^2)}{\pi^2(\beta'^2 - 16\pi\mu')} \tag{4.16}$$

It is obvious that when $\epsilon_0 = 0$, Eqs. (4.14) and (4.16) will decay to Eq. (4.7) and Eq. (4.9), respectively, which means State 2 will recover State 1 when there is no applied strain. This concludes the analysis of Loading Path (a) using the FC theory (Figure 4.1 (a)). Closed-form solutions have been obtained for both State 1 and State 2. Next, we need to obtain the solution to State 2 of Loading Path (b) (Figure 4.1 (b)) and prove that it is the same as State 2 of Figure 4.1 (a).

4.1.2 Fully Conformed Theory: Loading Path (b)

In Figure 4.1(b), the membrane and substrate are first stretched to State 1, and then the membrane is laminated to the substrate to achieve FC in State 2. We will use this loading path to find the solution to State 2.

4.1.2.1 State 1 in Loading Path (b)

In Figure 4.1(b) State 1, the membrane and the substrate are not in contact and they are individually stretched. Therefore, the top surface of the corrugated substrate is traction free, in which case the wavelength of the substrate surface profile becomes $\lambda_1 = \lambda_0(1 + \epsilon_0)$ and the semi-amplitude will simply change to $H_1 = h_0(1 - \epsilon_0)$ under small ϵ_0 [103]. It is also obvious that both the bending energy of the membrane and the adhesion energy at State 1 are zero, i.e. $U_{b1}^b = U_{ad1}^b = 0$ where superscript "b" stands for Loading Path (b). The membrane energy due to stretching equals $U_{m1}^b = \bar{E}_m t\epsilon_0^2/(2\lambda_1) \equiv D$. Also, the substrate energy and membrane energy are found to be a constant $U_{s1}^b = C$ which is the same as the constant term C in Eq. (4.12).(See Section 4.4.2 for derivation).

4.1.2.2 State 2 in Loading Path (b)

After each being stretched by ϵ_0 (State 1), the membrane is brought into contact with the substrate with ϵ_0 still applied on both. Assuming FC is achieved at equilibrium, as drawn in State 2 of Figure 4.1(b), the semi-amplitude becomes H_2 while the wavelength remains to be $\lambda_2 = \lambda_0(1+\epsilon_0)$. The bending energy of the membrane and the adhesion energy can be written as:

$$U_{b2}^b = \frac{4H_2^2\pi^4}{\lambda_2^4}\bar{E}_m I$$
$$U_{ad2}^b = -\gamma(1+\frac{\pi^2 H_2^2}{\lambda_2^2}) \tag{4.17}$$

Considering the substrate energy at State 1, U_{s1}^b is a constant independent of the amplitude of the wavy surface, the deformation from State 1 to State 2 in Loading Path (b) is analogous to that from State 0 to State 1 in Loading Path (a), i.e., the membrane spontaneously conforms to a traction-free surface. As a result, we can calculate the substrate energy at State 2 by simply modifying Eq. (4.5):

$$U_{s2}^b = \frac{\pi}{4\lambda_2}\bar{E}_s(H_1-H_2)^2 = \frac{\pi}{4\lambda_2}\bar{E}_s[(H_2-h_0)^2 + 2h_0(H_2-h_0)\epsilon_0] + O(\epsilon_0^2) \tag{4.18}$$

Since the stress-strain fields are calculated by linear perturbation method [103], higher order terms are omitted. Therefore, minimization of the total energy $\partial U_2^b/\partial H_2 = 0$ yields:

$$\frac{H_2}{h_0} = \frac{3(1-\epsilon_0)}{3+4\pi^3\alpha\,\eta'^3 - 12\pi\mu'} \tag{4.19}$$

Comparing Eq. (4.19) with Eq.(4.14), we can see that $H_2 = h_2$, which proves that the two loading paths are completely equivalent. This is because stretching in State 1 of Loading Path (b) simply changes the surface profile of the substrate before it contacts the membrane without introducing non-constant energy terms. Therefore, Path (b) shows a potential for developing and solving the PC theory.

4.1.3 Partially Conformed Theory: Loading Path (a)

In Section 4.1.1 and Section 4.1.2, we have proved that the laminate-stretching path and the stretch-laminating path can lead to the same final FC configuration. In this section, we will extend our model to the PC scenario.

4.1.3.1 State 1 in Loading Path (a)

When a membrane is partially conformed to a corrugated substrate, as depicted by State 1 in Figure 4.2 (a), the contact zone is labeled to be $0 \le x \le x_{c1}$ while the detached zone is $x_{c1} \le x \le \lambda_1/2$. This PC state has been investigated in Chapter 3. Here, we postulated that in PC mode, the substrate within the contact zone deforms from its initial sinusoidal profile to a new sinusoidal shape and within the detached zone $(x_{c1} \le x \le \lambda_0/2)$, the membrane simply takes a parabolic shape if the membrane stress is neglected and it is therefore under pure bending. Thus, the associated energies at State 1 can be calculated as

$$U_{b1}^{a} = \frac{4\pi^2 h_1^2 \bar{E}_m I}{\lambda_1^4} D(\hat{x}_{c1}); \;\; U_{ad1}^{a} = -\gamma E(\hat{x}_{c1}, \xi_1, \beta);$$
$$U_{s1}^{a} = \frac{\bar{E}_s \lambda_1 \beta^2 (1-\xi_1)^2}{4\pi} F(\hat{x}_{c1}) \tag{4.20}$$

where $\lambda_1 = \lambda_0, \; \beta = 2\pi h_0/\lambda_0, \; \hat{x}_{c1} = 2x_{c1}/\lambda_0, \; \xi_1 = h_1/h_0$, and

$$D(\hat{x}_{c1}) = \frac{2}{1-\hat{x}_{c1}} sin^2(\pi \hat{x}_{c1}) + \pi^2 \hat{x}_{c1} + \frac{\pi}{2} sin(2\pi \hat{x}_{c1})$$
$$E(\hat{x}_{c1}, \xi_1 \beta) = \hat{x}_{c1}\left(1 + \frac{(\xi_1 \beta)^2}{4}\right) - \frac{(\xi_1 \beta)^2}{8\pi} sin(2\pi \hat{x}_{c1}) \tag{4.21}$$

$$F(\hat{x}_{c1}) = \frac{1}{4} sin^4\left(\frac{\pi \hat{x}_{c1}}{2}\right)$$

When $\hat{x}_{c1} = 1$, Eq. (4.20) decays to Eq. (4.4) and Eq. (4.5) suggesting that our PC theory can successfully recover the FC theory when the there is no detached zone.

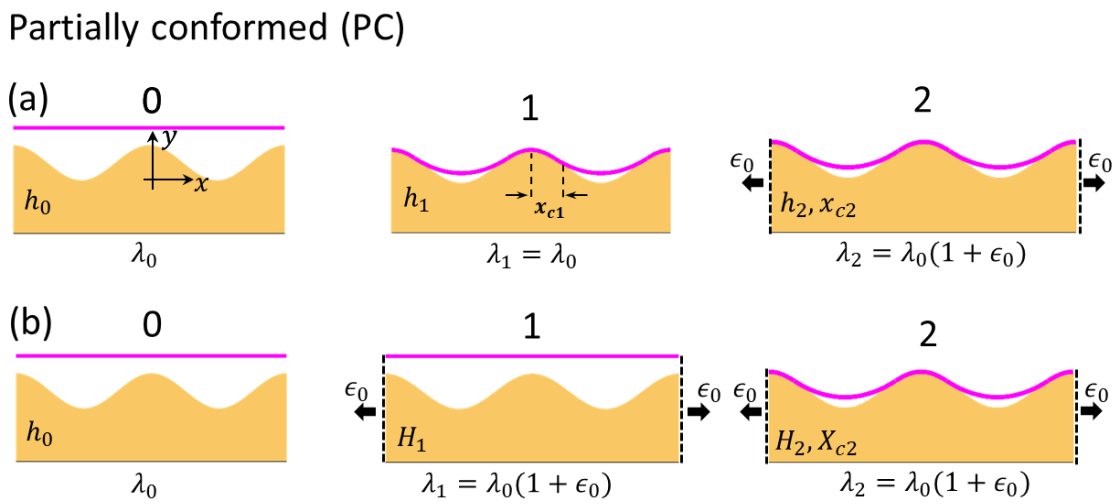

Figure 4.2 Schematics of a thin elastic membrane partially conformed to a soft corrugated substrate following two different loading paths. (a) The laminate-stretching path: at equilibrium, the substrate is characterized by (x_{c1}, h_1, λ_1) at State 1; (x_{c2}, h_2, λ_2) at State 2 where x_c reflects the contact zone size. (b) At equilibrium, the substrate is characterized by (H_1, λ_1) at State 1; (X_{c2}, H_2, λ_2) at State 2.

After introducing the contact zone variable $\hat{x}_{c1}$, the total energy of the system at State 1 becomes a function of six variables $\beta,\ \alpha,\ \eta,\ \mu,\ \xi_1$ and $\hat{x}_{c1}$

$$\widehat{U}_1^a = \frac{U_1^a}{\bar{E}_s \lambda_0 \beta^2} = \frac{\pi^2}{12}\xi_1^2 \alpha \eta^3 D(\hat{x}_{c1}) - \frac{\mu}{\beta^2} E(\hat{x}_{c1},\ \xi_1 \beta) + \frac{(1-\xi_1)^2}{4\pi} F(\hat{x}_{c1}) \quad (4.22)$$

When $\beta,\ \alpha,\ \eta$, and μ are specified, minimization of $\widehat{U}_1^a$ with respect to ξ_1 and $\hat{x}_{c1}$ will yield the equilibrium state. It is worth noting that at equilibrium, $\partial \widehat{U}_1^a / \partial \hat{x}_{c1} = 0$ is not always satisfied due to the fact that $\hat{x}_{c1}$ is limited within $0 \le \hat{x}_{c1} \le 1$. But the condition $\partial \widehat{U}_1^a / \partial \xi_1 = 0$ can always be met, which yields

$$\begin{aligned} \xi_1 = 3(1-\hat{x}_c)\, sin^4\left(\frac{\pi \hat{x}_{c1}}{2}\right) / \{ & 3(\hat{x}_{c1}-1)\, sin^4\left(\frac{\pi \hat{x}_{c1}}{2}\right) \\ & + 2[-4\pi\alpha\eta^3\, sin^2(\pi \hat{x}_{c1}) + (\hat{x}_{c1}-1)(2\pi \hat{x}_{c1}(\pi^2 \alpha \eta^3 - 3\mu) \\ & + (\pi^2 \alpha \eta^3 + 3\mu)\, sin(2\pi \hat{x}_{c1}))]\} \end{aligned} \quad (4.23)$$

Plugging Eq. (4.23) into Eq. (4.22) simplifies the normalized total energy to have only five variables:

$$\widehat{U}_1^a(\alpha, \beta, \eta, \mu, \hat{x}_{c1}) \quad (4.24)$$

For the sake of space, the complete form of Eq. (4.24) is not provided here. For given β, $\alpha,\ \eta$, and μ, normalized total energy $\widehat{U}_1^a$ can be plotted as a function of $\hat{x}_{c1}$ in which minimal energy state can be found. The difference between conformability predicted by the FC theory, i.e. by the minimization of Eq.(4.6), and by the PC theory, i.e. by the minimization of Eq. (4.24), will be discussed in Section 4.2.

4.1.3.2 State 2 in Loading Path (a)

State 1 in Figure 4.2 (a) has been analytically solved by the PC theory. However, after stretching or compression is applied, i.e. at State 2 in Path (a), no analysis regarding the substrate energy is available to the best of our knowledge. Fortunately, we have shown that for the FC case, the two loading paths are interchangeable. Here, we presume that for the PC scenario, the two loading paths can still give identical results according to the following three arguments:

(1) Only small stretching/compression and slightly wavy surface are considered in this paper, i.e. $\epsilon_0 \ll 1,\ h_0/\lambda_0 \ll 1$. These are necessary conditions to derive explicit stress-strain fields by linear perturbation method in [103, 107].

(2) Substrate deformation in PC mode is smaller than that of FC mode.

(3) PC theory can successfully recover the FC theory.

Herein, we assume that State 2 in the PC scenario can be analyzed by following Path (b) in Figure 4.2 in which the substrate is stretched first to have wavelength $\lambda_1 = \lambda_0(1+\epsilon_0)$ and semi-amplitude $H_1 = h_0(1-\epsilon_0)$ at State 1.

Therefore, by modifying Eq. (4.22), the normalized total energy at State 2 can be written as

$$\widehat{U}_2^b = \frac{U_2^b}{\bar{E}_s \lambda_2 \beta'^2} = \frac{\pi^2}{12}\xi_2^2 \alpha \eta'^3 D(\hat{x}_{c2}) - \frac{\mu'}{\beta'^2} E(\hat{x}_{c2},\ \xi_2\beta') + \frac{(1-\epsilon_0-\xi_2)^2}{4\pi} F(\hat{x}_{c2}) \tag{4.25}$$

where $\beta' = \beta/(1+\epsilon_0)$,$\eta' = \eta/(1+\epsilon_0)$,$\mu' = \mu/(1+\epsilon_0)$,$\hat{x}_{c2} = 2x_{c2}/\lambda_2,\ \xi_2 = H_2/h_0$, and

$$D(\hat{x}_{c2}) = \frac{2}{1-\hat{x}_{c2}} sin^2(\pi\hat{x}_{c2}) + \pi^2\hat{x}_{c2} + \frac{\pi}{2} sin(2\pi\hat{x}_{c2})$$

$$E(\hat{x}_{c2},\, \xi_2\beta') = \hat{x}_{c2}\left(1 + \frac{(\xi_2\beta')^2}{4}\right) - \frac{(\xi_2\beta')^2}{8\pi} sin(2\pi\hat{x}_{c2}) \tag{4.26}$$

$$F(\hat{x}_{c2}) = \frac{1}{4} sin^4\left(\frac{\pi\hat{x}_{c2}}{2}\right)$$

Similar analysis can be performed to obtain the equilibrium solution. The criterion to maintain FC when ϵ_0 is applied using the PC theory can be expressed as

$$\alpha\eta'^3 < f(\beta', \mu', \epsilon_0) \tag{4.27}$$

where $f(\beta', \mu', \epsilon_0)$ is numerically obtained. Results will be presented and discussed in Section 4.2.

4.2 RESULTS

The criteria for a thin elastic membrane to fully conform to a soft corrugated substrate subjected to stretching/compression (State 2) have been obtained by the FC theory, i.e. Eq. (4.16), and by the PC theory, i.e. Eq. (4.27), respectively. Note that setting $\epsilon_0 = 0$ in Eq. (4.16) and Eq. (4.27) will lead to the criterion for FC mode at State 1 in the FC and PC theory, respectively. By fixing the moduli of the substrate and membrane, the roughness of the substrate surface, and the interfacial work of adhesion, i.e. by fixing α, β, and μ, we can investigate the effect of membrane thickness, i.e. η, on the conformability. In this section, we will use the following numerical example to illustrate the idea. Considering a silicone membrane of $\bar{E}_m \approx 2$ MPa [106] laminating on human skin whose $h_0 \approx 20$ μm, $\lambda_0 \approx 150$ μm [116], and $\bar{E}_s \approx 130$ kPa [115]. The silicone-skin interface adhesion has been measured to be $\gamma \approx 0.21$ N/m [117]. Accordingly, the non-dimensional parameters can be calculated as $\alpha = \bar{E}_m/\bar{E}_s = 15.4$, $\beta = 2\pi h_0/\lambda_0 = 0.8$, $\mu = \gamma/(\bar{E}_s\lambda_0) = 0.011$.

4.2.1 Laminating on Relaxed Substrate

On the one hand, plugging $\alpha = 15.4, \beta = 0.8, \mu = 0.011, \epsilon_0 = 0$ into Eq. (4.16) yields that the critical thickness of the membrane to fully conform to the skin is 31.5 μm, i.e. $\eta = 0.21$. In other words, according to the FC theory, as long as the membrane is thinner than 31.5 μm, it will fully conform to a relaxed skin. On the other hand, according to the PC theory, the total energy at State 1 of Loading Path (a), $\widehat{U}_1^a$ can be plotted as a function of the contact zone variable $\hat{x}_{c1}$. Normalized energy $\widehat{U}_1^a$ as function of $\hat{x}_{c1}$ with $\eta = 0.11, 0.12, 0.13, 0.14, 0.15$ and 0.21 are plotted in Figure 4.3 (a). The three curves corresponding to $\eta = 0.11, 0.12$ and 0.13 (red, blue and black) all reach the global minimum at $\hat{x}_{c1} = 1$, which indicates that the FC mode is energetically favorable. The difference is that for $\eta = 0.11$ (red), $\widehat{U}_1^a$ monotonically decreases with $\hat{x}_{c1}$, while for $\eta = 0.12$ and 0.13 (blue and black), there is an energy barrier before reaching $\hat{x}_{c1} = 1$. This indicates that PC mode, though excluded by FC theory, could be a locally stable state during the transition from NC to FC. When $\eta = \eta_0 = 0.14$ (magenta), i.e. $t_0 = 21$ μm, there are two global minimums, $\hat{x}_{c1} = 0.36$ and $\hat{x}_{c1} = 1$. Thus, $\eta_0 = 0.14$ is the critical thickness of membrane that assures FC based on the PC theory. For thicker membranes, e.g. $\eta = 0.15$ and 0.21 (green and brown), the global minimum falls at $\hat{x}_{c1} = 0.36$ and $\hat{x}_{c1} = 0.30$, respectively, which indicates that PC is preferred over FC. In summary, we discover that the critical thickness predicted by the PC theory ($t_0 = 21$ μm) is 33% smaller than that predicted by the FC theory (31.5 μm). This is because the FC theory dismisses the possibility of PC so that the minimal energy is searched only within

FC and NC scenarios. In other words, the critical membrane thickness in the FC theory is obtained by equating the total energy at $\hat{x}_{c1} = 0$ and $\hat{x}_{c1} = 1$, which is the case for the brown curve in Figure 4.3 (a). Nevertheless, the PC theory claims that even when $\widehat{U}_1^a|_{FC} < \widehat{U}_1^a|_{NC}$ is satisfied, the FC may not be the most energetically favorable state because there may be a global energy minimum in between, e.g. at $\hat{x}_{c1} = 0.32$ when $\eta = 0.15$ (green).

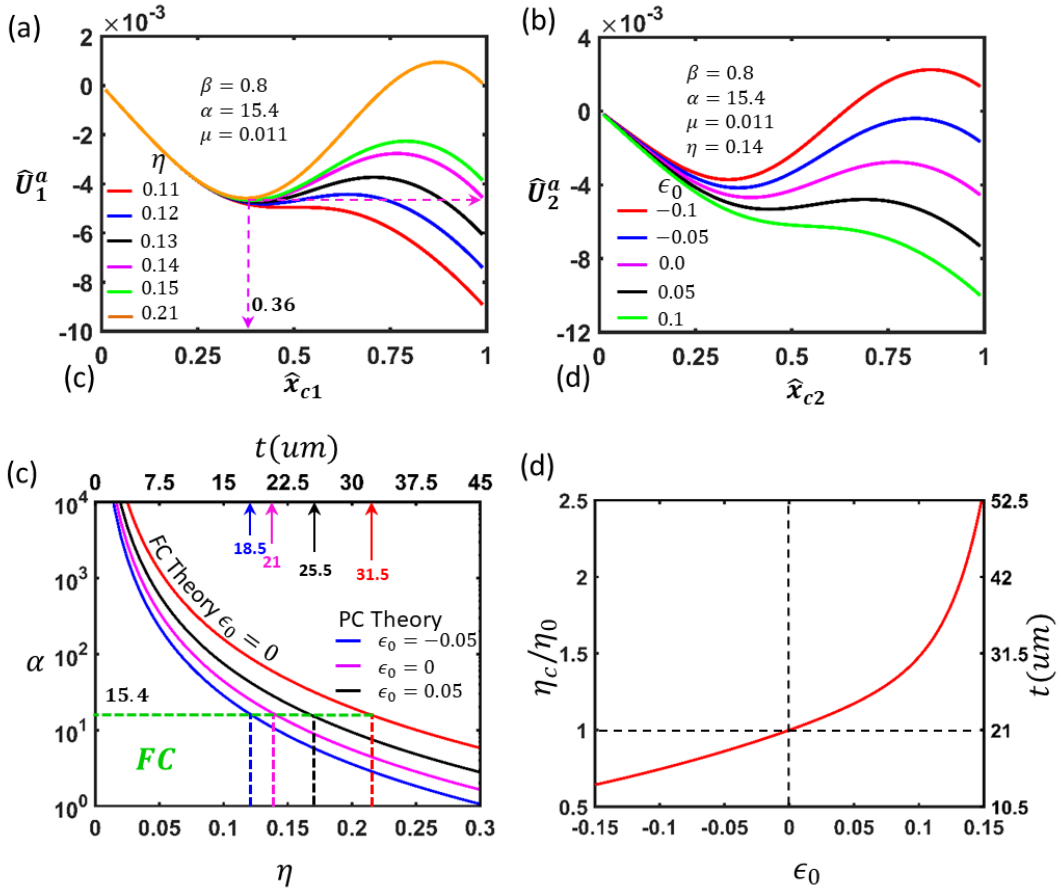

Figure 4.3 (a) Normalized total energy of the system as a function of contact zone variable $\hat{x}_{c1}$ at State 1 with $\beta = 0.8, \alpha = 15.4$ and $\mu = 0.011$ fixed. Six different $\eta = 0.11, 0.12, 0.13, 0.14, 0.15$ and 0.21 are plotted where $\eta = 0.14$ (magenta curve) is the critical membrane thickness for FC. (b) Normalized total energy of the system as a function of contact zone variable $\hat{x}_{c2}$ at State 2 with $\beta = 0.8, \alpha = 15.4$, $\mu = 0.011$ and $\eta = 0.14$ fixed. Five different applied strains $\epsilon_0 = -0.1, -0.05, 0, 0.05$ and 0.1 are plotted. (c) Critical combinations of η and α for FC according to the FC theory (red curve) and the PC theory (blue, magenta, black) with $\beta = 0.8$ and $\mu = 0.011$ fixed. (d) Critical membrane thickness for FC as a function of applied strain ϵ_0.

4.2.2 Strained after Lamination

Due to the limitation of the FC theory, when discussing the conformability after straining, we only focus on the results of the PC theory. First, by fixing $\eta = \eta_0 = 0.14$, i.e. critical thickness $t_0 = 21$ μm of the membrane, we can investigate how the stretching and compression of the substrate affect the conformability. Figure 4.3(b) presents the normalized total energy at State 2 as a function of $\hat{x}_{c2}$ with $\epsilon_0 = -0.1, -0.05, 0, 0.05$ and 0.1. It clearly shows that when stretching is applied, e.g. when $\epsilon_0 = 0.05$ and 0.1 (black and green), the right part of the energy curve bends down, thus FC can be maintained. However, when compression is applied, e.g. when $\epsilon_0 = -0.05$ and -0.1 (blue and red), the right part of the energy curve bends up and global minimum shifts to the middle, hence FC will change to PC under compression. The discovery that conformability can improve when stretching is applied can be easily explained using Loading Path (b). In fact, stretching the substrate in State 1 effectively reduces the surface roughness of the substrate.

One application of this result is illustrated in Figure 4.3(c), which plots the critical (η, α) combination left to or below which FC can be achieved. The red curve in Figure 4.3(c) represents the FC criterion given by the FC theory when $\epsilon_0 = 0$, i.e. Eq. (4.9). When $\alpha = 15.4$, as used in the previous example, the intersection between the dashed green line and the red curve gives the critical thickness of the membrane, which is $\eta = 0.21$ or $t = 31.5$ μm as pointed by the red arrow close to the upper horizontal axis. The magenta curve plots the critical (η, α) combination based on the PC theory when $\epsilon_0 = 0$, i.e. Eq. (4.27).

When $\alpha = 15.4$, the critical thickness is $\eta_0 = 0.14$ or $t = 21$ μm. When a tensile strain, $\epsilon_0 = 0.05$, is applied, the result shifts right to be the black curve, such that the critical thickness enlarges to $t = 25.5$ μm. When a compressive strain, $\epsilon_0 = -0.05$, is applied, the magenta curve shifts left to be the blue curve, such that the critical thickness reduces to $t = 18.5$ μm. Therefore, when a substrate is subjected to arbitrary lateral strain between $-0.05 < \epsilon_0 < 0.05$, it is easy to conclude that the critical thickness for the membrane to always stay FC should be $t = 18.5$ μm.

We may directly visualize the critical thickness η_c as a function of ϵ_0 in Figure 4.3(d). We normalize η_c by $\eta_0 = 0.14$, which is the critical thickness at $\epsilon_0 = 0$ obtained by the PC theory. The actual thickness is denoted by the vertical axis on the right. It is manifest that the critical thickness monotonically increases with increasing ϵ_0, which has an opposite trend to that reported in [105, 106] due to the inversed sign before ϵ_0 in their substrate energy equations as pointed out before. The prediction that stretching allows for thicker membrane to conform can be comprehended by imagining an extreme case in which very large stretching is applied. In this case, the rough surface of the substrate would flatten to an almost smooth surface and then membrane of any thickness would be able to fully conform to it. The other difference is that our plot is based on the PC theory but plots in [105, 106] were based on the FC theory.

4.2.3 Predicting Critical Strain to Losing FC

Another application of our PC theory is to predict the change of conformability with different applied strain. The loading has to be quasi-static as the theory does not involve dynamics analysis. Recently, Ameri *et al* [6, 118] have fabricated an ultrathin and transparent graphene electronic tattoo (GET) sensor that is imperceptible on human skin but can perform multimodal vital sign monitoring. The graphene layer is supported by a transparent PMMA substrate which provides necessary mechanical support for processing and also for transferring GET to human skin. Since graphene thickness is much less compared with the PMMA, the thickness and mechanical properties of the GET are dominated by the PMMA. To fully understand GET conformability on human skin, here we conducted a series of experiments using blanket PMMA membranes with thicknesses of 500 nm, 550 nm and 700 nm and we observed three different conforming behaviors within such a small thickness range. Figure 4.4 displays multiple experimental pictures of those PMMA membranes on human skin with and without skin deformation. It is interesting to note that 500-nm-thick PMMA can fully conform to the skin upon lamination and can stay conformed even under 25% compression (Figure 4.4 (a)). In contrast, Figure 4.4 (b) shows that 550-nm-thick PMMA can fully conform to the relaxed skin but when subjected to 10% compression, internal delaminations can be observed, as indicated by small red arrows. When PMMA is 700-nm thick, Figure 4.4 (c) clearly suggests that it cannot even conform to relaxed skin. With a compression of 10%, more delamination occurred.

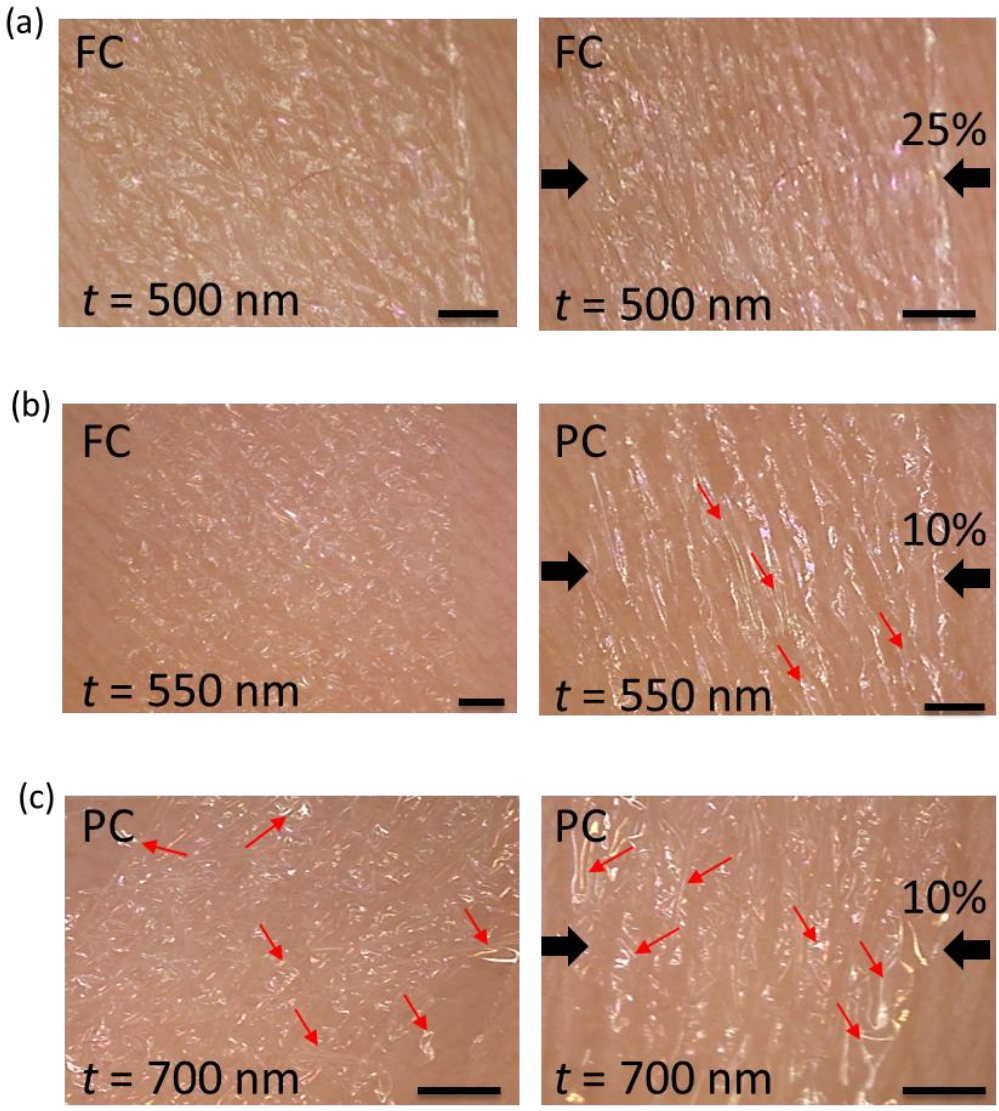

Figure 4.4 Experimental pictures of PMMA membranes on human skin. (a) membrane of thickness t = 500 nm can fully conform to the skin with or without skin compression. (b) membrane of thickness t = 550 nm fully conforms to relaxed skin but experiences partial delamination under a compression of 10%. (c) membrane of thickness t = 700 nm cannot form full conformability even with relaxed skin and more delaminations appear after a compression of 10%. Scale bar indicates 1 mm.

We now can use our PC theory to understand above experimental observations. Parameters are chosen to be $h_0 \approx 20$ μm, $\lambda_0 \approx 150$ μm [116], $\bar{E}_s \approx 130$ kPa [115], $\bar{E}_m \approx 3.3$ GPa [6, 118], $\gamma \approx 18$ mJ/m^2 [119]. Accordingly, the non-dimensional parameters can be calculated as $\beta = 2\pi h_0/\lambda_0 = 0.8$, $\alpha = \bar{E}_m/\bar{E}_s = 25384$, and $\mu = \gamma/(\bar{E}_s\lambda_0) = 0.00092$. Plugging into Eq. (4.24), the system energy after lamination (solid curves) and after compression (dashed curves) for different $t = 500, 550$ and 700 nm are shown in Figure 4.5 (a). It is obvious that the minimal total energy of 500-nm (red solid curve) and 550-nm-thick PMMA (blue solid curve) after skin lamination falls at $\hat{x}_c = 1$ (FC) while that of 700-nm thickness (black curve) falls at $\hat{x}_c = 0.21$ (PC). This is fully consistent with our experimental observations in the left column of Figure 4.4, i.e. 500-nm- and 550-nm-thick PMMA can fully conform to relaxed skin while 700-nm-thick one cannot. When $\epsilon_0 = -0.25$ is applied, the solid red curve shifts to the dashed red curve, whose global minimum still locates at $\hat{x}_c = 1$, which explains why the 500-nm-thick PMMA remained FC under 25% skin compression (Figure 4.4 (a)). In contrast, for 550-nm-thick PMMA, the blue solid curve is bent to the blue dashed curve after $\epsilon_0 = -0.25$, in which case the total minimal energy changes from $\hat{x}_c = 1$ to $\hat{x}_c = 0.17$, i.e. the conformability status switches from FC to PC (Figure 4.4 (b)). The relation between $\hat{x}_c$ and ϵ_0 is plotted in Figure 4.5(b). As expected, the 500-nm-thick PMMA (red curve) can stay FC up to 25% skin compression whereas the conformability of the 550-nm-thick PMMA (blue curve) suddenly drops from FC to PC upon compression at $\epsilon_0 = -0.08$, which explains why we see delamination at 10% compression in our experiment (Figure

4.4 (b)). It is worth noting that this snap-through transition is similar to those reported in previous works [98, 100, 120]. After the sudden change from FC to PC at $\epsilon_0 = -0.08$, our PC theory can continue to predict the change of contact area upon further compression. It is surprising that when the thickness only drops by 50 nm, the 500-nm PMMA (red curve) survives compressive strain of 0.25, which makes it a very good choice for GET because it well balances the tradeoff between conformability and thickness (robustness). However, we have to admit that our current theory is developed within the scope of linear elasticity, hence the predictions for strains beyond 10% will not be very accurate.

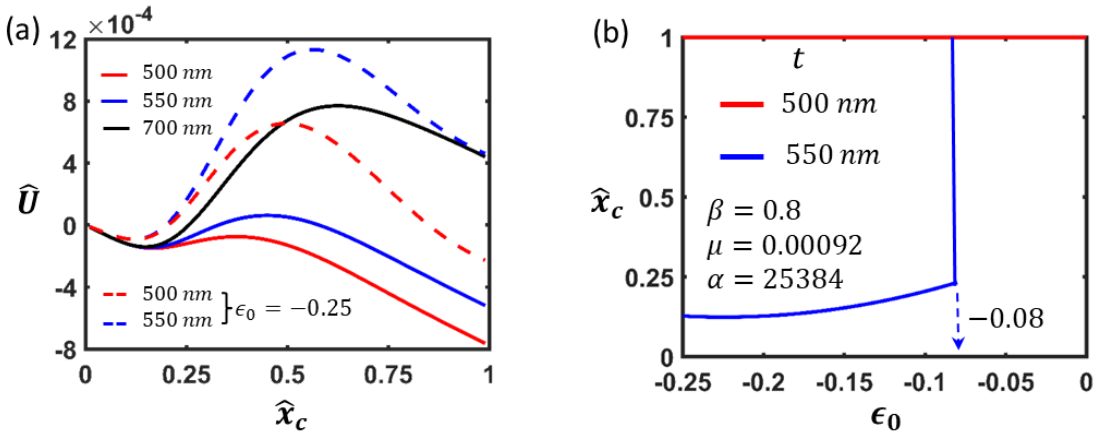

Figure 4.5 Analytical prediction of conformability of PMMA membrane. (a) Normalized total energy of the system as a function of contact zone variable $\hat{x}_c$ with $\beta = 0.8, \alpha = 25384$ and $\mu = 0.00092$ fixed. At State 1, three thicknesses of PMMA $t = 500, 550,$ and 700 nm are plotted as solid curves; At State 2 (e.g. $\epsilon_0 = -0.25$), $t = 500$ and 550 nm are plotted as dashed curves. (b) Conformability as a function of ϵ_0 for PMMAs of thicknesses $t = 500$ nm (red) and 550 nm (blue). Snap-through transition from FC to PC is predicted at $\epsilon_0 = -0.08$ when $t = 550$ nm while PMMA with $t = 500$ nm remains FC throughout the compression up to $\epsilon_0 = -0.25$.

4.3 CHAPTER SUMMARY

In this chapter, by using the method of energy minimization, we developed a theoretical framework to determine the conformability of a thin elastic membrane placed on a soft substrate with slightly wavy surface subjected to stretching/compression. By proving that the laminate-stretching and stretch-laminating loading paths can lead to exactly the same final states for the fully conformed scenario, we demonstrate that the stretch-laminating loading path can also be employed to solve partial conformability under linear elasticity assumptions. Our theory suggests that stretching improves the conformability while compression impairs it, which can be explained by the fact that stretching actually reduces the roughness of the substrate. Furthermore, this framework provides a viable method to predict the conformability and the contact area when the substrate has lateral strain. The critical membrane thickness and membrane-to-substrate stiffness ratio are quantitatively identified for full conformability. Our theory can also be used to predict the strain at which full conformability can no longer sustain. Our theory has been validated by laminating PMMA membranes of different thicknesses on human skin and inducing skin deformation.

4.4 APPENDIX

4.4.1 Substrate energy at State 2 in FC

According to the linear perturbation analysis in Ref. [103], the displacement field at State 2 in Loading Path (a) is given

$$\begin{aligned} u_x &= \epsilon_0 x + \frac{h_0}{2(1-\nu)} e^{k\omega} \sin kx \left[(1-2\nu+k\omega)\frac{h_2-h_0}{h_0}\right. \\ &\quad \left. -(3-2\nu+k\omega)\epsilon_0\right] \\ u_y &= -\frac{\nu}{1-\nu}\epsilon_0\omega + \frac{h_0}{2(1-\nu)}\cos kx \{-2\nu\epsilon_0 \\ &\quad + e^{k\omega}\left[(2-2\nu-k\omega)\frac{h_2-h_0}{h_0} + (2\nu+k\omega)\epsilon_0\right]\} \end{aligned} \tag{4.28}$$

where $k = 2\pi/\lambda$, ν is the Poisson's ratio of the substrate, and $\omega = y - h_0\cos(kx)$ which transforms the substrate with sinusoidal surface to a semi-infinite solid with flat surface $(-\infty < x < \infty, -\infty < \omega < 0)$. The stress and strain fields can be derived accordingly and integrating $\frac{1}{2}\sigma_{ij}\epsilon_{ij}$ over the entire substrate gives the substrate energy at State 2 in Figure 4.1(a)

$$U_{s2}^{a} = \frac{\pi}{4\lambda_2}\bar{E}_s[(h_2-h_0)^2 + 2h_0(h_2-h_0)\epsilon_0] + \frac{\bar{E}_s\epsilon_0^2}{2}H_{sub} \tag{4.29}$$

where H_{sub} is the thickness of the substrate and $H_{sub} \to \infty$ is assumed throughout our analysis. The second term is a constant $C \equiv 1/2\ \bar{E}_s\epsilon_0^2 H_{sub}$. Note that the substrate energy given in Refs. [105, 106] has an inverse sign in front of the ϵ_0 term, which leads to a trend opposite to Figure 4.3(d).

4.4.2 Substrate energy at State 1 in FC

According to the linear perturbation analysis in Ref. [103], the displacement field at State 1 in Loading Path (b) is given by

$$\begin{aligned} u_x &= \epsilon_0 x + (\epsilon_0 h_0)\left(\frac{-2+2\nu-k\omega}{1-\nu} e^{k\omega} \sin kx\right) \\ u_y &= -\frac{\nu}{1-\nu}\epsilon_0\omega + (\epsilon_0 h_0)\left[\left(\frac{-2+2\nu+k\omega}{1-\nu} e^{k\omega} - \frac{\nu}{1-\nu}\right)\cos kx + 1\right] \end{aligned} \tag{4.30}$$

The stress-strain fields can be obtained out of the displacement field and integrating $\frac{1}{2}\sigma_{ij}\epsilon_{ij}$ over the substrate domain gives the substrate energy per wavelength

$$U_{s1}^b = \frac{\bar{E}_s\epsilon_0^2}{2} H_{sub} + \frac{\bar{E}_s\pi h_0^2\epsilon_0^2(5-20\nu+16\nu^2)}{8\lambda_0(1-\nu)(2\nu-1)} \approx \frac{\bar{E}_s\epsilon_0^2}{2} H_{sub} \equiv C \tag{4.31}$$

The first term is simply equal to the work done by the external load on a semi-infinite elastic body with thickness of H_{sub}. The second term is omitted as $H_{sub} \gg h$. Therefore, U_{s1}^b is independent of H_2, thus it does not play a role in the variation of the total energy.

Chapter 5 Background and Motivations for Crater-enabled Dry Adhesive[4]

The vdW interaction between the thin electronics and bio-tissues is a weak bonding, which can only works for ultra-thin electronics with sufficiently low structural stiffness, e.g., E-tattoos. When thick materials are needed or multi-layered electronic patches are fabricated, additional adhesive force may be incorporated to secure the conformal contact. A promising solution is to use dry adhesives. In this chapter, we will elucidate the motivations for the study of crater-enabled dry adhesives due to its remarkable superiority to both chemical-based pressure sensitive adhesives and micro-pillar-based adhesives.

[4] L. Wang, S. Qiao, K. Ha, N. Lu, Understanding Crater-enabled Dry Adhesives. (*To be submitted*). (L. Wang conducted literature review and wrote the paper)

5.1 BACKGROUND AND MOTIVATIONS

In the preceding Chapter 3 and Chapter 4, we built an analytical framework for predicting how an elastic thin film conforms to the soft substrate with wavy surfaces under vdW interaction. We found that the electronics/bio-tissues vdW adhesion is normally weak, e.g., $\gamma \sim 20$ J/m^2, which is not substantially strong for stiff electronics to fully conform to bio-tissues, thus limits the selection of materials and the design of electronics. For example, only when the thickness of the graphene/PMMA membrane drops below 510 nm can it fully conform to the human skin, as predicted by our theory and observed in the experiment [121]. Such a thinness not only makes it difficult for the fabrication process but also renders a low mechanical robustness. The fully conformed contact can also be easily compromised when encountered with compressive deformation since bio-tissues are dynamically deformable.

The current theoretical model elaborated in Chapter 3 and Chapter 4 simplifies the whole electronics patch as an effective elastic thin layer without considering the complex patch configuration. The rigid components, if any, e.g., Bluetooth IC for data transmission, and batters for power supply, etc., will further elevate the overall stiffness of the structure, leading to a poor conformability. Therefore, strong and reliable adhesion between the electronics and bio-tissues is always desired for bridging the intrinsically stiff electronics and soft bio-tissues.

5.2 CONVENTIONAL PRESSURE SENSITIVE ADHESIVES (PSA)

Currently, conventional pressure sensitive adhesives (PSA) are most commonly employed for enhancing the adhesion with bio-tissues. Utilizing a viscoelastic bonding agent, they can instantaneously form a bond to the adherend when pressure is applied without any activation such as treatment with solvents or heat [45-48]. Acrylics, polyether, rubbers, silicones, polyesters, and polyurethanes are commonly used bonding agent for PSA[122, 123]. Due to their viscous nature, PSA can even flow into the surface with multiscale roughness (e.g., skin), leading to a conformal and robust contact.[124, 125] Examples can be found everywhere in healthcare, such as the bandage and 3M Tegaderm for wound covering and healing (Figure 5.1 (a) and Figure 5.1 (b)). In the last two decades, 3M Tegaderm has also been extensively used as the adhesive dressing in epidermal electronics. The strong adhesive force can enable robust contact with skin over a large area with prolonged time and low susceptibility to deformation [89]. (Figure 5.1 (c) and Figure 5.1 (d)).

However, despite the strong adhesion, PSA for bio-medical applications are also facing some challenges and drawbacks. First, the bonding agent can be easily contaminated with impurities (e.g., dust, sebum and cutin etc.) such that PSAs are usually designed for one-time use and are hardly repositionable when in service. Second, the bonding agent may contain chemical irritants that induces skin irritation[126] and contact dermatitis[127]. Third, the excessive adhesive force may be more traumatic to the skin during removal, causing skin injury and damage [39, 53-55] (see Figure 5.2). Therefore, to overcome these limitations, a wealth of attention has been paid to other adhesion mechanisms in the last

two decades, among which bio-inspired dry adhesives stand out as exceptional alternatives to chemical-based PSAs.

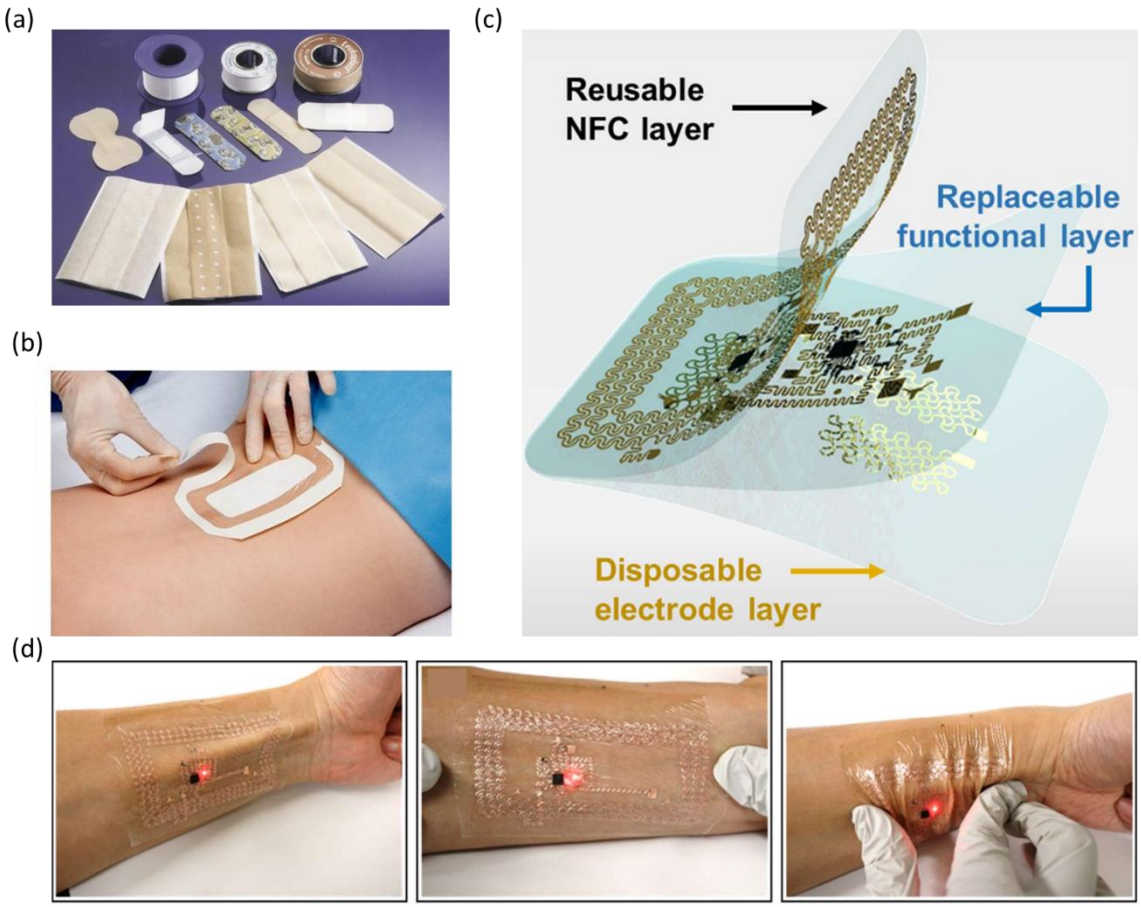

Figure 5.1 Examples of adhesion enhancement using conventional pressure sensitive adhesives. (a) Bandage for wound covering. (b) 3M Tegaderm for wound healing. (c) 3M Tegaderm serves as an adhesive dressing for multi-functional electronics[42]. (d) Epidermal electronics stay fully conformed with the skin under stretching and compression.

Figure 5.2 Types of skin irritation and injury by pressure-sensitive adheisves [39]

5.3 MICRO-PILLAR-ENABLED DRY ADHESIVES

5.3.1 Nature Prototype

The first successful bio-inspiration originates from terrestrial spices with fibril-patterned toe pad including spiders, lizards and geckos [56, 75, 128-131]. The pioneer work done by Autumn *et al* revealed the intricate structures of gecko toe pad by scanning electron microscopy (SEM) [56], where the hierarchical structure is based on the *lamellae*, from which the individual hairs, referred as *setae*, protrude [56]. Each seta branches into hundreds of 200-nm thin *spatula*, which is capable of making intimate contact with a variety of surface profiles of any orientations. As a result, a strong adhesion strength of 100 kPa can be achieved according to the measurement from Autumn *et al*.[56] Such a high adhesion is solely attributed to the vdW forces between the nanoscale spatula and the target surface instead of chemical bonding since no skin gland has been observed on the toe pad of gecko [128].

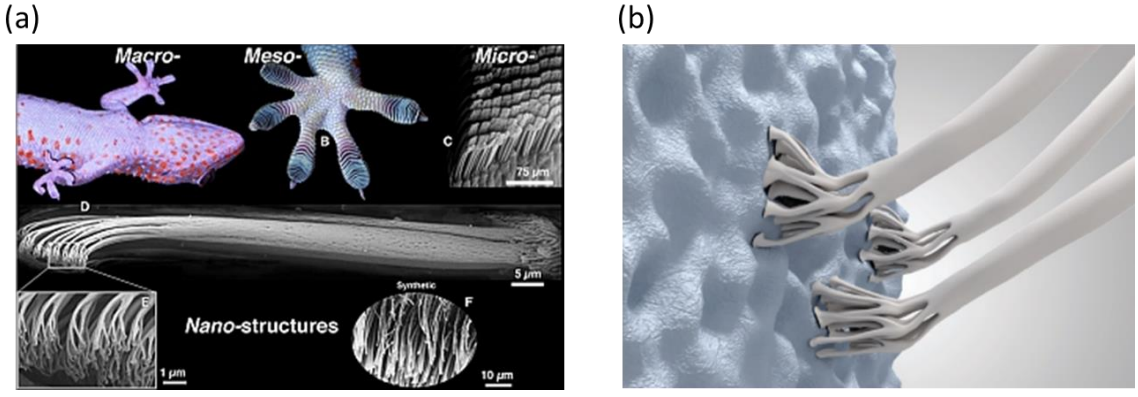

Figure 5.3 (a) Hierarchical structure of gecko's adhesive system.[132] (b) Schematic of gecko adhesion mechanism[133].

Aside from the remarkable attachment performance, the fibrillary system also exhibits superior reversibility and self-cleaning ability: gecko's toe pad can easily peel off from the surface without leaving any residue while keeping the cleanness.[131] due to the "dry" contact.

5.3.2 Artificial Micro-pillar-enabled Dry Adhesives

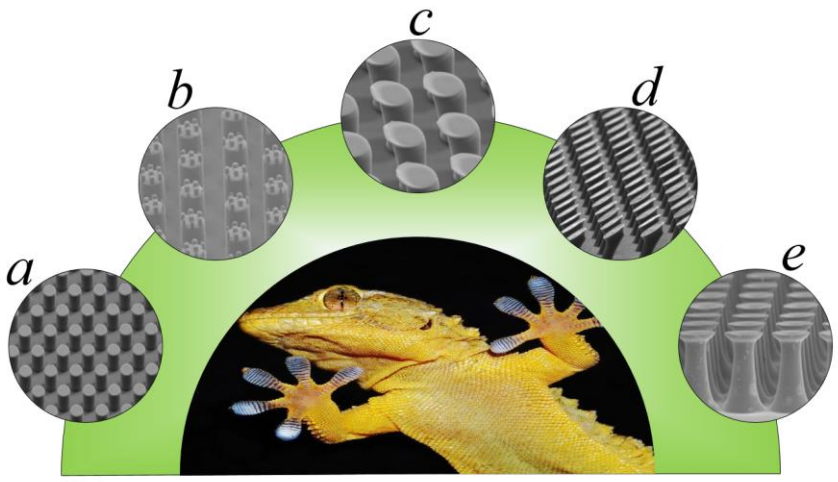

Figure 5.4 Gecko inspired micro-pillar-based adhesives (a) Flat tip [77] . (b) Hierarchical tip [134] ; (c) Spatula tip [135]; (d) Tilted tip [136]; (e) Mushroom-like tip [137].

The rapid advancing of microfabrication techniques, such as photolithography, electron-beam lithography[138, 139] and hot embossing,[140] has contributed to the boom of biomimetic adhesives. Figure 5.4 showcases several representative synthetics mimics with micro-scale surface features in reminiscence of gecko setae. The simplest design of the fibrillary system is micro-pillars arrays with a flat tip (Figure 5.4 (a)) [77, 135, 141]. Since real gecko's toe pad has a hierarchical structure with spatula end, synthetic mimics

with hierarchy [134, 137](Figure 5.4 (b)) and spatula tip [135] (Figure 5.4 (c)) have also been fabricated. Emulating the design principle of the tilting setae in the gecko's toe pad, slanted structures have been widely exploited to generate directional adhesion (Figure 5.4 (d)), i.e., strong adhesion in one direction for gripping and weak adhesion in another for quick releasing[136]. Such an anisotropic adhesion gives rise to the breakthrough in developing reversible adhesives that truly resembles the natural prototypes. Among all the tip geometries, mushroom-like shape (Figure 5.4 (e)) prevails as it shows promising adhesion strength at relatively low preload by reducing the stress concentration when in contact with substrates.[43, 81, 135, 137, 142-144].

By incorporating with engineering technology, e.g., electronic sensors, monitors, etc., the micro-pillar-enabled adhesives can be transformed into advanced biomedical devices other integrated functions such as vital signal monitoring[4, 44] and pressure sensing [12, 145, 146] (see Figure 5.5). In these applications, the dry adhesives serve as a dressing layer which provides strong adhesive force during service, high repeatability, and less skin irritation.

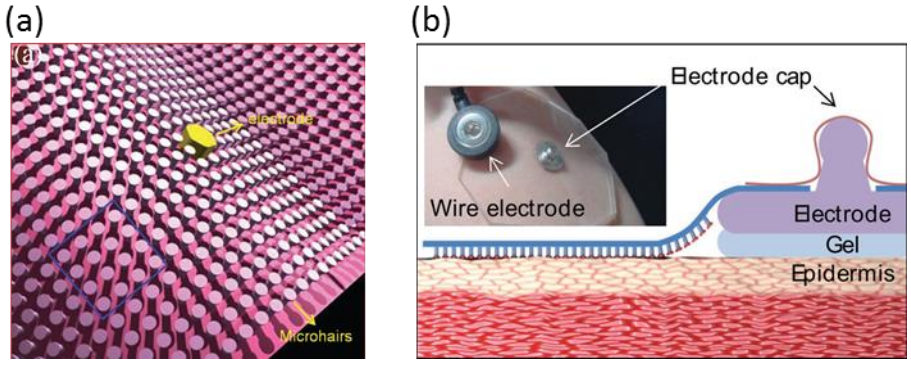

Figure 5.5 Micro-pillar-enabled adhesives with integrated functionalities [43, 72].

5.3.3 Limitations

Though micro-pillar-enabled adhesives have shown promising potential as an alternative to chemical-based PSA, there are still some obstacles that inhibit them from large-scale applications. First, due to the slender nature, tiny pillars possess very low mechanical robustness, leading to lateral collapse (Figure 5.6 (a)) and rupture (Figure 5.6 (b)) after repetitive use. Such a structural instability dramatically impairs the adhesion as well as the repeatability. Second, it has been reported that wet surfaces or underwater environment significantly reduce the performance of micro-pillar-enabled adhesives [147-149], as shown in Figure 5.6 (c). This challenges the application on human skin because of the sweating of the gland.

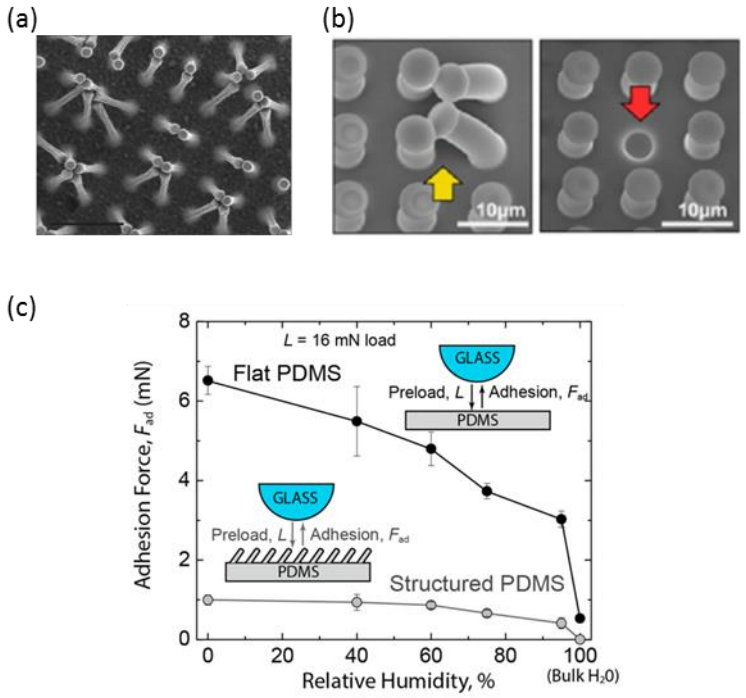

Figure 5.6 Limitation of micro-pillar-enabled adhesives (a) Lateral collapse [57]; (b) Rupture [144]; (c) Low wet adhesion [150].

5.4 CRATER-ENABLED ADHESIVES

5.4.1 Nature Prototype

Another inspiration for the design of dry adhesives comes from aquatic cephalopods such as squid and octopus whose limbs are equipped with hundreds of suckers [65, 151-154]. For example, the octopus can easily anchor onto different terrains and substrates by actively manipulating the muscle on the limbs. Such attachment is secured by the strong suction force due to the pressure difference between the sucker and ambient environment, termed negative pressure, which can roar up to 300 kPa for octopus and 800 kPa for decapod underwater[151, 155]. (Figure 5.7)

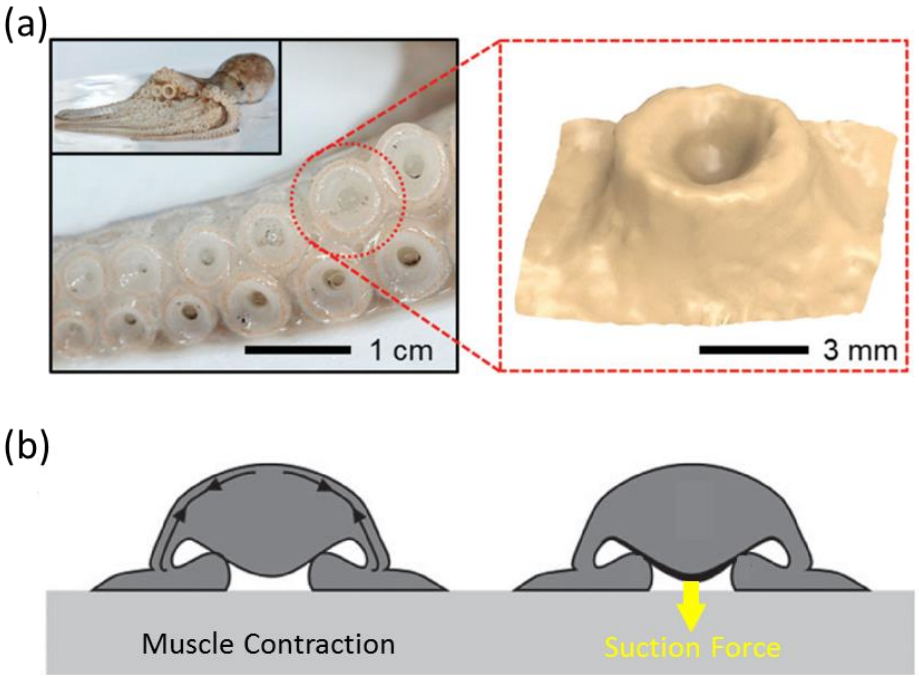

Figure 5.7 (a) Photograph of the cephalopod tentacle (left; inset shows the entire octopus) and 3D laser scanning image of magnified suction cup (right)[67]. (b) Adhesion mechanism of octopus sucker.

5.4.2 Artificial Crater-enabled Dry Adhesives

While commercial use of engineered hierarchical fibrillary structures is at its infancy, low-cost fixtures in the form of suction cups have been widely used in numerous applications, such as wall/window-mounting suction hooks and skin-mounting suction electrodes. Adhesion of suction cups is enabled by vacuum generated inside the cup upon compressive loading and unloading, as inspired by octopus suckers. Similarly, adhesion can also be generated on cratered surfaces which are surfaces with engineered dimples. For example, in 2015, Choi *et al*. created an array of 1-μm-diameter craters on the surface of a multilayer PDMS and the measured adhesion strength exceeds that of the same PDMS with both flat surfaces and surface pillars.[67] (Figure 5.8 (a)). Also in 2015, Akerboom *et al*. fabricated close-packed nano-dimples on 10:1 PDMS and found that the pull-off force is promoted compared with flat PDMS control [66] (Figure 5.8 (b)). In 2017, Baik *et al.* fabricated microscale craters cylindrical-shape and dome-shaped protuberances and their adhesion strength measured under both dry and wet conditions turn out to be much larger than their pillared counterparts.[69] (Figure 5.8 (d)). Similarly, enhanced adhesion has also been observed by Nanni *et al.* who engineered PDMS with square-shaped craters [156]. Octopus suckers equipped with a layer of thermoresponsive hydrogel show switchable adhesion and thus, can be used for transfer printing of semiconducting nanomembranes [68] (Figure 5.8 (e)). Octopus-inspired micro-craters with built-in protuberance structure demonstrated load-dependent adhesion both in dry and wet conditions [157], distinct from that of gecko-like adhesives. PDMS nanosucker arrays are flexible and generate strong adhesion even when applied on irregular surfaces [158].

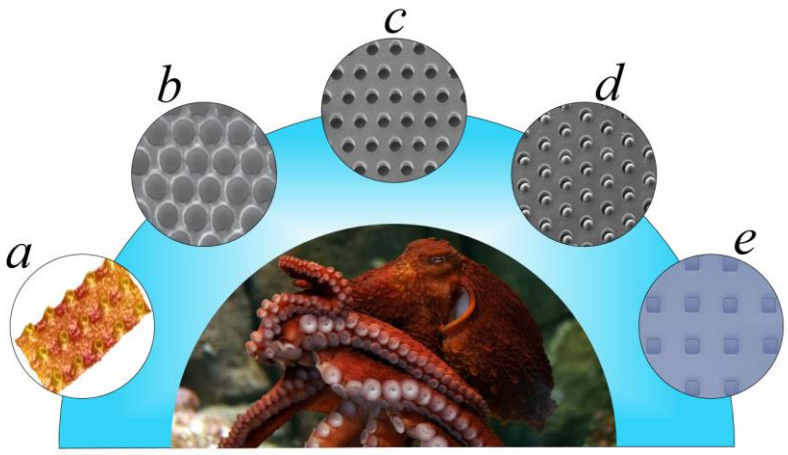

Figure 5.8 Octopus inspired crater-enabled dry adhesives. (a) [67] (b) [66]; (c)-(d) [69]; (e) [156]

Unlike the abundant theoretical understandings for microfibrils [130, 159-161], cratered surfaces are emerging physical adhesives that little analysis is available at this moment. Although thin-walled suction cups have been modeled before [162, 163], surface craters [68, 157, 164-166] are surrounded by thick walls and therefore demand different analysis. Spolenak *et al* investigated various suction effect in pillars with concaved tip [159], but the pressure drop in the suction cup was considered to be constant. In Baik *et al* (2017), the authors presented a closed-form solution for the adhesion strengths of cratered surfaces. However, the analysis is based on the prior work of Afferrante *et al* [167] and Tramacere *et al* [168], which is applicable to suction cups rather than craters. All of these call for a new modeling scheme for crater-enabled dry adhesives.

5.5 CHAPTER SUMMARY

In this chapter, three types of adhesives have been discussed. The conventional pressure sensitive adhesives, which are widely used in healthcare but still facing some limitations; the micro-pillar-enabled adhesives which have emerged as a new dry adhesive but also suffer from the low structural stability and repeatability; and crater-enabled dry adhesives, which are still in its infancy but have exhibited many superiorities to others. Fundamental understanding of the behavior of craters is critical to the design, including optimal selection of material properties, crater shape, and preload. In Chapter 6, we will establish a theoretical framework to analyze isolated craters in ambient condition, obtain nonlinear solutions to preload-dependent suction forces, and validate our solutions by experiments. We regard this study as an essential step toward developing a comprehensive framework for quantitative characterization of cratered surface. Utilizing this framework, we continue to consider the effect of surface tension (Chapter 7) and aquatic environment condition (Chapter 8) on isolated crates and extend to crater arrays in Chapter 9.

Chapter 6 Isolated Craters in Ambient Environment[5]

Enhanced adhesion of crater-enabled dry adhesives is primarily attributed to the suction effect. In this chapter, we develop a framework for quantifying the suction effect produced by isolated craters combining experimental, numerical simulation and analytical approaches. The modeling approach emphasizes the essential role of large elastic deformation, while the airflow dynamics, microscopic mechanisms, like surface tension and air permeation, and rate-dependence are neglected. This approach is validated using experimental data for isolated hemispherical craters. The modeling approach is further applied to spherical cap (not necessarily hemi-spherical) craters with the objective of identifying optimal geometric and material properties, as well as the minimum preload necessary for attaining the maximum suction force.

[5] S. Qiao, L. Wang, G. Rodin, N. Lu*. Suction effects in cratered surfaces. *Journal of the Royal Society Interface*. 14(135):20170377. Oct 1, 2017. (L. Wang conducted some parts of numerical simulations, experiments and wrote the analysis section in the paper)

6.1 HEMI-SPHERICAL CRATERS

In this section, we use experimental, computational, and analytical approaches to study isolated hemi-spherical macroscopic craters. The computational framework established in this section will be applicable to more general classes of isolated macroscopic craters, i.e., craters of other shapes.

6.1.1 Modeling setup

Consider a specimen containing a hemi-spherical crater with radius a. The specimen rests on a flat rigid substrate. We suppose that the specimen is made of rubber, that is, it is capable of sustaining large elastic strains. The air inside the crater is the same as in the ambient environment, and it is characterized by the atmospheric pressure p_a, volume V_0, and molecules N_0.

The suction effect is realized in two stages:

1. The specimen is compressed, so that the air is squeezed out of the crater; at the end of this stage, the remaining air in the crater is characterized by the triplet (p_1, V_1, N_1).
2. The specimen is unloaded, so that the crater springs back. This action results in a pressure drop associated with the suction effect. At the end of this stage, the air in the crater is characterized by the triplet (p_2, V_2, N_2).

Accordingly, the pressure drop is

$$-\Delta p = p_1 - p_2$$

and the suction force is

$$F = -\Delta p A_2 \tag{6.1}$$

where A_2 is the projected area of the crater at the end of Stage 2.

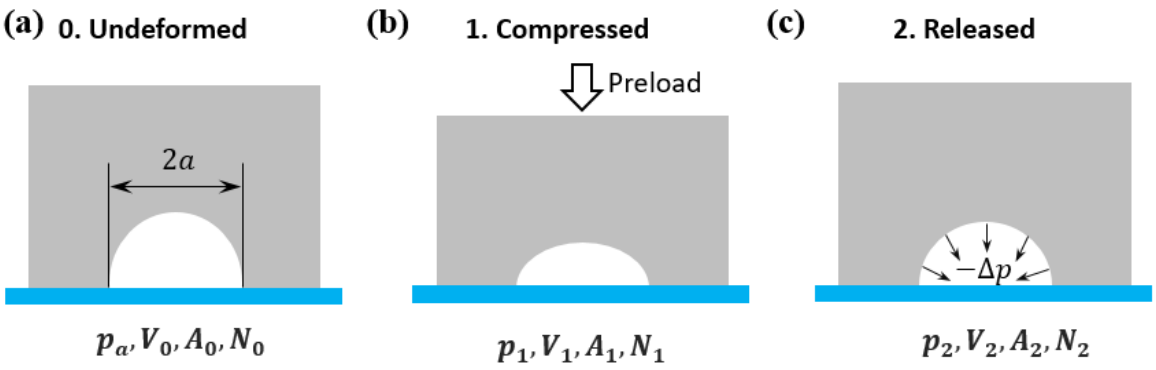

Figure 6.1 A loading-unloading cycle that produces the suction effect: (a) A specimen with an isolated hemi-spherical crater of radius a resting on a flat plate (blue); (b) The specimen is preloaded in compression and the air is squeezed out of the crater; (c) The preload is released, and the springback induces vacuum in the crater. The symbols p, V and N denote the pressure, volume, and number of molecules of air inside the crater at each state.

A complete analysis of the two-stage process requires one to model the airflow dynamics. Preliminary results presented in this dissertation are obtained by adopting the following assumptions:

1. The air flows freely out of the crater upon loading, so that $p_1 = p_a$.

2. No air exchange takes place upon unloading, so that $N_1 = N_2$.

3. The entire process is isothermal and the air is an ideal gas, so that $p_1 V_1 = p_2 V_2$.

As a result, the expression for the suction force becomes

$$F = \left(1 - \frac{V_1}{V_2}\right) p_a A_2 \tag{6.2}$$

The first assumption that the liquid can flow out freely when compressed is inspired by prior works on thin-walled suction cups [163, 167, 169]. In these models [163, 167, 169], analytical relationship between preload and suction-cup deformation has been obtained by neglecting gas resistance during compression. As for the second assumption that there is no leakage during unloading, it is consistent with experimental observations for thin-walled suction cups[163, 167, 169] as well as surface craters[69].With the adopted assumptions, the dynamics of airflow is regarded as a sequence of static equilibrium states. Consequently, it becomes sufficient to analyze the two-stage process in the context of solid mechanics.

In the remainder of this section, we describe an experimental setup designed to conform with the adopted assumptions. Further, we show that the experimental results can be accurately predicted using nonlinear elasticity theory alone. That is neglecting the airflow dynamics appears to be a good assumption.

6.1.2 Experimental Setup

The experimental setup was designed so that it realizes the two-stage process under conditions that well represent the adopted assumptions. We choose polydimethylsiloxane (PDMS, Sylgard 184 Dow Corning) to make our specimens as it is a quintessential rubber with negligible rate-dependence in the time-temperature range in our experiments [170]. Cylindrical specimens with diameter 25.40 mm and height 35.13 mm was molded from PDMS with the base-to-curing-agent mass ratio equal to 30:1, and then cured at 70℃ for 12 hours. A hemi-spherical crater of diameter 12.70 mm was placed at the center of a circular face.

Pure rectangular prisms without crater were also made for identifying material properties. The dimensions of the prisms were 25×25×40 mm^3. To this end, we conducted a uniaxial compression test using a Dynamic Mechanical Analyzer (DMA) (RSA-G2, TA Instruments). The top and bottom surfaces of the specimen were lubricated by performance oil (Fellowes Powershred Performance Shredder Oil) such that the specimen was under uniaxial stress. The loading velocity was set at 3 mm/min, which corresponds to a nominal strain rate of 1.25×10^{-3} s^{-1}, so that the deformation was dominated by rubber elasticity. The axial load-displacement data were converted into the nominal stress σ versus the principal stretch λ data and fitted by the incompressible Neo-Hookean model

$$\sigma = \mu\left(\lambda - \frac{1}{\lambda^2}\right) \tag{6.3}$$

where the shear modulus μ is the small strain shear modulus as well as a fitting parameter. As shown in Figure 6.2, this model fits the experimental data very well for $\mu =$ 47.3 kPa.

Direct measurements of the suction force upon unloading are difficult. Therefore we performed the loading-unloading experiments on the specimens and measured the pull-off force rather than suction force. These data can be used for calculating the suction force.

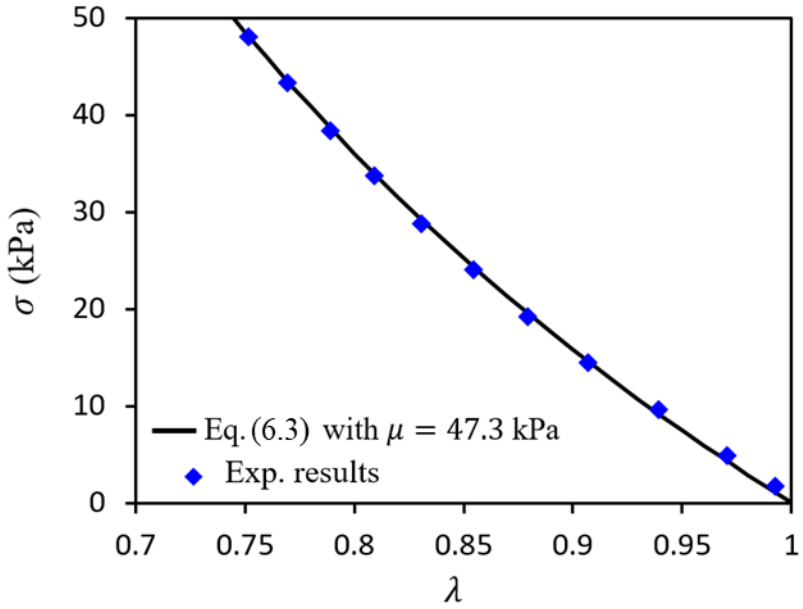

Figure 6.2 Nominal stress σ versus the principal stretch λ. The data were obtained using pure rectangular specimens subjected to uniaxial compression, and fitted based on the incompressible Neo-Hookean model for μ=47.3 kPa.

To realize experimental conditions that well represent the adopted assumptions, we built a special platform as illustrated by a schematic in Figure 6.3 (a) and a photograph in Figure 6.3 (b). The cratered specimen was compressed against a stiff acrylic platform. At the platform center, we drilled a ventilation hole with diameter of 0.8 mm, which was used for releasing and trapping the air in the crater. During the first stage, consistent with the first assumption, the hole was opened. During the second stage, consistent with the second assumption, the hole was sealed. Both stages were realized using a 3 mm/min loading velocity. Similar to the pure rectangular prism, the top and bottom surfaces of the cratered specimens were lubricated. To measure the pull-off force, the second stage involved not only unloading but also retraction. That is, during the second stage, the specimen was stretched beyond the unloading point, until the cratered surface was pulled off the platform. The load-displacement data for both pure prismatic and cratered specimens are shown in Figure 6.3 (c) and Figure 6.3 (d). There we identify the loading, unloading, and retraction stages, and the pull-off force. Note that the two sets of data are qualitatively similar. Nevertheless, quantitative differences are significant enough to identify the suction effect.

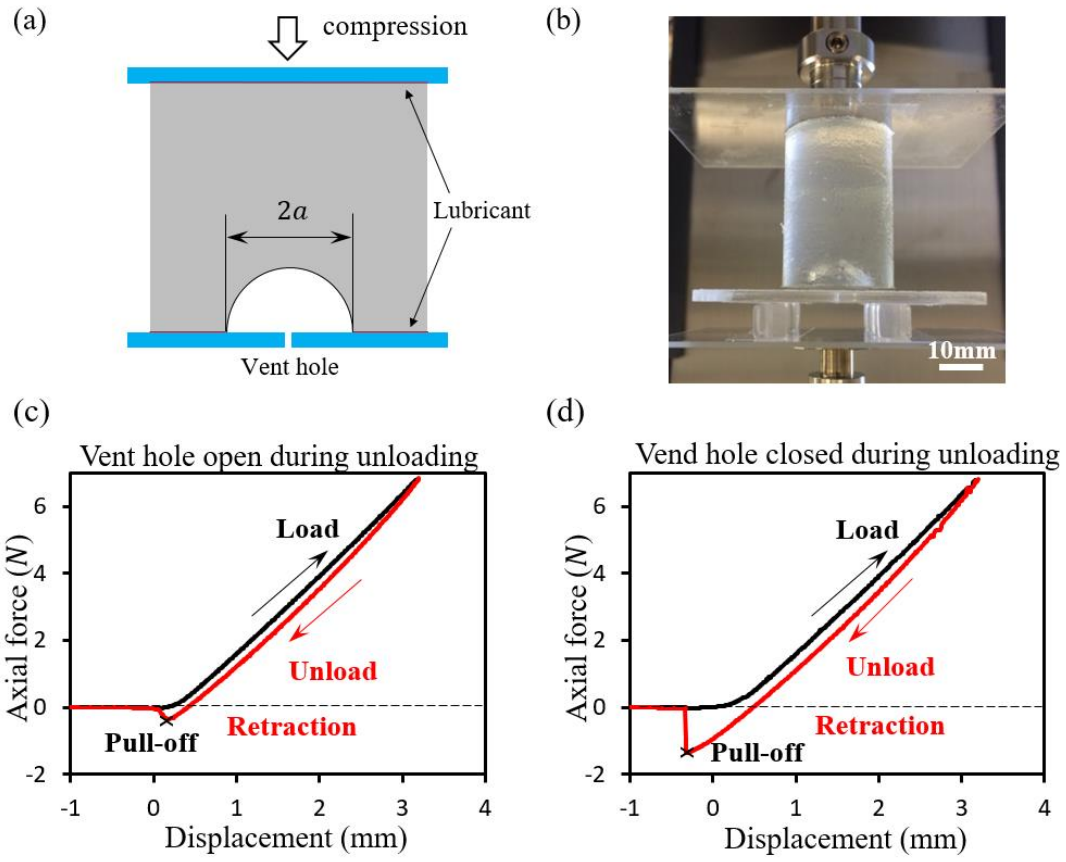

Figure 6.3 A schematic drawing (a) and a photograph (b) of the experimental platform. The small ventilation hole drilled in the bottom plate is open during loading and closed during unloading. Load-displacement curves with vent hole open (c) and closed (d) during unloading. Peak compressive strain was 10%. Loading, unloading, retraction stages, and the pull-off points are identified.

In both testing systems, the top and bottom surfaces of the specimen were still lubricated by performance oil (Fellowes Powershred Performance Shredder Oil) such that the specimen was free of friction and loaded under uniaxial stress.

Because the suction force induced by pressure drop inside the crater (Δp) only depends on the different liquid pressure inside the crater (i.e. p_1 and p_2) instead of the ambient, it was only necessary to fill the crater with incompressible liquid and perform the measurement in air. To realize experimental conditions that well represent the adopted assumptions, we built a special platform as illustrated by a schematic in Figure 6.3 (a) and a photograph in Figure 6.3 (b). The cratered specimen was compressed against a stiff acrylic platform. At the platform center, we drilled a ventilation hole with diameter of 0.8 mm, which was used for releasing and trapping the liquid in the crater. During the first stage, consistent with the first assumption, the vent hole was kept open. During the second stage, consistent with the second assumption, the hole was sealed. Both stages were realized under a 3 mm/min loading velocity. To measure the pull-off force, the second stage involved not only unloading but also retraction. That is, during the second stage, the specimen was stretched beyond the unloading point, until the cratered surface was pulled off the platform. This pull-off force is denoted as F'. To extract the suction force, we performed the same loading-unloading experiments with the vent hole open throughout the test and the collected pull-off force is denoted as F''. Representative load-displacement curves for both cases are plotted in Figure 6.3 (c) and Figure 6.3 (d). There we identify the loading, unloading, and retraction stages, as well as the pull-off force. Note that the two

sets of data are qualitatively similar. Nevertheless, quantitative differences are significant enough to identify the suction effect.

The experimentally collected pull-off force F' is a resultant force of the adhesion strength over the specimen/platform interface and the suction force over the crater, whereas F'' only consists of the interface adhesion. Thus, the difference in value

$$F = F' - F'' \tag{6.4}$$

produces the suction force inside the crater at pull-off as illustrated by the free body diagram in Figure 6.4 (a), the suction force $F' - F''$ is plotted against the preload ϵ, which is the peak macroscopic axial strain defined as

$$\epsilon = -\Delta L/L \tag{6.5}$$

where L is the specimen axial length. Solid dots denote results measured are by DMA while hollow dots are measured by MTS. In general, craters can produce stronger suction force when larger compression is applied. Note that experimental results from DMA were limited to $0 \leq \epsilon \leq 0.32$, which is associated with the allowable load of the DMA used in the experiments. At $\epsilon \approx 0.32$, we measured pull-off forces by both DMA and MTS, and the corresponding results are in good agreement for craters filled with both liquid and air. This justifies the consistence between the experiments performed via DMA and MTS.

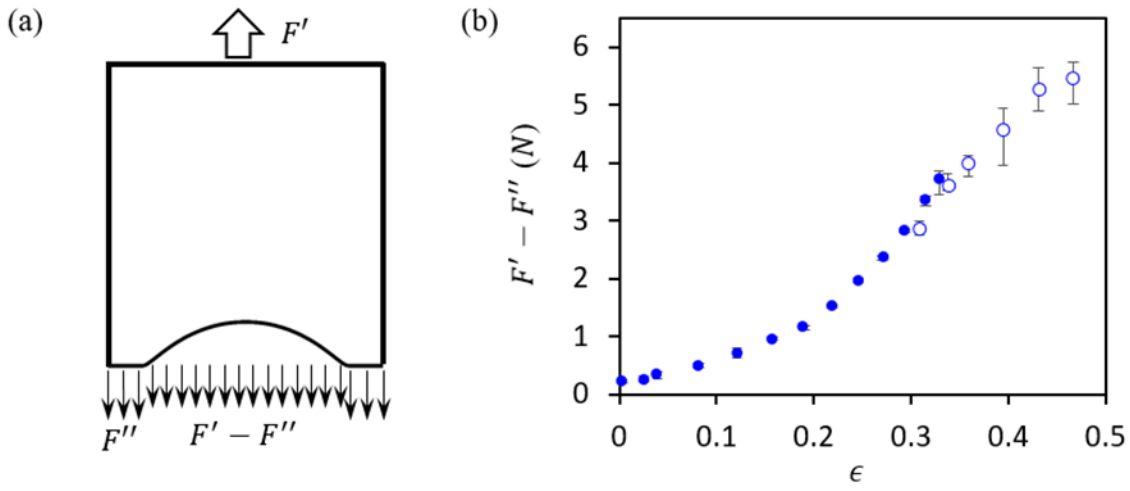

Figure 6.4 (a) A schematic of the free body diagram of a specimen at pull-off. (f) Experimentally measured suction forces ($F'-F''$) of air-filled craters. Data obtained by DMA are represented by solid dots and MTS by hollow circles.

6.1.3 Finite Element Analysis

Following experimental data for the pure prismatic specimens, we assumed that the constitutive behavior of the cratered specimens is described by the incompressible Neo-Hookean constitutive model with $\mu = 47.3$ kPa. To simplify the analysis, we applied axisymmetry, and the specimen/substrate interface was assumed to be frictionless (Figure 6.5). Also we neglected any surface tension effects simply because

$$\frac{\gamma}{a\mu} \approx \frac{2 \times 10^{-2}\ N/m}{(10^{-2}\ m) \times (4 \times 10^{4}\ N/m^2)} = 5 \times 10^{-5} \ll 1 \qquad (6.6)$$

where γ is the surface tension of PDMS [171].

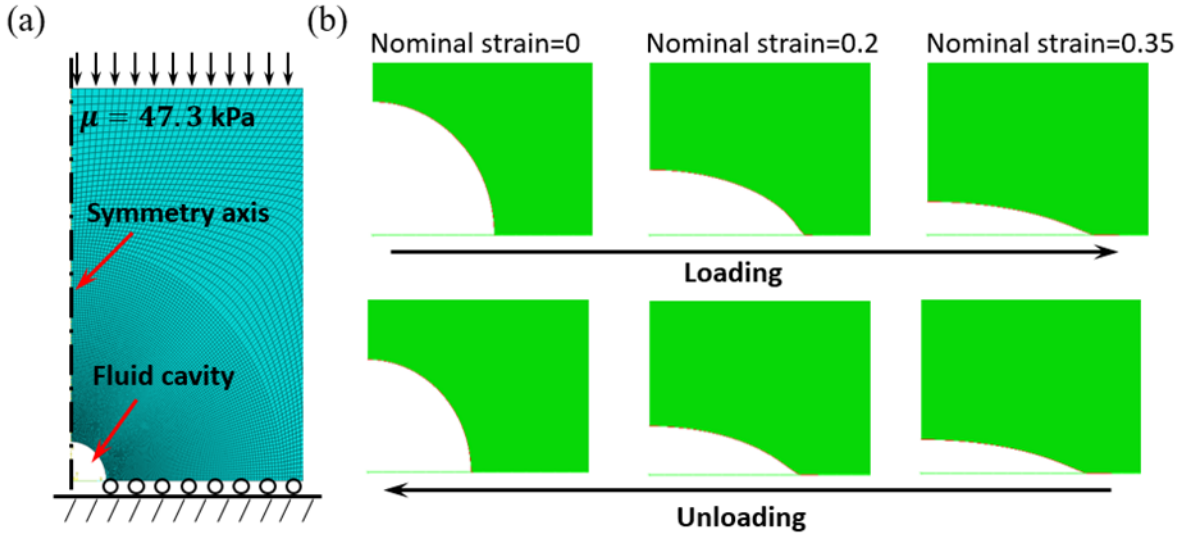

Figure 6.5 A finite element mesh for an axisymmetric crater model. (b) A deformation sequence of a specimen in a loading-unloading test: top row for loading stage and bottom row for unloading stage.

We used finite element simulations to compute the relationship between the suction force $F = -\Delta p A_2$ and the preload ϵ. All simulations were conducted using Abaqus. The finite element mesh formed by CAX4H elements is shown in Figure 6.5 (a); this mesh was selected using basic convergence tests. We used the option *FLUID CAVITY which is ideal for modeling both stages of the gas-solid interactions.

Figure 6.5 (b) shows a sequence of deformed configurations of a specimen with hemi-spherical crater in a loading-unloading test. The first panels in top and bottom rows are the initial (before loading) and final (end of unloading) configurations, respectively. The third panels in each row correspond to the end of loading with ϵ =0.35, and the rest are intermediate states. At the end of the unloading, the finite element results indicate that the crater maintains the spherical symmetry.

6.1.4 Linear Elasticity Analysis

In this section, we present linear elasticity analysis of the problem based on Eshelby's formalism [172]. We treat the crater as an isolated hemi-spherical crater in a semi-infinite specimen, and take advantage of the assumption that the contact between the specimen and the substrate is frictionless. This allows us to replace the problem for semi-infinite specimen containing a hemi-spherical crater with an infinite specimen containing a spherical cavity. This problem is straightforward to analyze using Eshelby's formulism

According to Eq. (6.2), we need to calculate V_1, V_2, and A_2. Note that according to classical linear elasticity, the quantities $\Delta V_1 = V_1 - V_0$, $\Delta V_2 = V_2 - V_0$, and $\Delta A_2 = A_2 - A_0$ are infinitesimal. This allows us to replace A_2 with A_0. However, computing ΔV_1 and ΔV_2 is essential for meaningful calculation of the suction force.

To compute ΔV_1, we subject the infinite specimen to remote uniaxial compressive strain ϵ. For this case, Eshelby's formulism yields

$$\Delta V_1 = -\frac{3}{2}(1-\nu)\epsilon V_0 \tag{6.7}$$

where ν is the Poisson's ratio of the specimen material, and for incompressible material, we have $\nu = 1/2$.

To compute ΔV_2, we subject the cavity to the surface traction

$$\boldsymbol{t} = (p_1 - p_2)\boldsymbol{n} = (p_a - p_2)\boldsymbol{n} = -\Delta p \ \ \boldsymbol{n} \tag{6.8}$$

where $\boldsymbol{n}$ is the outward normal. As far as ΔV_2 is concerned, this problem is equivalent to the superposition of two problems. In the first problem, the specimen is uniformly loaded

by $-\Delta p$ on both cavity and remote surfaces. In the second problem, the cavity surface is traction-free and the remote surface is subjected to Δp. As a result, we obtain

$$\Delta V_2 = \frac{3}{4}\ \frac{\Delta p}{\mu} V_0 \tag{6.9}$$

where

$$\Delta p = -\left(1 - \frac{V_1}{V_2}\right) p_a \tag{6.10}$$

Therefore, one can calculate the suction force

$$F = \frac{1}{2}\left[\left(1 + \frac{4\mu}{3p_a}\right) - \sqrt{\left(1 + \frac{4\mu}{3p_a}\right)^2 - 8(1-\nu)\frac{\mu}{p_a}\epsilon}\right] p_a A_0 \tag{6.11}$$

6.1.5 Results

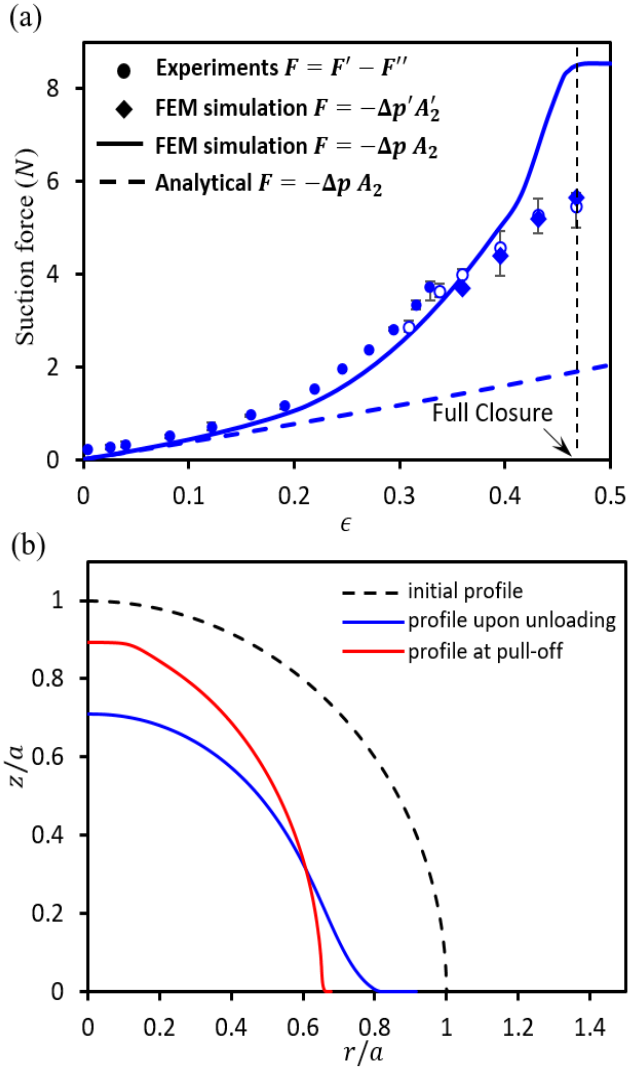

Figure 6.6 (a) Comparisons of suction forces obtained by experimental measurements (circular markers), analytical modeling (dashed curves) and finite element simulation (solid curves and diamond markers). (b) Finite element simulation results of crater profiles upon unloading (blue curve) and at pull-off (red curve) at $\epsilon = \epsilon_f$. Dashed curve represents the initial profile of the hemi-spherical crater.

Comparisons of experimental (circular markers), simulation (solid curve), and analytical (dashed curve) results are shown in Figure 6.6 (a), where the suction force is plotted versus the preload ϵ. In the range of $0 \leq \epsilon \leq 0.36$, experimental and simulation results are in good agreement, which validates the use of the modelling assumptions, as well as extending the simulations for characterizing more general situations under loading range $0 \leq \epsilon \leq 0.36$. The calculated suction force $-\Delta p A_2$ using linear elasticity analysis is plotted as the dashed blue curve in Figure 6.6 (a). It is clear that the linear analysis is valid for small strains, and deviates significantly from the experimental and simulation results for $\epsilon > 0.1$, and therefore its usefulness is rather limited.

Under large preload, especially when craters reach full closure upon loading, finite element simulation shows considerable discrepancy from experimental results. One source of the discrepancy comes from the different definitions of suction force used in experiments and simulations. In experiments, $F' - F''$ represents the suction force inside the crater at pull-off, while in simulations, $-\Delta p A_2$ is the suction force at the end of unloading and before retraction. At small preload, it is fair to argue that the crater has similar configuration at pull-off point with that upon fully unloading, so that

$$F' - F'' \approx -\Delta p A_2 \tag{6.12}$$

is expected. This is true under loading range $0 \leq \epsilon \leq 0.32$ based on the observation from Figure 6.6 (a). However, the approximation in Eq. (6.12)*(6.12)* will no longer hold once significant difference exists between the pull-off status and the fully unloading status. In finite element simulations, experimentally measured retraction strain at pull-off, ϵ_t, can

be applied after unloading. Resulted suction forces, $F = -\Delta p' A_2'$, are plotted as blue diamonds in Figure 6.6 (a), where $\Delta p'$ and A_2' represent the finite element results of pressure drop inside the crater and the projected area of the crater at "pull-off", respectively. It is found that $\Delta p'$ doesn't differ from Δp significantly (relative error < 1%), but A_2' is considerably smaller than A_2, as shown in Figure 6.6 (b). In Figure 6.6 (a), the good agreement between $F = -\Delta p' A_2'$ and $F' - F''$ indicates that, for air-filled craters, the discrepancy between finite element simulation and experimental results can be fully explained by the difference in $-\Delta p A_2$ and $F' - F''$.

Thus, to accurately predict the suction force at pull-off, one needs the traction-separation behavior of the specimen/platform interface, which is out of our focus. So, we would focus on the study of the suction force $-\Delta p A_2$ upon unloading only.

6.2 SPHERICAL-CAP-SHAPED CRATERS

In this section, we extend the simulation approach developed for hemi-spherical craters to spherical-cap-shaped (SCS) craters. Our focus is on maximizing the suction force by optimizing the crater shape and specimen mechanical properties. Since our analysis is limited to large specimens, the only dimensionless geometric parameter involved is

$$\frac{b}{a} \tag{6.13}$$

where a is crater base radius and b is the crater height (Figure 6.7 (a)). The dimensionless stiffness parameter is defined as

$$\frac{\mu}{p_a} \tag{6.14}$$

In the previous section, these parameters were fixed at $a/b = 1$ and $\mu/p_a = 0.47$ for a hemispherical crater in the ambient environment. Further, in the previous section, the preload ϵ was varied. In contrast, in this section, this parameter is set to be ϵ_f, which is the preload so that the crater attains a full closure and realizes complete vacuum. With this provision $V_1 = 0$, and the suction force is computed from Eq. (6.2) as

$$\hat{F} = -\Delta p A_2/(p_a A_0) \tag{6.15}$$

The normalized suction force $\hat{F}$ as a function of b/a and μ/p_a can be produced using finite element simulations, and is presented as a contour plot Figure 6.7 (b). This plot clearly demonstrates that large $\hat{F}$'s are realized by specimens with large b/a and μ/p_a. But the dependence of $\hat{F}$ on b/a and μ/p_a is not monotonic.

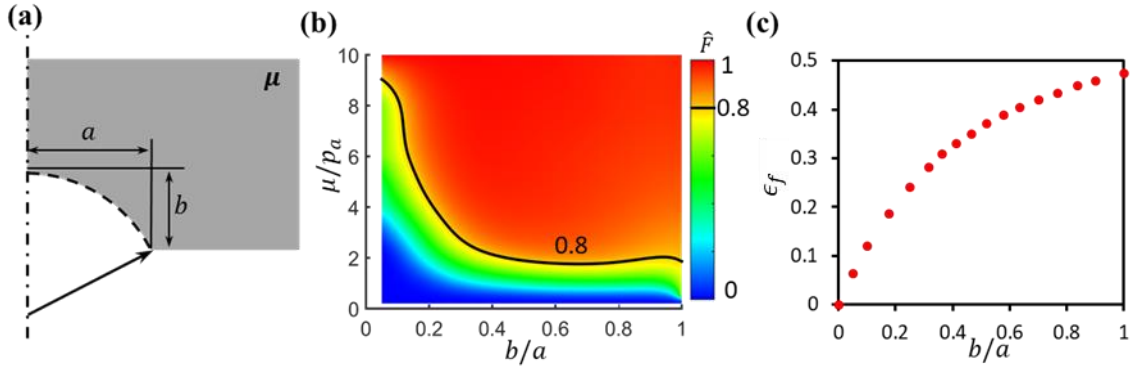

Figure 6.7 (a) A schematic of the spherical-cap-shaped (SCS) crater. (b) A contour plot for the normalized achievable suction force $\hat{F}$ as a function of b/a and μ/p_a. (c) Minimum preload strain for closure ϵ_f as a function of b/a.

Further, for sufficiently stiff specimens, the dependence on α is relatively weak. We identify "good" specimens as those for which $\hat{F} > 0.8$; the rest of the specimens are regarded as "bad". This (arbitrary) classification is represented by the black curve in Figure 6.7 (b). In Figure 6.7 (c), we present ϵ_f as a function of a/b; apparently ϵ_f is independent of μ/p_a. As expected, deep craters require large ϵ_f.

To gain further insight into simulation results, we present the deformed shape of twelve specimens upon full unloading corresponding to $\alpha =$ 0.25, 0.5, 0.75, 1 and $\beta =$ 0.5, 1, 10 (Figure 6.8). The dashed lines show the initial craters. It is clear from that stiff specimens with deep craters are capable of recovering in a way that $A_2 \approx A_0$ and therefore for such specimens $\hat{F} \approx 1$. In contrast, soft specimens with shallow craters result in $A_2 \ll A_0$ and therefore very small.

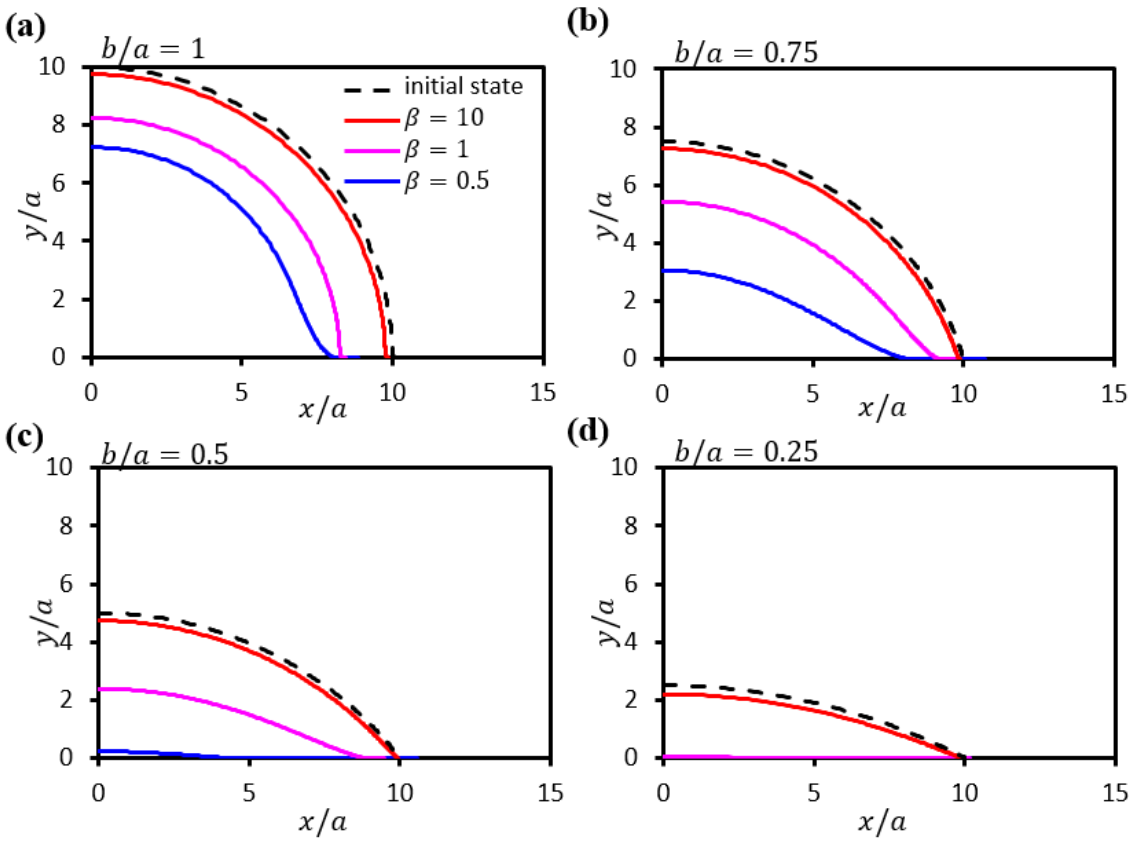

Figure 6.8 Deformed (solid lines) and undeformed (dashed lines) shapes of craters. The deformed shapes correspond to complete unloading.

6.3 CHAPTER SUMMARY

In this work, we established a framework for quantifying the suction force generated by a macroscopic crater. For the sake of simplicity, we assume frictionless interface between the crater and the flat substrate. We also neglect the surface tension effect as our size of samples are much large than the elaso-capillary length. Linear elasticity solution has been obtained using Eshelby's formulism, which breaks down at large preload. Both experiments and finite element analysis have been carried out, which mutually agree with each other for a hemi-spherical crater. The finite element analysis was then adopted to characterize craters of other shapes, i.e., spherical-cap-shaped in this Chapter. We found that the suction force show a non-monotonic dependence on the aspect ratio of the crater as well as the material stiffness. In stiff materials, one can realize large suction forces by optimizing the crater shape.

Chapter 7 Effect of Surface Tension on Isolated Miniaturized Craters[6]

In Chapter 6, we developed a framework for quantifying the suction forces produced by isolated macroscopic craters neglecting surface effects. In this chapter, we take surface tension into consideration because it plays a significant role in microscale craters on soft polymers. We have derived linear and nonlinear elastic solutions for the elasto-capillary distortion in miniature hemi-spherical craters when they are demolded from the template. By implementing a user-element subroutine in finite element modeling (FEM), we have also simulated the demolding, compression, and unloading processes of the craters subjected to surface tension under large deformation. We discover that reinforcing the crater surface by a thin and stiff shell can help sustain the crater shape after demolding. The effects of shell thickness and stiffness are quantitatively investigated through FEM and optimal parametric combinations are identified.

[6] L. Wang, S. Qiao, N. Lu*, Effects of surface tension on the suction forces generated by miniature craters. *Extreme Mechanics Letters*, 5: 130-138. Jul. 27, 2017.(L. Wang conducted the theoretical analysis, finite element simulation, and wrote the paper)

7.1 INTRODUCTION

Commonly used fabrication method for miniature craters is molding. The molding templates are created using either micromachining [67] or colloidal lithography [66, 164]. Such methods worked well for UV resin [164] whose modulus is in the GPa range and 10:1 PDMS [66] whose modulus is in the MPa range. However, when researchers tried to mold 40:1 PDMS (shear modulus μ =52 kPa) with μm-sized craters, they found that after peeling off PDMS from the template, i.e. demolding, the craters in PDMS appeared to be much smaller than the domes on the molding template. After coating stiffer PDMS layers on the template before molding 40:1 PDMS, the craters were able to preserve the template shape very well after demolding [67]. We attribute the self-collapse of miniature craters on soft polymers after demolding to the so-called elasto-capillary phenomena [173, 174].

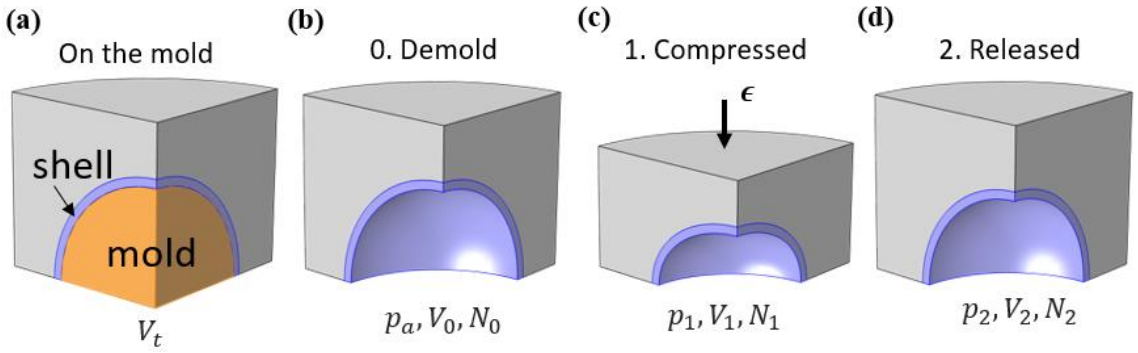

Figure 7.1 Schematics for the deformation process of an isolated hemi-spherical crater with reinforcing shell. (a) Crater on the mold whose volume is defined by the molding template, V_t; (b) State 0: after demolding, the crater volume contracts to V_0 merely due to surface tension. (c) State 1: preload ϵ is applied on the specimen to squeeze the crater to volume V_1; (d) State 2: crater volume recovers to V_2 after unloading.

To elaborate on how the elasto-capillary phenomena can affect the miniature craters, let's consider a crater of radius r in a polymer whose shear modulus is μ and surface energy density is γ. If constant surface energy density is assumed, surface tension would equal to surface energy density γ [175]. Since the total surface energy scales as γr^2 while the volumetric strain energy scales as μr^3, we can define a dimensionless elasto-capillary number

$$\Gamma = \gamma \ /(\mu r) \tag{7.1}$$

to represent the ratio of surface energy to strain energy. When the polymer is very stiff (μ is large) and/or the crater is very big (r is large), Γ would approach zero, which means the surface energy would be negligible compared with the elastic strain energy and therefore the crater cannot be deformed by surface tension. However, when the polymer is ultra-soft (μ is small) and when the crater is in micro- or nano-scale (r is small), Γ can be so large that the effects of surface tension is no longer negligible. In this case, the crater will try to reduce the surface energy (or surface area) through mechanical deformation. Experimentally, such elasto-capillary phenomena have been widely reported when Γ is near 1 [173, 174, 176, 177]. Specific to craters, let's consider the experiments carried out by Choi *et al*. [67] where they tried to mold μm-sized craters out of 40:1 PDMS whose μ =52 kPa, γ = 20 mN/m [178, 179], and $r \sim 0.5$ μm. Plugging into Eq. (7.1), we find $\Gamma = 0.769$, which suggests that due to surface tension, the crater may shrink significantly to reduce its surface area after demolding. Adding a stiff reinforcing shell to the crater proved to be an effective way to sustain the crater shape [67]. However, a quantitative

characterization of the effects of surface tension and reinforcing shell on the suction force generated by those craters is still missing.

Following a framework developed for isolated macroscopic craters neglecting surface effects in Chapter 6 [180], here we analyze isolated hemi-spherical craters with reinforcing shells subjected to surface tension. The process of suction generation is illustrated using a quarter of the crater in Figure 7.1. When the specimen is just cured and still on the molding template, the volume of the crater is denoted by V_t(Figure 7.1(a)). After demolding, the crater contracts due to surface tension (Stage 0). At the end of Stage 0, the air inside the crater is the same as the ambient air so it is characterized by pressure p_0, volume V_0, and number of molecules N_0 (State 0, Figure 7.1(b)). The suction effect is then realized in the following two stages:

Stage 1: the specimen is compressed by a nominal strain of ϵ, named the preload, against a flat plate (not shown in Figure 7.1(c)), such that air is squeezed out of the crater. At the end of this stage, the remaining air in the carter is characterized by the triplet (p_1, V_1, N_1) (State 1, Figure 7.1(c)).

Stage 2: the specimen is unloaded and the crater springs back. This action results in a pressure drop inside the crater which produces the suction force. At the end of this stage, the air in the crater is characterized by the triplet (p_2, V_2, N_2) (State 2, Figure 7.1(d)).

Accordingly, the pressure drop is

$$-\Delta p = p_1 - p_2$$

and the suction force is

$$F = -\Delta p A_2 \tag{7.2}$$

where A_2 is the projected area of the crater at State 2.

Key assumptions adopted in this paper are:

1. The air flows freely out of the crater upon loading (Stage 1), so that $p_1 = p_0$.
2. No air exchange takes place upon unloading (Stage 2), so that $N_2 = N_1$.
3. The entire process is isothermal and the air is an ideal gas, so that $P_1 V_1 = P_2 V_2$.

As a result, the pressure drop can be related to the crater volumes as

$$-\Delta p = \left(1 - \frac{V_1}{V_2}\right) p_0 \tag{7.3}$$

Therefore, the suction force becomes

$$F = \left(1 - \frac{V_1}{V_2}\right) p_0 A_2 \tag{7.4}$$

In the following section, we simply assume that the crater is sitting in the air such that initial pressure equals the atmospheric pressure, i.e., $p_0 = p_a$. We will quantitatively characterize the effects of surface tension and reinforcing shell on crater performance. Linear and nonlinear elastic formulation for Stage 0 and nonlinear elastic finite element modeling (FEM) of all three stages are described. Analytical and FEM results are presented.

7.2 METHODS

7.2.1 Linear Elasticity Solutions for Stage 0

Given the axisymmetry of the specimen, this problem can be analyzed as a 2-D problem. By neglecting the interfacial shear stress between the specimen and the flat plate and by overlooking the surface tension effects at the rim of the crater, the hemi-spherical crater can be mirrored to a spherical cavity embedded in a polymer matrix (Figure 7.2 (a)). The matrix dimension is assumed to be much larger than the cavity size such that the matrix can be treated as infinitely large. The initial radius of the crater is R_t (as defined by the molding template shown in Figure 7.1 (a)) and the shear modulus of the polymer matrix is μ_m. Surface tension can be interpreted as a normal traction applied on the surface of the spherical cavity [181-183]:

$$t_n = \gamma\kappa \tag{7.5}$$

where κ is the sum of the two principal curvatures, which equals to $2/R_t$ initially.

We first solve the problem using linear elasticity in a polar coordinates defined in Figure 7.2 (a) by adopting Lur'e solution [184] . The displacement and stress fields can be expressed as

$$\begin{aligned} U_r &= Fr + \frac{G}{r^2} + P_2(cos\,\phi) \times [12A\nu\, r^3 + 2Br + 2C\frac{5-4\nu}{r^2} - 3\frac{D}{r^4}] \\ U_\phi &= \frac{dP_2(\cos\phi)}{d\phi} \times [(7-4\nu)A\, r^3 + Br + 2C\frac{1-2\nu}{r^2} + \frac{D}{r^4}] \end{aligned} \tag{7.6}$$

$$\frac{\sigma_{rr}}{2\mu_m} = \left[2B - \frac{2C}{r^3}(10-2\nu) + \frac{12D}{r^5}\right]P_2(cos\,\phi) + \frac{F(1+\nu)}{1-2\nu} - \frac{2G}{r^3}$$

$$\frac{\sigma_{r\phi}}{2\mu_m} = [B + \frac{2C}{r^3}(1+\nu) - 4\frac{D}{r^5}]\frac{dP_2(cos\,\phi)}{d\phi} \tag{7.7}$$

where U_r and U_ϕ are the displacements of cavity surface in the radial and hoop directions, respectively, and σ_{rr} and $\sigma_{r\phi}$ are the normal and shear stresses, respectively. $P_2(cos\,\phi) = 1/2(3cos^2\phi - 1)$ is the Legendre Polynomial of order two and ν is the Poisson's ratio of the polymer matrix. Coefficients A through G are to be determined by boundary conditions.

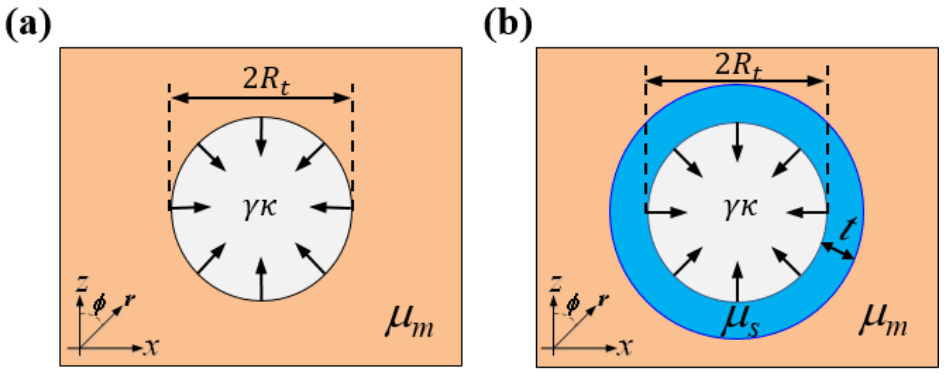

Figure 7.2 Effective boundary value problems for Stage 0. (a) A spherical cavity of radius R_t inside a matrix of shear modulus μ_m. (b) A reinforcing shell of thickness *t* and modulus μ_s is added. Both the matrix and the reinforcing shell are assumed to be incompressible Neo-Hookean materials.

The boundary conditions of Figure 7.2 can be expressed as: in the far field, $\epsilon_{rr}^{\infty} = 0$; at $r = R_t, \quad \sigma_{rr} = 2\gamma/R_t, \quad \sigma_{r\phi} = 0$. Hence the only nonzero coefficient is found to be $G = -R_t^2\gamma/(2\mu_m)$, which gives the radial displacement of the crater surface $U_r = -R_t\Gamma/2$, where $\Gamma = \gamma/(\mu_m R_t)$ is the dimensionless elasto-capillary number. Therefore, at the end of Stage 0 (i.e. demolding), the hemi-spherical crater will deform to another hemi-sphere with a new radius of

$$R_0 = R_t(1 - \frac{\Gamma}{2}) \tag{7.8}$$

Equation (7.8) shows that the change of crater radius $\Delta R = R_0 - R_t$ is linearly proportional to the elasto-capillary number Γ.

Lur'e formulism, i.e. Eq. (7.6) and Eq. (7.7), can also be applied to solve a spherical cavity with a reinforcing shell subjected to surface tension, as depicted in Figure 7.2 (b). The thickness and shear modulus of the shell is t and μ_s, respectively. In this case, the boundary conditions become: in the far field, $\epsilon_{rr}^{\infty} = 0$; at $r = R_t, \quad \sigma_{rr}^{s} = 2\gamma/R_t, \quad \sigma_{r\phi}^{s} = 0$, where superscript "s" stands for shell. In addition, stresses and displacements should be continuous across the shell-matrix interface, i.e., at $r = R_t + t$, $\sigma_{rr}^{s} = \sigma_{rr}^{m}; \sigma_{r\phi}^{s} = \sigma_{r\phi}^{m}; U_r^{s} = U_r^{m}; U_{\phi}^{s} = U_{\phi}^{m}$, where superscript "*m*" indicates the matrix. Assume both the shell and the matrix are incompressible materials, i.e., $\nu = 0.5$, solving this boundary value problem gives the following radius of crater after demolding:

$$R_0 = R_t\{1 - \frac{\Gamma(1+\beta)^3}{2[(1-\alpha) + \alpha(1+\beta)^3]}\} \tag{7.9}$$

where $\alpha = \mu_s/\mu_m$ is the normalized shell modulus and $\beta = t/R_t$ is the normalized shell thickness. It is obvious that Eq. (7.9).will decay to Eq. (7.8) when $\alpha = 1$ or $\beta = 0$, i.e., when there is effectively no shell. The conclusion that ΔR is proportional to Γ is also true for Eq. (7.9).

7.2.2 Nonlinear Elasticity Solutions for Stage 0

According to Eq. (7.8), if Γ is 2, R_0 should be zero, indicating that the crater would disappear due to large surface tension. Such large deformation violates the small deformation assumption in linear elasticity. In fact, the spherical symmetry of the two cavities in Figure 7.2 dictates that the solution for this problem should be independent of ϕ, which means that the spherical cavity will deform to another spherical shape. Under such premise, nonlinear elasticity solutions may be deduced. First, consider a spherical cavity with initial inner radius R_t (Figure 7.2(a)) and an arbitrary radius R $(R \geq R_t)$ in the reference configuration. When subjected to surface tension (i.e., Stage 0), it deforms to another cavity with inner radius R_0 and the radius R deforms to $r(r \geq R_0)$ in the current configuration. Hence the hoop stretch is defined as $\lambda_\phi(R) = r/R$. The incompressibility of the polymer requires a constant volume of the shell confined by R_t and R, i.e.,

$$R^3 - R_t^3 = r^3 - R_0^3 \tag{7.10}$$

Due to spherical symmetry, the material is under a triaxial stress state $(\sigma_{rr}, \sigma_{\phi\phi}, \sigma_{\phi\phi})$. If incompressibility is considered, superposing a hydrostatic stress $(-\sigma_{rr}, -\sigma_{rr}, -\sigma_{rr})$ on the material will not change the state of deformation. Therefore, the stress state of the material becomes $(0, \sigma_{\phi\phi} - \sigma_{rr}, \sigma_{\phi\phi} - \sigma_{rr})$. The constitutive law for incompressible Neo-Hookean materials in this equibiaxial stress state can be rewritten as

$$\sigma_{\phi\phi} - \sigma_{rr} = \mu_m\left(\lambda_\phi^2 - \lambda_\phi^{-4}\right) \tag{7.11}$$

The nontrivial equilibrium equation of this problem is

$$\frac{d\sigma_{rr}(r)}{dr} + 2\frac{\sigma_{rr} - \sigma_{\phi\phi}}{r} = 0 \tag{7.12}$$

Plugging Eq. (7.11) and Eq. (7.12)and integrating Eq. (7.12) from $r = R_0$ to $r = \infty$ yields

$$\sigma_{rr}|_{r=\infty} - \sigma_{rr}|_{r=R_0} = \mu_m[\frac{5}{2} - 2\frac{R_t}{R_0} - \frac{1}{2}\left(\frac{R_t}{R_0}\right)^4] \tag{7.13}$$

The right hand side is a well-established function group to characterize the large deformation of hyperelastic materials [185], while the left hand side is only associated with boundary conditions in current configuration. Substituting $\sigma_{rr}|_{r=\infty} = 0, \sigma_{rr}|_{r=R_0} = 2\gamma/R_0$ gives an equation relating R_0 to R_t:

$$\frac{\gamma}{\mu_m R_t} = 1 - \frac{5}{4}\left(\frac{R_0}{R_t}\right) + \frac{1}{4}\left(\frac{R_t}{R_0}\right)^3 \tag{7.14}$$

Numerically solving Eq. (7.14) can yield R_0 as a function of R_t

When a reinforcing shell is considered (Figure 7.2), this problem can be solved by adding the continuity conditions at the shell-matrix interface in current configuration, i.e. at $r = r_0:\ \sigma_{rr}^s = \sigma_{rr}^m;\ \sigma_{r\phi}^s = \sigma_{r\phi}^m; \lambda_\phi^s = \lambda_\phi^m$. After derivation, the analytical relation between R_0 and R_t is given by

$$\begin{aligned}\frac{\gamma}{\mu_m R_t} = \alpha - \frac{5}{4}\frac{R_0}{R_t} + \frac{\alpha}{4}\left(\frac{R_t}{R_0}\right)^3 + (1-\alpha)[\frac{(1+\beta)R_0}{r_0} \\ + \frac{1}{4}\frac{R_0}{R_t}\left(\frac{(1+\beta)R_t}{r_0}\right)^4]\end{aligned} \tag{7.15}$$

where $\alpha = \mu_s/\mu_m$ and $\beta = t/R_t$ are as defined before. Similarly, Eq.(7.15) will decay to Eq. (7.14) when $\alpha = 1$ or $\beta = 0$ if we note that $r_0 = R_0$ when $\beta = 0$.

7.2.3 Finite element modeling

We performed FEM using a commercial package ABAQUS/standard 6.13. To simulate curvature-dependent surface tension, we implemented a four-noded isoparametric quadrilateral user-element subroutine (UEL) [186] in all following FEM jobs. Considering the axisymmetry of the problem, in 2-D space, a quarter of a small spherical cavity with radius R_t was built on the surface of a large polymer matrix with lateral size L_0 ($L_0 > 10R_t$) (Figure 7.3). The left and bottom surfaces are modeled as symmetric planes. In accordance with theoretical analysis, we used nearly incompressible Neo-Hookean material, i.e., $\nu = 0.4995$, throughout the simulation. To model large deformation in FEM, nonlinear geometry (NLGEOM) is always on. We first simulated hemi-spherical cavity without reinforcing shell. Detailed procedures for Stages 0 through 2 are described as follows:

Stage 0 (demolding): Apply uniform normal traction $\kappa\gamma$ to the inner surface of the crater to simulate the demolding process. The hemi-spherical crater deforms from initial radius R_t to R_0. The volume of the crater at the end of Stage 0 is $V_0 = 2/3\pi R_0^3$. This step is realized merely by applying the UEL.

Stage 1 (loading): Apply a compressive load of $\epsilon = 0.5$ on the top surface of the specimen. During compression, traction on the crater due to surface tension is still activated but varies at each incremental step with the updated local curvature. This step is completed by applying the UEL and a compressive load of $\epsilon = 0.5$. At the end of this stage, the crater deforms to a shallow dome of volume V_1 which can be calculated via exported nodal coordinates of the inner surface of the crater.

Stage 2 (unloading): Remove the remote compressive load ϵ and apply a positive normal traction with the amplitude of $-\Delta p = p_1 - p_2$ in addition to $\kappa\gamma$ to the surface of the crater. The pressure drop $-\Delta p$ has to be calculated by combining the ideal gas relation and Eq. (15) (see Appendix). This step is finished by deactivating ϵ and simultaneously applying UEL and $-\Delta p$. At the end of Stage 2, the crater volume V_2 can be obtained.

In fact, Stage 2 FEM is not necessary because $-\Delta p$ can be obtained analytically (see Appendix) once V_1 is obtained by Stage 1 FEM. Therefore, Stage 2 FEM serves as a validation for the nonlinear elasticity theory.

Boundary conditions for those three stages are illustrated in Figure 7.3. The contours plot the magnitude of normalized displacement with constant $\Gamma = 1$ in all stages. The shape of the crater before demolding is highlighted by the red dashed curve in Figure 7.3 (a) and (d). After demolding, the profile of the crater is given in Figure 7.3 (b) and is also drawn as the black dashed curve in Figure 7.3(d). Figure 7.3 (c) shows that after $\epsilon = 0.5$ is applied, the crater is compressed to a very shallow dome and the arrows inside the cavity indicate the nonuniform normal traction (i.e. surface tension) arising from nonuniform local curvature.

Such three-stage FEM procedure can also be applied to quantify the effects of a reinforcing shell by simply modifying the geometry and material properties of the elements near the cavity.

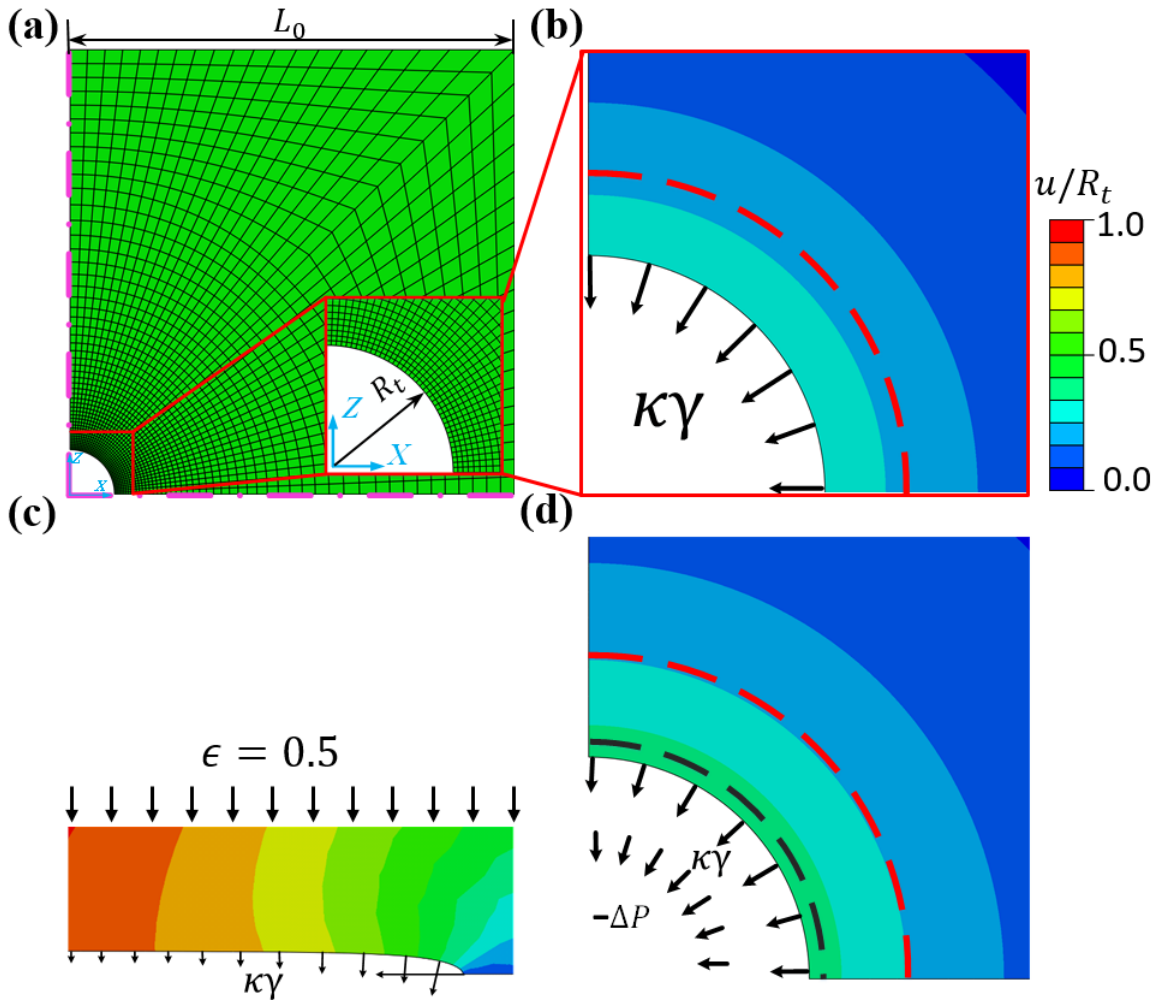

Figure 7.3 (a) FEM mesh of an axisymmetric crater model with a magnified view of the refined mesh near the crater. (b)-(d) Contour plots of normalized total displacement with $\Gamma = 1$ at (b) State 0 where initial crater boundary is marked as red dashed curve; (c) State 1 with a preload of $\epsilon = 0.5$; (d) State 2 where initial and State 0 crater shapes are represented by red and black dashed curves, respectively.

7.3 RESULTS

7.3.1 Crater Volume at the end of Stage 0

Regarding the demolding process (Stage 0), linear elasticity analysis concludes that when there is no reinforcing shell, the change of the crater radius (ΔR) is linearly proportional to the elasto-capillary number (η). When a reinforcing shell is introduced, crater contraction can be suppressed and the radius after demolding is given by Eq. (7.9). To reveal the effects of shell stiffness (α) and thickness (β), we consolidate the surface tension effect by normalizing $\Delta R/R_t$ by $-\Gamma/2$ and plot the linear elasticity results in Figure 7.4 (a) and (b) where the red horizontal lines represent unreinforced craters. It is manifest that for a given Γ, increasing α and β will both impede the radius shrinkage due to surface tension. Specifically, $\alpha = 30$ and $\beta = 1$ are obtained from a reported experiment where $\mu_m = 52$ kPa, $\mu_s = 1.6$ MPa, and $t = R_t = 0.5$ μm [67]. Figure 7.4 suggests that when $\alpha = 30$ (green curve), a small value of β, say $\beta = 0.1$, will significantly resist the crater from shrinking. When $\beta = 1$ (green curve), Figure 7.4 (b) indicates that such a thick shell will only need $\alpha = 10$ to effectively protect the cavity from collapsing.

In contrary to linear elasticity solutions, radius change predicted by nonlinear analysis in Section 2.2 is no longer proportional to Γ. Analytical and FEM results of radius change as a function of Γ, α and β are presented in Figure 7.4 (c) and (d). While our nonlinear analysis fully agrees with the FEM results, the linear theory is only valid up to about $\Gamma = 0.5$. When Γ is beyond 0.5, the linear theory would greatly overestimate the

radius change. For example, the linear theory predicts that the unreinforced crater should disappear when $\Gamma = 2$ whereas the nonlinear analysis only yields $\Delta R/R_t = -0.47$. For craters of $r \sim 0.5$ μm on the surface of 40:1 PDMS [67], $\Gamma = 0.769$, which should be modeled by the nonlinear theory. When $\alpha = 30$ and $\beta = 1$ (green curves in Figs. 4c and 4d), the radius shrinkage is almost negligible even at very large Γ.

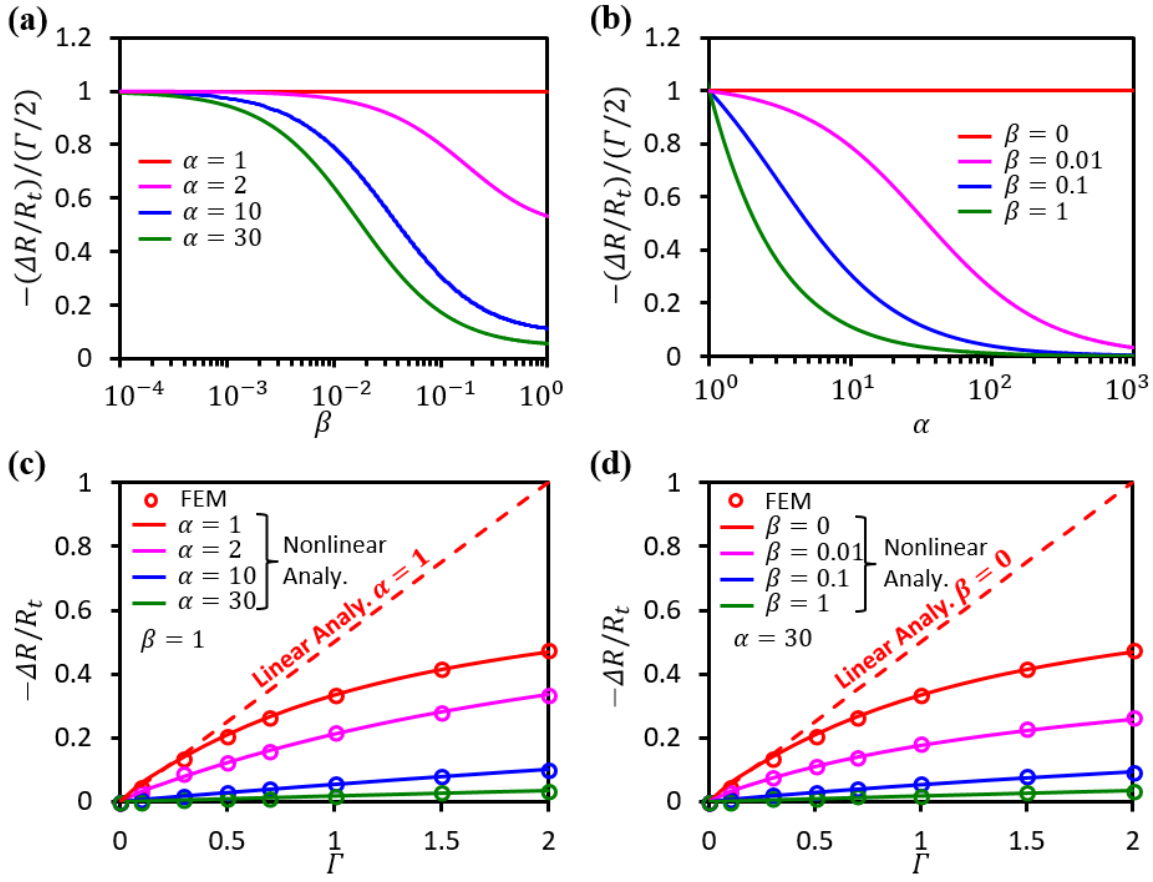

Figure 7.4 Change of crater radius during Stage 0. (a)-(b) Linear elasticity results for different α and β. $\alpha = 1$ or β=0 indicates unreinforced craters. Note that radius change is proportional to Γ. (c)-(d) Comparison among linear and nonlinear analytical results and FEM results for different α, β, and Γ.

7.3.2 Crater Volume at the end of Stage 1

Section 7.3.1 quantified the effect of surface tension for unreinforced and reinforced craters during Stage 0. To generate suction force, the crater must be compressed to squeeze out the air, which is represented by Stage 1. Intuitively, larger volume loss during compression is preferred because more air can be driven out. However, will the reinforcing shell, though plays an important role in protecting the crater shape, also resist the deformation during compression?

During Stage 1, compressive load ϵ is applied remotely. We first examined the effects of surface tension on unreinforced craters ($\alpha = 1$ or $\beta = 0$). FEM results of V_1/V_t as a function of ϵ are plotted for four different $\Gamma = 0, 0.5, 1, 2$ in Figure 7.5. Note that when $\epsilon = 0$, V_1 is the same as the crater volume at the end of Stage 0, i.e., $V_1|_{\epsilon=0} = V_0$. The red markers plot the results for $\Gamma = 0$. V_1 decreases as ϵ increases and it goes to zero when ϵ reaches 0.5, at which point the crater surface fully touches the flat plate and air inside the crater has been completely squeezed out. The red dashed curve is obtained from an analytical solution based on Eshelby formulism [180], which is only valid for small strains. When surface tension is taken into account, the starting values of V_1 are significantly smaller than V_t due to the volume loss at Stage 0. V_1 also decays slower than no surface tension case and almost reaches the same values at $\epsilon = 0.5$ for three different $\Gamma = 0.5, 1, 2$, i.e., $V_1/V_t|_{\epsilon=0.5} \sim 0.08$. The reason it is more difficult for V_1 to vanish under nonzero η is that surface tension penalizes large curvature near the rim of the crater.

Effects of reinforcing shell are illustrated by fixing $\Gamma = 1$ and varying α and β. The stiffness effect is presented in Figure 7.5 (b) with $\Gamma = 1, \beta = 1$ and $\alpha = 1, 2, 10, 30$. It clearly shows that $\alpha = 10$ (blue) and 30 (green) not only protect the crater shape during Stage 0, but also resist crater compression during Stage 1. Such a limited volume change during compression is not favorable for suction generation. In comparison, smaller α affords larger volume change during Stage 1. However, small α also yields small V_0, which leads to a tradeoff. The thickness effect is illustrated in Figure 7.5 (c) with $\Gamma = 1, \alpha = 30$ and $\beta = 0,\ 0.025,\ 0.05,\ 0.1,\ 0.2,\ 0.5$. Encouragingly, we find that thin shells with $\beta =\ 0.025,\ 0.05,\ 0.1$ can protect the crater shape during demolding (i.e. large V_0) without imposing too much constraints during compression (i.e. small V_1), which have a potential in generating high pressure drop according to Eq. (7.3).

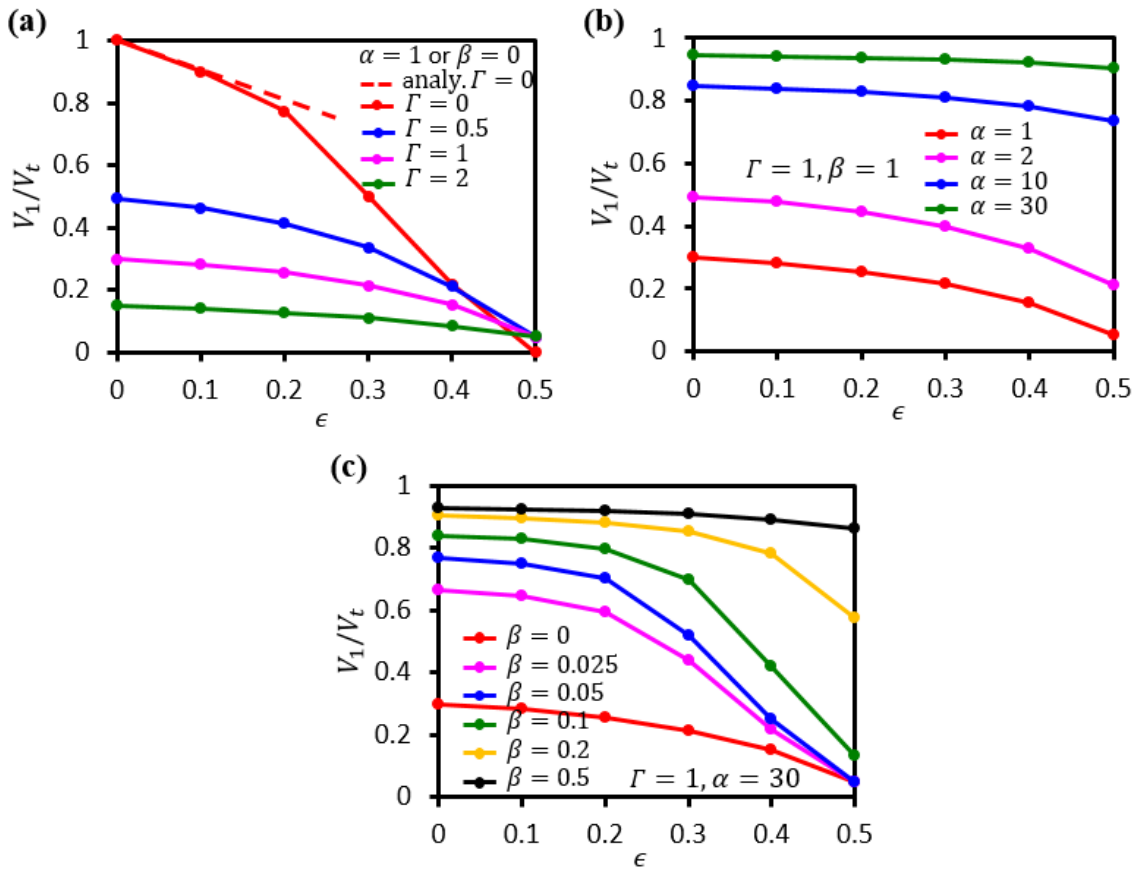

Figure 7.5 Volume of the compressed crater V_1 normalized by $V_t = 2\pi R_t^3/3$ as a function of preload ϵ: (a) Unreinforced crater with $\beta = 0, \Gamma = 0, 0.5, 1, 2$; (b) Reinforced crater with $\Gamma = 1, \beta = 1, \alpha = 1, 2, 10, 30$; (c) Reinforced crater with $\Gamma = 1, \alpha = 30, \beta = 0, 0.025, 0.05, 0.1, 0.2, 0.5$.

7.3.3 Pressure Drop and Suction Force at the end of Stage 2

When unloaded, crater springs back. At equilibrium, aside from the surface tension induced normal traction, the crater is also subjected to a negative pressure, $-\Delta p$. Therefore, ambient pressure is taken into account by introducing a new dimensionless parameter, $\delta = \mu_m/p_a$. Following the FEM procedure for Stage 2 described in Section 7.2.3, we can obtain V_2 after unloading. Plugging V_1 and V_2 in Eq. (7.3) and Eq. (7.4), we would be able to obtain the pressure drop and the suction force, respectively. We can first investigate surface tension effect for unreinforced craters. Results are plotted in Figure 7.6 with $\delta = 1, \alpha = 1$ and $\Gamma = 0, 0.5, 1, 2$. All scenarios show that pressure drop monotonically increases with ϵ. When $\Gamma = 0$, vacuum is achieved at Stage 2 when $\epsilon = 0.5$, hence $-\Delta p/p_a = 1$. When η increases, the pressure drop reduces, which clearly states that surface tension has a negative effect on pressure drop. The reason is two folds. Equation (7.3) suggests that large pressure drop comes from large V_2 and small V_1. According to our three-stage analysis, we know that large V_2 relies on large V_0. Surface tension shrinks V_0 hence limits V_2. The second effect is on V_1. As mentioned in Figure 7.5 (a) , surface tension resists compression, hence preventing the specimen from achieving small V_1.

By fixing $\Gamma = 1$, we can examine the effect of the stiffness of the polymer matrix on suction generation. The pressure drop for three different $\delta = 0.5, 1, 10$, i.e., μ_m ~50 kPa, 100 kPa, 1 MPa which are close to the moduli of commonly used PDMS, are plotted in Figure 7.6(b). The difference between the three specimens is very small because a

narrow range of δ is studied here. Thereafter, we can study the effect of reinforcing shell by simply fixing $\delta = 1$. Figure 7.6 (c) and (d) plot the pressure drop and the suction force for $\Gamma = 1, \delta = 1, \alpha = 30$ and $\beta = 0,\ 0.025,\ 0.05,\ 0.1,\ 0.2,\ 0.5$. The suction force F is normalized by $F_t = P_0 A_t$, where $A_t = \pi R_t^2$ is the projected area of the hemi-spherical dome of the molding template. Both pressure drop and suction force show non-monotonic dependence on β at $\epsilon = 0.5$. They first increase as β increases and then drop after β goes beyond a certain value. This agrees with the prediction we made in Figure 7.5 (c) that $\beta = 0.025, 0.05, 0.1$ should yield better suction because they may sustain large V_0 after demolding and are capable of reaching small V_1 after compression. An interesting observation when comparing Figure 7.6 (c) and Figure 7.6 (d) is that large pressure drop does not necessarily lead to large suction force because A_2 also contributes to F For example, the red curve ($\beta = 0$) has large pressure drop at $\epsilon = 0.5$ in Figure 7.6 (c) but the generated suction force is low in Figure 7.6 (d). This is because the A_2 is small due to the volume loss during Stage 0.

To offer a comprehensive understanding of the effects of α and β, more FEM simulations within the parameter space $\alpha \in (0,100)$ and $\beta \in (0,0.5)$ are conducted with fixed $\Gamma = 1$ and $\delta = 1$. Contour plots of pressure drop and suction force for different combinations of α and β are shown in Figs. 6e and 6f, respectively. Both $-\Delta p$ and F show non-monotonic dependence on α and β. Both figures suggest that large α and large β, i.e., thick and stiff shells, are not preferred. This is because although they can help sustain crater shape during demolding, they also greatly resist crater compression

during compression. Small α and small β does cannot offer large F either because they are not effective in protecting the crater shape during demolding. Therefore the optimal choice of α and β for large F lies in the domain $\alpha \in (20,50)$ and $\beta \in (0.025,0.15)$ as shown in Figure 7.6 (f). To quantify the suction enhancement by the reinforcing shell, we can compare the suction force generated by an optimally reinforced specimen (e.g. $\alpha = 50, \beta = 0.05$) and an unreinforced specimen ($\alpha = 1$). According to Figure 7.6 (f), the amplification factor can be determined to be 0.80/0.31=2.58. When α is large and β is small, some results are unattainable due to surface instabilities of the crater [180].

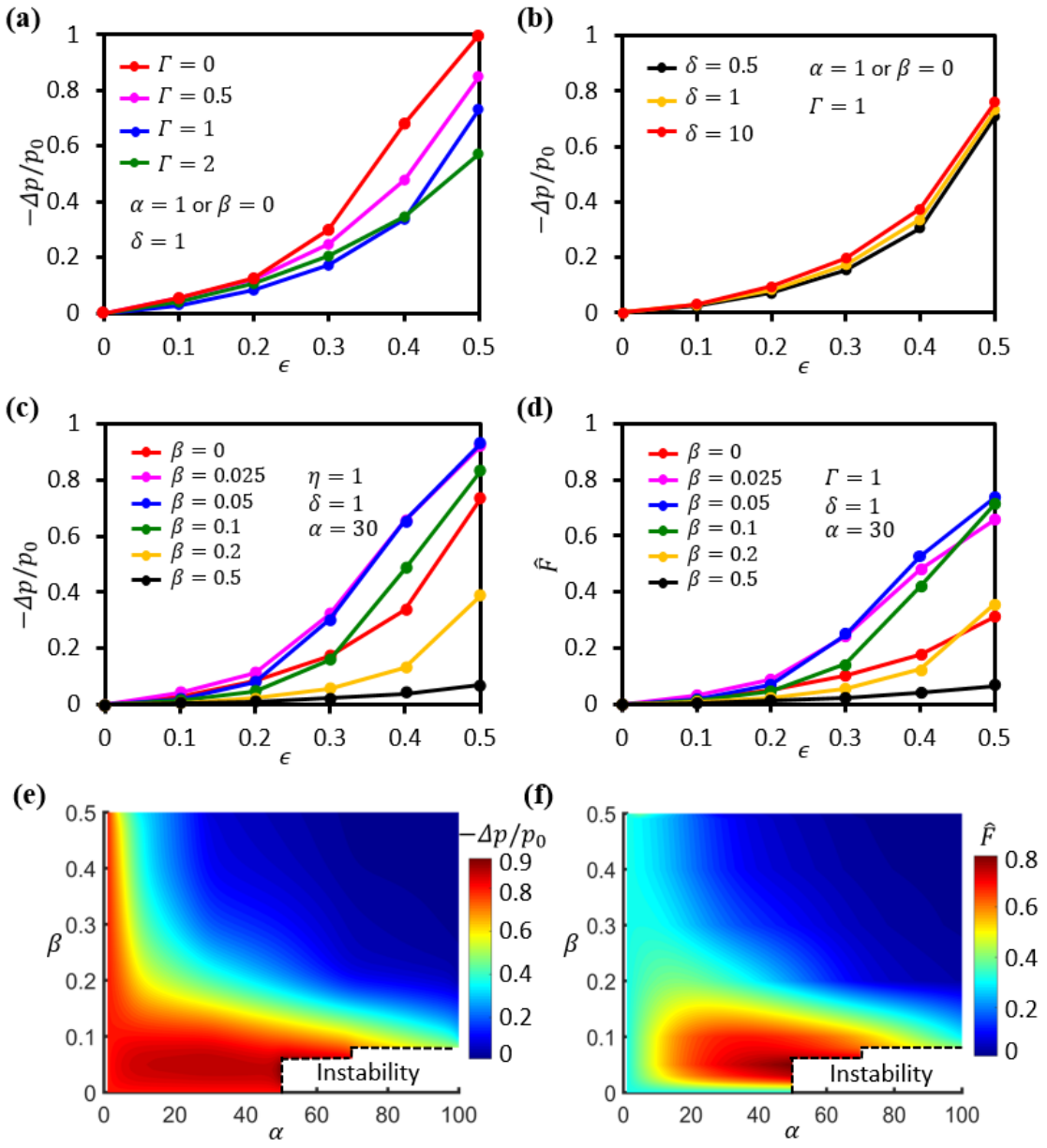

Figure 7.6 (a)-(c) Normalized pressure drop as a function of ϵ with (a) $\beta = 0, \delta = 1$, $\Gamma = 0, 0.5, 1, 2$; (b) $\eta = 1, \beta = 1, \delta = 0.5, 1, 10$; (c) $\Gamma = 1, \delta = 1, \alpha = 30, \beta = 0, 0.025, 0.05, 0.1, 0.2, 0.5$. (d) Normalized suction forces correspond to (c). (e)-(f) Contour plots of (e) normalized pressure drop and (f) normalized suction force as functions of α and β with $\Gamma = 1, \delta = 1, \epsilon = 0.5$.

7.4 CHAPTER SUMMARY

Suction forces generated by macroscopic craters depend on crater geometry, material properties, and applied preload. As craters miniaturize, surface tension can play a significant role especially when the micro- or even nano-craters are engineered on soft materials. In this chapter, we have obtained analytical solutions for the demolding process. By implementing a user-element subroutine, we have developed a three-stage FEM process to quantify the effects of surface tension on suction forces. We found that overall, surface tension is detrimental to suction forces because it shrinks crater volume after demolding and resists full closure of crater during compression. We propose that a stiff reinforcing shell can be added to prevent the crater from contraction during demolding. However, the reinforcing shell cannot be too stiff or too thick because it will then prevent crater from collapsing during compression. Extensive simulations for various combinations of shell thickness and stiffness have revealed the optimal parametric choices. We also noticed that large pressure drop does not necessarily lead to large suction force because suction force is also dependent on the projected area after unloading. This is why adding the reinforcing shell can enhance the suction force against surface tension.

Chapter 8 Isolated Craters Underwater[7]

In this chapter, we follow the framework developed in Chapter 6 to analyze isolated craters underwater. Utilizing experimental, computational, we characterize the relation between suction force and preload for liquid-filled hemi-spherical craters and spherical-cap-shaped craters. Distinct from the air-filled craters, the water inside the crater is assumed as incompressible liquid. Direct comparison between fluid and air-filled craters has been carried out. We find that the suction forces generated by underwater craters scale with specimen modulus but exhibit non-monotonic dependence on the aspect ratio of the craters.

[7] S. Qiao‡, L. Wang‡, K. Ha, N. Lu*. Suction effects of craters under water, *Soft Matter*. 14(42): 8509-8520. 2018 Oct 11; (‡ represents equal contribution. L. Wang conducted the numerical simulations and experiments, and wrote the analysis section in the paper.)

8.1 PROBLEM DESCRIPTION

Similarly with air-filled craters, we consider a specimen containing a hemi-spherical crater with radius a at its bottom (Figure 8.1). The specimen rests on the flat bottom of a rigid container. The liquid inside the crater is the same as in the ambient environment, and it is characterized by the volume V_0, N_0 molecules and the hydrostatic pressure p_0 which can be written as

$$p_0 = p_a + \gamma_w h$$

where p_a is still the atmospheric pressure, γ_w is the specific weight of the liquid, and h is the distance from the cratered surface to the liquid surface. The loading and unloading process has been established in Chapter 6 and suction force upon full unloading is defined as

$$F = -\Delta p A_2 \tag{8.1}$$

where $-\Delta p$ is the pressure drop as defined in Eq. (7.1). A complete analysis of the two-stage process requires one to model the liquid flow. We avoid this task by adopting the following assumptions:

1. The liquid flows freely out of the crater upon loading, so that $p_1 = p_0$.
2. No liquid exchange takes place upon unloading, so that $N_1 = N_2$.
3. The entire process is isothermal and the liquid is incompressible, so that $V_1 = V_2$.

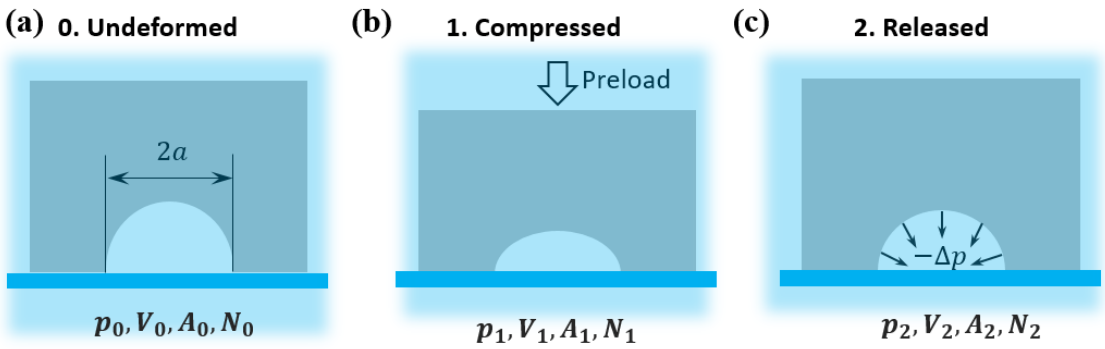

Figure 8.1 A loading-unloading cycle that produces suction force underwater: (a) A specimen with an isolated hemi-spherical crater of radius a resting on the flat bottom of a tank filled with liquid (blue); (b) The specimen is preloaded in compression and the liquid is squeezed out of the crater; (c) The preload is released, and the crater springs back, resulting in pressure drop in the crater. The symbols p, V, A and N denote the pressure, volume, projected area, and number of liquid molecules inside the crater at each state

The first assumption that the liquid can flow out freely when compressed is inspired by prior works on thin-walled suction cups [163, 167, 169]. In these models[163, 167, 169], analytical relationship between preload and suction-cup deformation has been obtained by neglecting gas or liquid resistance during compression. As for the second assumption that there is no leakage during unloading, it is consistent with experimental observations for thin-walled suction cups [163, 167, 169] as well as surface craters[69]. The third assumption of incompressible fluid is widely adopted for many liquids. With these three assumptions, the dynamics of liquid flow is regarded as a sequence of static equilibrium states. Consequently, it becomes sufficient to analyze the two-stage process in the context of solid mechanics,

One must be aware that our first assumption is only valid when there is finite amount of liquid left inside the crater at Stage 1. When the crater is fully closed, i.e. when all the liquid is squeezed out of the crater, complete vacuum is achieved inside the crater. As a result, the negative pressure is simply $-\Delta p = p_a + wh$, and will be maintained throughout the unloading process (Stage 2) if no backflow is allowed. The third assumption would break down once there is significant vaporization inside the crater, which occurs when the liquid pressure drops close to the saturated vapor pressure of this liquid. These extreme situations are elusive in the current model but we will offer in-depth discussions for them in Section 8.4

8.2 EXPERIMENTAL MEASUREMENTS

The experimental setup was designed so that it realized the two-stage process under conditions that well represent the adopted assumptions. First, polydimethylsiloxane (PDMS, Sylgard 184 Dow Corning) with the base-to-curing-agent mass ratio equal to 30:1 was cured at 70℃ for 12 hours to mold a cylindrical specimen with diameter 25.40 mm and height 35.13 mm. A hemi-spherical crater of diameter 12.70 mm was placed at the center of a circular face. The material constitutive behavior was measured to fit an incompressible neo-Hookean model with shear modulus $\mu = 47.3$ kPa in Chapter 6. Note that a hydrostatic pressure will not induce any deformation in an incompressible polymer[187]. During the entire loading-unloading process, as long as there is still incompressible fluid inside the crater, the whole specimen would be subjected to a hydrostatic pressure $p_0 = p_a + wh$. On top of that, a negative pressure is applied inside the crater during the unloading stage. Superimposing an imaginary hydrostatic tensile stress $\sigma = wh$ to the whole specimen changes its hydrostatic stress state to $p_0 - \sigma = p_a$, yet introducing no deformation due to its incompressibility. In other words, the specimens' response is independent of the liquid depth h, yielding a depth-independent suction effect. However, this argument breaks down when the incompressibility of the filling liquid no longer holds. For example, when the liquid is fully squeezed out at the end of Stage 1 or when the liquid starts to vaporize. Both situations will be discussed in detail in Section 2.4. Neglecting the two extreme cases at this point, we can simply fill the crater with incompressible fluid and perform the experiments in air at the sea level, i.e., $h = 0$ and $p_0 = p_a$ in our experiment.

To realize experimental conditions that well represent the adopted assumptions, we built a special platform as illustrated by the schematic in Figure 8.2 (a). The corresponding photograph is offered in Figure 8.2 (b). The cratered specimen was compressed against a stiff acrylic platform. At the center of the platform, we drilled a ventilation hole with a diameter of 0.8 mm, which was used for releasing and trapping liquid in the crater. During Stage 1 (loading), consistent with the first assumption, the vent hole was kept open. During Stage 2 (unloading), consistent with the second assumption, the hole was sealed. Without the vent hole, we noticed that there was resistance against liquid flowing out. Therefore, future studies should be carried out accounting for such resistance.

Direct measurements of the suction force upon unloading are difficult. Therefore we performed the loading-unloading-pulling-off experiments on the specimens and measured the pull-off force rather than the suction force. These data will be used to extract the suction force. We conducted a series of uniaxial compression and retraction tests using a Dynamic Mechanical Analyzer (DMA) (RSA-G2, TA Instruments) and a Mechanical Testing System (MTS Servohydraulic load frame with Instron 8500R controller). The load cell of the DMA has good resolution (10 μN) but limited range (up to 35 N), whereas the load cell in the MTS (Omega LCHD-50) has sufficient range (222 N) but lower resolution (0.22 N). Thus, experiments with loading forces greater than 35 N were performed with the MTS, while the rest were done using the DMA. In both testing systems, the top and bottom surfaces of the specimen were lubricated by performance oil (Fellowes Powershred Performance Shredder Oil) such that the specimen was free of friction and loaded under

uniaxial stress. The loading velocity was set at 3 mm/min, which corresponds to a nominal strain rate of 1.42×10^{-3} s^{-1}, so that the deformation was dominated by rubber elasticity.

To measure the pull-off force, Stage 2 involved not only unloading but also retraction. That is, during Stage 1, the specimen was stretched beyond the unloading point, until the cratered surface was pulled off from the platform. This pull-off force is denoted as F'. To extract the suction force, we performed the same loading-unloading experiments with the vent hole open throughout the test and the collected pull-off force is denoted as F''. Representative load-displacement curves for both cases are plotted in Figs. 2c and 2d where we identify the loading, unloading, and retraction stages, as well as the pull-off forces. Note that the two sets of data are qualitatively similar. Nevertheless, quantitative differences are significant enough to reveal the suction effect. For comparison purpose, the pull-off force F' was also measured when the crater was filled with air.

The experimentally collected pull-off force F' can be thought as a resultant force of the adhesion strength over the specimen/platform interface and the suction force over the crater, whereas F'' only consists of the interface adhesion. Thus, the difference in value

$$F = F' - F'' \tag{8.2}$$

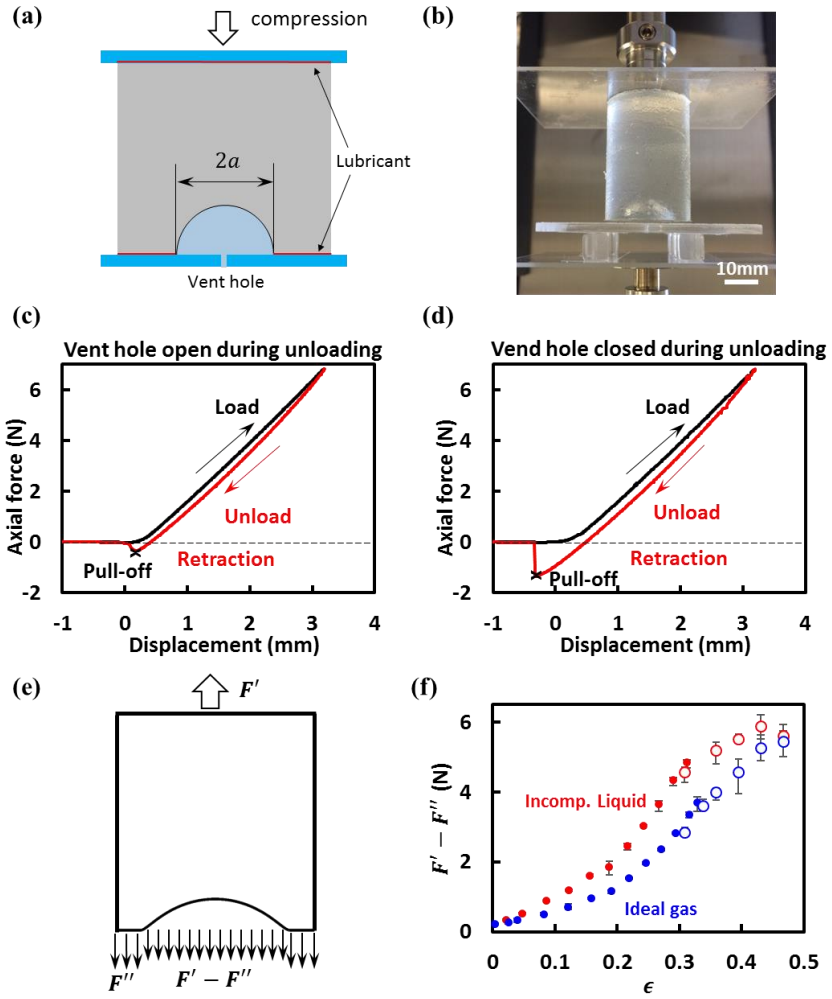

Figure 8.2 A schematic (a) and a photograph (b) of the experimental setup. The small ventilation hole drilled in the bottom platform is open during loading and closed during unloading. Load-displacement curves with vent hole open (c) and closed (d) during unloading. Peak compressive strain was 10%. Loading, unloading, retraction stages, and the pull-off points are identified. (e) A schematic of the free body diagram of a specimen at pull-off. (f) Comparisons of experimentally measured suction forces ($F' - F''$) of air-filled (blue markers) and liquid-filled (red markers) craters. Data obtained by DMA are represented by solid dots and MTS by hollow circles.

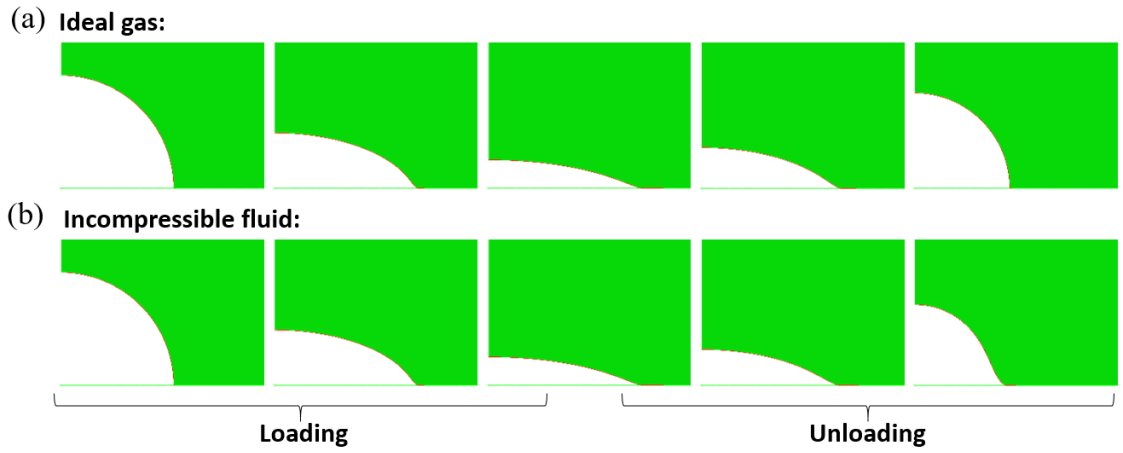

Figure 8.3 (a) A finite element mesh for an axisymmetric crater model. (b) Two deformation sequences of specimens in a loading-unloading test with different fillings: top row for air-filled crater and bottom row for liquid-filled crater.

8.3 FINITE ELEMENT ANALYSIS

Following the framework developed in Chapter 6, we can model the specimen to be incompressible neo-Hookean material with shear modulus $\mu =$ 47.3 kPa. Further, to simplify the analysis, we applied axisymmetry and the specimen/substrate interface was assumed to be frictionless (Figure 8.3 (a)). Also we neglected any surface tension effects simply because

$$\frac{\gamma}{a\mu} \approx \frac{2 \times 10^{-2}\, N/m}{(10^{-2}\ \ m) \times (4 \times 10^{4}\, N/m^{2})} = 5 \times 10^{-5} \ll 1$$

where γ is the surface tension of PDMS[171]. We have considered the effects of surface tension only when the crater size is sufficiently small [188]. If we assume the liquid inside the crater is incompressible and there is no liquid exchange during Stage 2, it means that there should be no volume change during Stage 2. As a result, the negative pressure generated at the end of Stage 2 should be fully controlled by the crater volume at the end of Stage 1, which is determined by the preload.

We used nonlinear finite element simulations to compute the relationship between the suction force and the preload ϵ. All simulations were conducted using ABAQUS Version 6.14. We built an axisymmetric model with frictionless contact at the bottom and uniform compressive displacement on the top. The finite element model with mesh formed by CAX4H elements is displayed in Figure 8.3 (a). This mesh was selected using basic convergence tests. We used the option *FLUID CAVITY which is ideal for modeling both stages of the liquid-solid interactions.

In simulations, during unloading, liquid-filled craters recover differently from air-filled craters. The deformation snapshots of liquid- and air-filled craters are displayed in Figure 8.3 (b). The first and last panels in each sequence are the initial (before loading) and final (end of unloading) configurations, respectively. The third panels correspond to the end of loading (Stage 1) with $\epsilon = 0.35$, and the rest are intermediate states. A Supplementary Movie is provided which allows one to visualize the deformation process. At the end of the unloading (Stage 2), the finite element results indicate that the air-filled crater maintains the spherical symmetry, whereas the liquid-filled crater doesn't.

8.4 RESULTS

8.4.1 Hemi-spherical crater

In this section, we first examine the difference between air-filled craters and liquid-filled craters, and explicitly discuss the effect of the depth of water. We will then compare the experimental and simulation results for both cases. In addition, we present linear analysis results of this problem based on Eshelby's formalism [172].

Still considering hemi-spherical craters with $\mu =$ 47.3 kPa, finite element simulation results for different parameters at the end of unloading as functions of ϵ are plotted in Figure 8.4: (a) normalized pressure drop $-\Delta p/p_a$, which is positive as Δp is the negative pressure, (b) phase diagram of pressure drop as a function of liquid depth h and preload ϵ, (c) normalized projected area A_2/A_0, and (d) normalized suction force, defined as

$$\hat{F} = -\Delta p A_2/(p_a A_0) \tag{8.3}$$

Full closure of the hemi-spherical craters happens at $\epsilon_f = 0.47$, which is independent of the type of the filling and denoted by vertical magenta dashed lines in all plots. After full closure, complete vacuum, i.e., $p_2 = 0$ is achieved for craters of both fillings such that further compression will no longer increase suction. Therefore, the maximum preload was chosen as $\epsilon = 0.5$ in all finite element simulations.

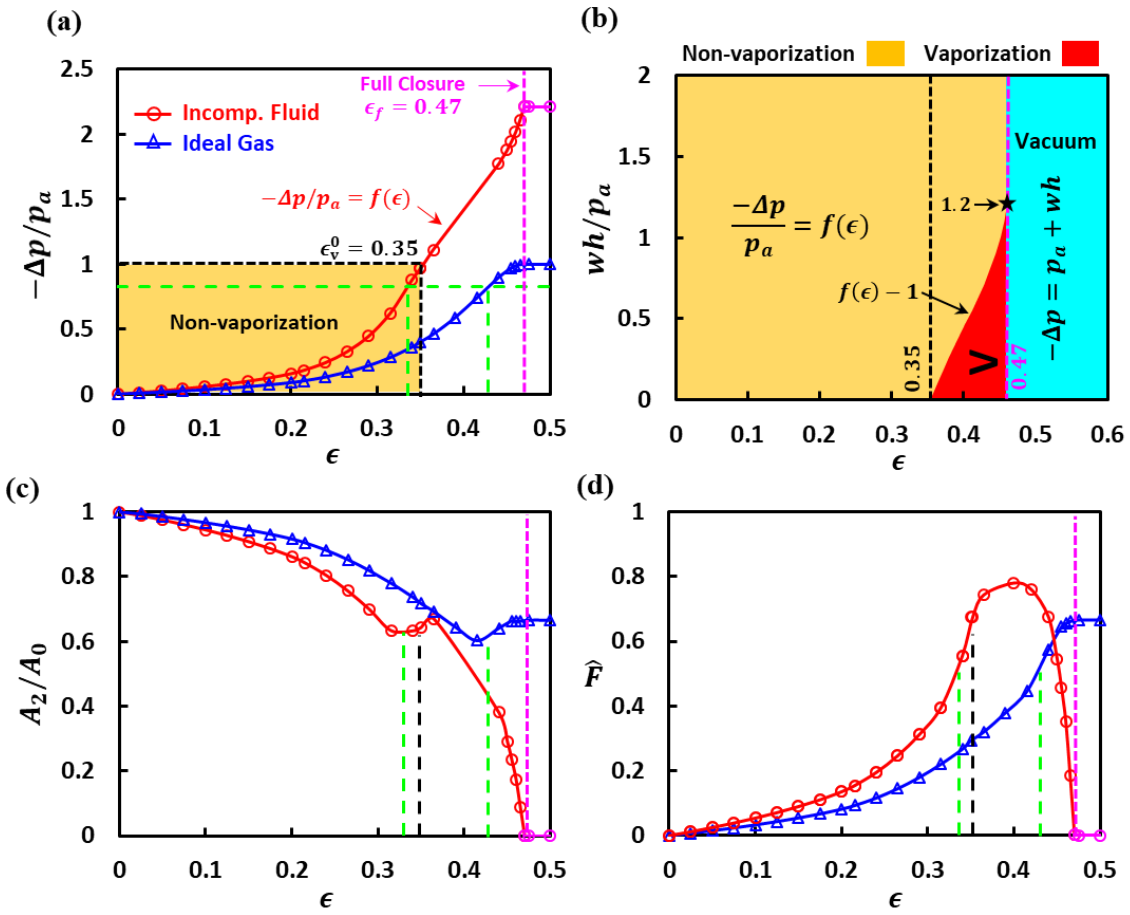

Figure 8.4 End results of the loading-unloading test are computed and plotted as functions of the preload ϵ: (a) normalized pressure drop $-\Delta p/p_a$, (b) phase diagram of pressure drop as a function of liquid depth h and preload ϵ, (c) normalized projected area A_2/A_0, and (d) normalized suction force $\hat{F} = -\Delta p A_2/(p_0 A_0)$. Craters filled with incompressible fluid are represented by circular makers and ideal gas by triangular markers.

Figure 8.4 (a) clearly shows craters of both fillings experience an increase in pressure drop with growing preload ϵ, whereas the liquid-filled craters exhibit faster increase due to the stronger constraint on the polymer matrix under volume conservation, i.e., $V_1 = V_2$, compared with ideal gas relation $p_1V_1 = p_2V_2$. It can be safely predicted that both craters should achieve vacuum when fully closed, i.e., $p_2 = 0$, such that the pressure drop for air-filled crater and liquid-filled crater should be $-\Delta p = p_a$ and $-\Delta p = p_a + wh$, respectively. As shown by the blue curve in Figure 8.4 (a), air-filled craters indeed reach $-\Delta p = p_a$ at full closure, which is consistent with our prediction. However, liquid-filled craters show a plateau of pressure drop of $-\Delta p = 2.2\ p_a$ at full closure, which is contradictory to the fact that pressure drop is dependent on liquid depth at full closure, i.e., $-\Delta p = p_a + wh$. This discrepancy results from the assumption of incompressible fluid behavior which enforces zero crater volume, i.e., $V_2 = 0$, throughout the unloading process in finite element simulation. Such a rigid constraint of volume conservation $V_2 = V_1 = 0$ at full closure contradicts with reality, thus the finite element results of $\epsilon > \epsilon_f$ in Figure 8.4 (a) (as shown by magenta makers) for liquid-filled craters are not meaningful. In reality, when the pressure inside the crater approaches the saturated vapor pressure of the liquid (denoted by p_v), the liquid vaporizes rapidly (e.g., boiling), violating the assumption of incompressibility. In this case, vaporization models should be incorporated to accurately predict the negative pressure, which is out of the scope of this paper. The saturated vapor pressure of water and oil at room temperature is very small compared with atmospheric pressure, e.g., $p_\mathrm{v} \approx 2$ kPa for water and $p_\mathrm{v} \approx 0.1$ kPa for the performance oil (99 wt% canola oil) used in our experiment according to the product sheet. Herein, we

simply assume that the liquid vaporizes when the pressure inside the crater drops to zero, i.e., when $p_2 = 0$ and $-\Delta p = p_a + wh$. The vaporization consideration actually sets an upper bound for the validity of the finite element results shown in Figure 8.4 (a). For example, consider a hemisphere-cratered specimen filled with liquid at sea level, i.e., $h = 0$, and the vaporization occurs when $-\Delta p = p_a$. A horizontal line of $-\Delta p = p_a$ (black dashed line) intersects with the curve of $-\Delta p/p_a(\epsilon)$, showing a critical preload $\epsilon_{\mathrm{v}}^0 = 0.35$. When the preload is smaller than ϵ_{v}^0, we simply assume that no vaporization will happen as the pressure inside the crater is still positive, i.e., $p_2 > 0$. Therefore, finite element results below ϵ_{v}^0 are valid while those above ϵ_{v}^0 are not. The critical preload for vaporization ϵ_{v} depends on the liquid depth h in that the pressure drop simply equals to the ambient pressure when vaporization occurs, i.e., $-\Delta p = p_a + wh$. If we simply fit the finite elements results of liquid-filled craters in Figure 8.4 (a) by using $-\Delta p/p_a = f(\epsilon)$ for $0 \le \epsilon \le \epsilon_f$ (red curve), ϵ_{v} can be obtained by solving the equation $f(\epsilon_{\mathrm{v}}) = 1 + wh/p_a$ for a given liquid depth h. When $\epsilon < \epsilon_{\mathrm{v}}$, i.e. when $f(\epsilon) < f(\epsilon_{\mathrm{v}}) = 1 + wh/p_a$, no vaporization would occur. As a result, we can write the pressure drop as a function of liquid depth h and preload ϵ:

$$-\frac{\Delta p}{p_a}\ (\epsilon, h) = \begin{cases} f(\epsilon) & 0 \le \epsilon < \epsilon_{\mathrm{v}}^0, \forall\ h \\ f(\epsilon) & \epsilon_{\mathrm{v}}^0 \le \epsilon < \epsilon_f\ \ \&\ \ wh/p_a > f(\epsilon) - 1 \\ \text{Vaporization, no solution} & \epsilon_{\mathrm{v}}^0 \le \epsilon < \epsilon_f\ \ \&\ \ wh/p_a \le f(\epsilon) - 1 \\ 1 + wh/p_a & \epsilon \ge \epsilon_f \end{cases} \tag{8.4}$$

Equation (8.4) can be illustrated by a phase diagram as Figure 8.4(b) where the horizontal axis is the preload ϵ and the vertical axis is the normalized liquid depth wh/p_a. The solution to pressure drop will be different in different regimes. The brown regimes are non-vaporizations zones where the pressure drop is simply characterized by $-\Delta p/p_a = f(\epsilon)$, the red regime is where vaporization would occur, and the cyan regime represents complete vacuum. When $\epsilon < \epsilon_{\mathrm{v}}^0 = 0.35$, the pressure inside the crater after unloading is always above zero, i.e., non-vaporization, and the pressure drop is given by $-\Delta p/p_a = f(\epsilon)$ which is independent of liquid depth h as the hydrostatic pressure wh does not deform the incompressible specimen. When $\epsilon_{\mathrm{v}}^0 \le \epsilon < \epsilon_f = 0.47$, vaporization occurs when $-\Delta p \ge p_a + wh$, i.e., $wh/p_a \le -\Delta p/p_a - 1 = f(\epsilon) - 1$, as highlighted by the red regime. Hence, when $wh/p_a > f(\epsilon) - 1$, no vaporization happens and our finite element results are useful. Interestingly, according to the finite element results in Figure 8.4 (a), when the preload approaches ϵ_f, the pressure drop is capped at $-\Delta p/p_a = 2.2$, corresponding to a maximum normalized liquid depth for vaporization $wh/p_a = 1.2$. It means that for normalized liquid depth higher than 1.2, the craters will be fully closed prior to the significant vaporization of the liquid. Such a critical liquid depth is about 12 m for water if we simply take $w \approx 10^4$ N/m^3. When $\epsilon \ge \epsilon_f$, the hemispherical crater attains full closure and realizes complete vacuum, giving rise to $-\Delta p = p_a + wh$, regardless of the flawed finite element simulation at full closure. Therefore, when the crater is fully closed, craters in deeper waters will produce higher suction force. We need to point out again that the vaporization discussed in this paper refers to the rapid liquid-to-vapor phase

transition, e.g., boiling, rather than the slow evaporation that is always ongoing on the liquid surface.

After fully understanding the pressure drop, we are ready to look at the suction force $\tilde{F}$ given in Eq. (8.3). The projected area A_2 is affected by the instabilities in the craters subjected to large preload. In Figure 8.4 (a), the horizontal dashed green line represents the critical Δp_c, beyond which the hemispherical shape of the crater breaks down upon unloading, irrespective of the filling or the depth of liquid. This critical load $-\Delta p_c = 0.83 p_a$ is obtained by analyzing the surface instability of a spherical void in an infinitely large block (See Appendix). And the corresponding critical preload ϵ_c is 0.33 and 0.43 for liquid- and air-filled craters, respectively.

As observed in finite element simulation results in Figure 8.3(b), once instability happens upon unloading, the partially recovered crater shows shallower but wider profile, giving rise to increased projected area, i.e. larger A_2. This explains the slight increase of the A_2/A_0 at ϵ_c for both liquid-filled and air-filled craters plotted in Figure 8.4(c). However, for liquid-filled craters, the instability induced increase in A_2 doesn't last. This is because the volume conservation constraint also gets stronger with increasing preload ϵ and eventually overwhelms other factors, leading to the re-decrease of A_2, as shown in Figure 8.4(c). For liquid-filled craters, A_2 eventually drops to 0 with fully closed craters due to the volume conservation enforced in the finite element simulation. The increasing Δp and the overall decreasing A_2 together produce an $\hat{F}$ that varies non-monotonically with ϵ for liquid-filled craters, as plotted in Figure 8.4. But as we discussed before, for liquid-filled craters at sea level, vaporization begins at $\epsilon_{\mathrm{v}}^0 = 0.35$, which is represented by

the black dashed lines in Figure 8.4 (c)-(d). Therefore, the finite element results for A_2 and $\hat{F}$ of liquid filled craters (the red curves) are no longer meaningful beyond the black dashed lines. However, the blue curves for air-filled craters should be valid all the way till full closure, i.e. $\epsilon_f = 0.47$.

Comparison of simulation (solid curves) and experimental (circular markers) results for hemi-spherical craters is conducted in (a), where the suction force is plotted versus the preload ϵ. Results corresponding to liquid-filled craters are plotted in red, and air-filled craters are in blue for comparison. In the range of $0 \leq \epsilon \leq 0.3$, experimental and simulation results are in good agreement for both types of craters. This validates the theoretical framework we developed and also justifies applying the framework on craters of other shapes under moderate preload. We also calculated the suction force using linear (infinitesimal strain) analysis based on Eshelby's formalism[172]. This approach is possible because of the assumptions that the specimen is large compared with the crater, the interface is frictionless, and the surface tension effects are negligible. It is clear that the linear analysis is valid for small strains, and deviates significantly from the experimental and simulation results for $\epsilon > 0.1$, and therefore its usefulness is rather limited.

Under large preload, especially when the crater reaches full closure, finite element simulation shows considerable discrepancy from experimental results for both air-filled craters and liquid-filled craters. For air-filled craters, we recognize that the source of the discrepancy comes from the different definitions of suction force used in experiments and simulations. In experiments, $F' - F''$ (Eq. (8.2)) represents the suction force inside the crater at pull-off, while in simulations, $-\Delta p A_2$ (Eq. (8.1)) is used to calculate suction

force at the end of unloading, without any retraction. At small to moderate preload, it is fair to argue that the crater has similar a configuration at pull-off and full unloading, so that

$$F' - F'' \approx -\Delta p A_2 \tag{8.5}$$

is expected. This is true under loading range $0 \leq \epsilon \leq 0.3$ based on the observation from Figure 8.5 (a). However, this approximation will no longer hold when the crater shapes are very different at pull-off and full unloading. To verify this hypothesis, we applied experimentally measured retraction strain at pull-off, ϵ_t in simulation beyond full unloading. Resulted suction forces, $F = -\Delta p' A_2'$, are plotted as solid blue diamonds in (a), where $\Delta p'$ and A_2' represent the finite element results of pressure drop inside the crater and the projected area of the crater at pull-off, respectively, at the pull-off point. Figure 8.5 (b) depicts the profiles of air-filled craters at unloading (blue curve) and pull-off (red curve) and visible difference can be found at full closure. In Figure 8.5 (a), the good agreement between $F = -\Delta p' A_2'$ (the diamond markers) and $F' - F''$ (the circular markers) indicates that, for air-filled craters, the discrepancy between the finite element results of suction force (the solid curve) and the experimentally measured pull-off force (the circular markers) can be fully explained by the difference in unloading vs. pull-off points. In other words, for air-filled craters, our finite element simulation is valid all the way up to the preload that fully closes the crater in terms of predicting the suction force at full unloading before retraction.

For liquid-filled craters, finite element results start to deviate from experiments when the preload $\epsilon > 0.3$. In addition to the difference between suction and pull-off forces

discussed above, there are other reasons which are only pertinent to liquid fillings. As we already know, the liquid inside the crater may undergo liquid-to-vapor phase transition when preload approaches the critical value $\epsilon_{\mathrm{v}}^{0} = 0.35$ as experiments are carried at sea level in air, i.e., $h = 0$. Vaporization would enlarge pressure inside the crater, thus compromising the suction force and hence the measured pull-off force. Moreover, the critical preload for vaporization $\epsilon_{\mathrm{v}}^{0} = 0.35$ was obtained without considering retraction strain ϵ_t in the simulation while the experimental results were measured at the pull-off points. Applying retraction strain to the specimen beyond full unloading will further reduce the liquid pressure inside the crater, causing the liquid to vaporize prior to the critical preload $\epsilon_{\mathrm{v}}^{0} = 0.35$. This can explain why deviation between finite element results and experiments starts after $\epsilon = 0.3$ rather than 0.35. Thus, for liquid-filled craters, the applicability of finite element simulation under large preload is limited to moderate preload. For the specimens used in this paper, the deviation between finite element simulation and experiments occurs at $\epsilon \approx 0.3$. One should note that the deviation may occur at different preload ϵ if the specimens are made of different materials or the crater shape is different or the specimen is at different depth of liquid.

It is also obvious that experimentally, craters with both fillings produced similar suction forces after full closure, validating our expectation that at full closure, the pressure drop in both types of craters should equal the ambient pressure at sea level, i.e., $-\Delta p = p_a$.

To accurately predict the pull-off force, one needs the traction-separation behavior of the specimen/platform interface, and the vaporization process of the liquid, which are

out of our current focus. So, we would focus on the study of the suction force given by Eq. (8.1).

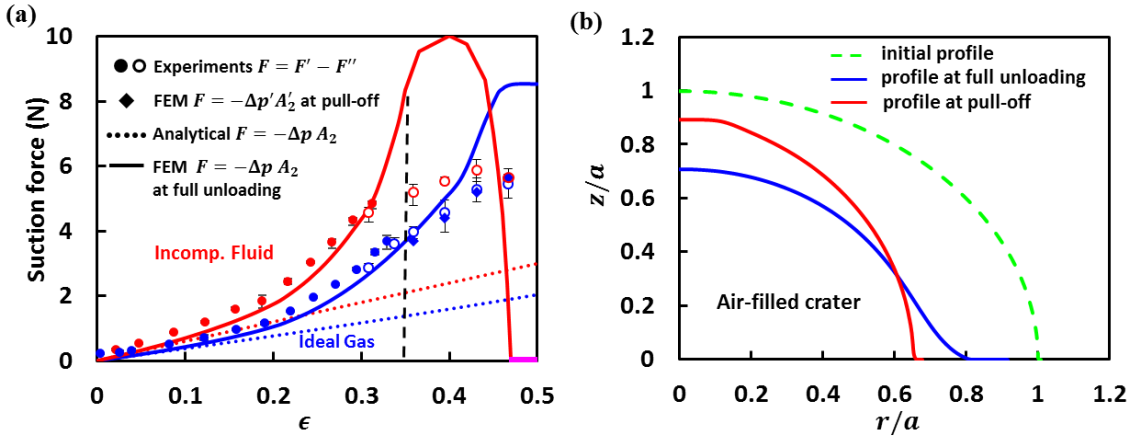

Figure 8.5 (a) Comparisons of suction forces obtained by experimental measurements (circular markers), analytical modeling (dashed curves) and finite element simulation (solid curves and diamond markers). Craters filled with incompressible fluid are represented by red ($0 \leq \epsilon < \epsilon_f$), magenta ($\epsilon_f \leq \epsilon < 0.5$) and ideal gas by blue. (b) Profiles of air-filled craters at undeformed (black dashed curve), full unloading (blue curve), and pull-off (red curve) conditions.

8.4.2 Spherical-cap-shaped craters

In this section, we extend the experimental and simulation approach established for hemi-spherical craters to spherical-cap-shaped (SCS) craters that are filled with incompressible fluid. Our objective is to investigate the effects of crater shape and preload so we fix the material modulus to be $\mu = 47.3$ kPa. In fact, according to dimensional analysis, the pressure drop and hence the suction force for underwater craters have to scale with the modulus of the specimen μ as p_a is not relevant except when considering vaporization or full closure. In this section, however, we will continue to use p_a in the normalization just to be consistent with Figure 8.4, where air-filled craters were compared with liquid-filled ones. Since our analysis is limited to large specimens, the only dimensionless geometric parameter involved is the crater aspect ratio, i.e. b/a, where a is crater base radius and b is the crater height (Figure 8.6(a)). Finite element results of pressure drops as a function of preload for SCS craters with various aspect ratios ($b/a =$ 0.1, 0.2, 0.3, 0.4, 0.5, 0.6, 0.7, 0.8, 0.9 and 1) are plotted in Figure 8.6 (b). For each b/a, the location of the preload of full closure is marked by the arrow. It is evident that shallower craters reach full closure at smaller preload than the deeper ones. Particularly, SCS craters with aspect ratio $b/a < 0.5$ reach full closure before $\epsilon_{\mathrm{v}}^{0} = 0.35$, meaning that no vaporization will take place before such craters are fully closed. For SCS craters with aspect ratios $b/a \geq 0.5$, our simulation result indicates that they have the same critical preload for vaporization, i.e. the curves all intersect at $\epsilon_{\mathrm{v}}^{0} = 0.35$ as evidenced in Figure 8.6 (b). At this moment, we do not have an explanation for this observation. To validate

our finite element simulation results for SCS craters with different aspect ratios, we conducted extra experiments on two SCS craters with aspect ratios $b/a = 0.25$ and 0.5. To eliminate the effect of A_0, the crater base radius $a = 6.35$ mm was fixed in all three specimens. All experiments were conducted in air with liquid filling at sea level under room temperature. Numerical (curves and diamond markers) and experimental (circular markers) results of suction forces for SCS craters with $b/a = 0.25,\ 0.5,$ and 1 are plotted together in Figure 8.6(c). It is obvious that the simulated suction forces only agree with measured pull-off forces at small to moderate preload. The shallower the crater, the earlier the deviation. For craters with $b/a = 0.25,\ 0.5$ and 1, the preload at deviation are $\epsilon_d = 0.05, 0.13$ and 0.3, respectively. For hemispherical crater, i.e., $b/a = 1$, towards the end of Section 2.4, this discrepancy was partially attributed to the possible vaporization when preload approaches $\epsilon_v^0 = 0.35$ (as shown by the black dashed line in Figure 8.6 (b)). However, for craters with $b/a = 0.25$ and 0.5, no vaporization would occur under such small preload, i.e., $\epsilon_d = 0.05$ and 0.13, according to Figure 8.6 (b). Therefore, we hypothesize that the deviation is due to the difference between simulated suction forces given by Eq. (8.1) and measured pull-off forces extracted using Eq. (8.2). To prove it, we added a retraction stage in finite element simulation where the applied retraction strain is the same as the pull-off strain in experiments. In this way, we can numerically obtain the suction force at the pull-off point for craters with $b/a =$ 0.25 and 0.5. Simulated results are plotted as diamond markers in Figure 8.6 (c), which agree well with the experiments. This agreement validates our hypothesis and implies that our finite element simulated suction forces (the solid curves), which are defined to be the attachment force at the end of

unloading and before retraction, are valid. But adding retraction strain for fluid-filled craters should be conducted with caution because retraction strain would further reduce the hydrostatic pressure in the liquid, expediting vaporization. For instance, for craters with $b/a = 0.5$ under preload $\epsilon = 0.29$, no vaporization happens at the end of unloading. However, after applying retraction, the pressure drop further increases beyond 1, which means although vaporization does not take place the end of unloading, it could happen at the pull-off point. Therefore, the critical preload for vaporization at pull-off, $\epsilon_{\mathrm{v}}^{\mathrm{po}}$, is smaller than that at the end of unloading, ϵ_{v}. We use blue dashed line to represent $\epsilon_{\mathrm{v}}^{\mathrm{po}}$ in Figure 8.6 (c).. Left to this line, finite element simulated suction forces at the pull-off point (blue diamonds) and experimentally measured pull-off forces (blue dots) match perfectly. Right to this line, evaporation kicks in so finite element simulation becomes useless. For craters with $b/a = 0.25$, the maximum preload used in experiment was 0.2, by which no vaporization would occur according to the finite element results at the pull-off point. Therefore, the modified finite element results (yellow diamonds) can fully capture the measured pull-off forces (yellow dots). From such exercise, we learned that as long as the crater is not fully closed and the liquid inside remains as incompressible, i.e. no vaporization, the discrepancy between the finite element curves and experimental dots purely stems from the different definitions of suction force, rather than the numerical approach itself. Therefore, it is reasonable to believe that the finite element curves before the black dashed curve $(\epsilon_{\mathrm{v}}^{0} = 0.35)$ are able to capture the true suction forces at the end of unloading.

To summarize the effects of preload and aspect ratio on suction forces, we offer a contour plot for the normalized suction force $\tilde{F}$ at full unloading (Eq. (8.3) in Figure 8.6 (d).. First, the white regime represents vacuum due to full closure. If the crater reaches vacuum, the pressure drop is simply given by $-\Delta p = p_a + wh$, which is obviously dependent on the depth of liquid, h. When $h = 0$ and the crater reaches vacuum, our previous results for air-filled craters at full closure (fig. 6b in ref [189]) are applicable. Second, before the crater is fully closed, the liquid vaporizes when the preload is beyond $\epsilon_{\mathrm{v}}^0 = 0.35$ when $h = 0$ (shown by the black dashed curve). Note that ϵ_{v} changes with h and the dependence is shown in Figure 8.4. Our simulation results beyond ϵ_{v} are not meaningful due to liquid vaporization. Third, below ϵ_{v} is the non-vaporization zone, where our numerical results have been validated by experiments as discussed in Figure 8.6 (c) and such results are independent of h. It is clear that the suction force has a non-monotonic dependence on the aspect ratio of the craters. The highest suction force $\tilde{F} = 0.69$ can be generated by a SCS crater with $b/a = 0.8$ under preload $\epsilon \approx 0.34$, as highlighted by the white star in Figure 8.6(d)

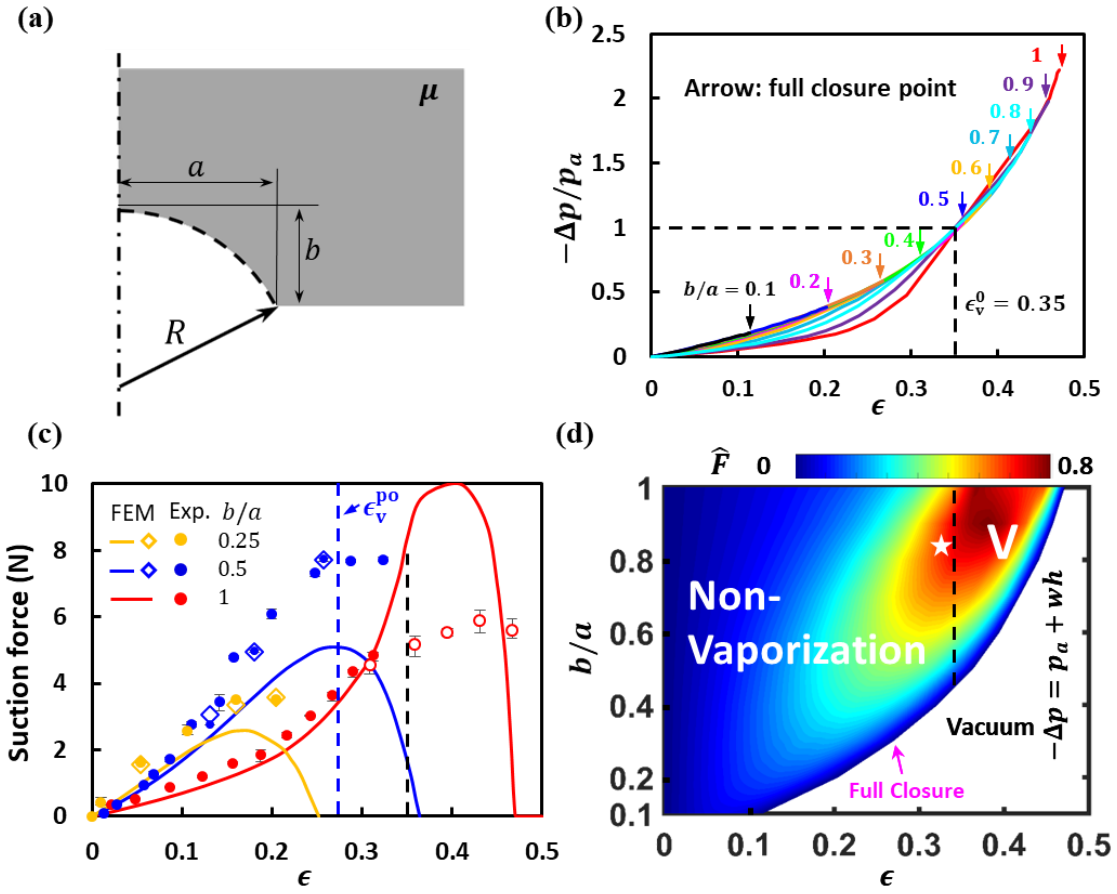

Figure 8.6 (a) Schematics of spherical-cap-shaped (SCS) crater. (b) Finite element results of pressure drop as a function of preload for various SCS craters. Arrows indicate full closure point. (c) Suction force as a function of applied strain for SCS craters with aspect ratios of $b/a = 0.25, 0.5$ and 1. Curves and diamonds represent finite element results at full unloading and pull-off point, respectively. Solid (DMA) and open (MTS) circular dots are experimental data. (d) A contour plot for the normalized suction force at full unloading $\hat{F} = -\Delta p A_2/(p_a A_0)$ as a function of b/a and ϵ. The white star highlights the highest suction force in the non-vaporization regime while the capital "V" represents the vaporization zone when $\epsilon > \epsilon_v^0 = 0.35$.

8.5 CHAPTER SUMMARY

In this paper, we try to elucidate adhesion generated by cratered surface underwater or more generally, immersed in incompressible fluid. Such enhanced adhesion is purely enabled by suction force due to pressure difference between the crater and the ambient, thus is reversible. We restricted ourselves to isolated macroscopic SCS craters, for which surface tension and other microscopic mechanisms were assumed to be negligible. The restriction to SCS craters is dictated by manufacturing considerations, but of course one can consider other shapes. Both experimental and simulation results focused on specimens resting on frictionless substrates with small vent holes. Clearly, friction would weaken the suction effect as it requires large force to close the crater. Therefore, reducing friction should be desirable for all practical purposes. Vent holes are necessary to satisfy our assumption of zero resistance to fluid flow. In reality, nonzero resistance may exist and hence would further weaken the suction effects. Under such idealized assumptions, our key findings are summarized as follows:

- As long as the specimen is immersed in incompressible fluid and the fluid inside the crater does not vaporize or fully disappear, the suction forces generated are independent of the depth of the liquid and can be confidently predicted by the framework established in this paper even under large preload.
- In this case, suction force measurement for underwater crater can be simply carried out in air with liquid filled in the crater.
- In this case, suction force produced by underwater crater scales with the modulus of the polymer material.

- In this case, for specimen of $\mu = 47.3$ kPa examined in this paper, with the same crater geometry, underwater craters are capable of producing stronger suction force than craters in air.
- In this case, for specimen of $\mu = 47.3$ kPa examined in this paper with liquid filling, the largest suction forces $\hat{F} = 0.69$ can be generated by a SCS crater with $b/a = 0.8$ under preload $\epsilon \approx 0.34$.
- If the crater is fully closed during loading, vacuum is generated in the crater and the resulting suction force should be independent of the filler but dependent on the depth of the liquid.
- The depth of the liquid and the preload together dictate when the liquid inside the crater would vaporize. When $wh/p_a > 1.2$, the liquid would never vaporize at the end of unloading even up to full closure.

Chapter 9 Crater Arrays[8]

In this chapter, we extend the study from isolated craters to crater arrays where craters can be closely packed. Adopting a SCS crater as a representative shape, we take the crater area fraction into account and consider three different crater patterns that are a single crater, square-patterned array, and hexagon-patterned array. Using finite element modeling (FEM) where the polymer matrix is modeled as 30:1 PDMS, we quantitatively present the preload-dependent suction forces of three patterns with various crater area fractions. We find for all three patterns, when the preload is small suction force increases with crater area fraction.

[8] L. Wang, K. Ha, S. Qiao, N. Lu*, Suction Effect in Crater Arrays. (*To be submitted*). (L. Wang conducted the numerical simulations, experiments and wrote the paper.)

9.1 ISOLATED CRATERS

Following experimental data for the pure prismatic specimens (see experiment in Chapter 6), we assume that the cratered specimens are also taking the incompressible neo-Hookean constitutive law with shear modulus μ =47.3 kPa. Three axisymmetric models with R/a =2, 3 and 10 are first built to examine the assumption of isolated craters. The schematic of FEM model is depicted in Figure 9.1 (a) where a hemispherical crater (i.e., $a/b = 1$) is adopted for R/a =2, 3 and 10 cases. The lubricated specimen/substrate interface was assumed to be frictionless, i.e., roller boundary condition in simulation. The preload-stretch relationships under uniaxial compression are extracted from simulation and plotted in Figure 9.1 (b), along with experimental data and fitting curve for the pure prismatic specimen. Note that the pure prismatic specimen represents the extreme condition when area fraction approaches zero, i.e., $\phi = 0$, which can be rigorously regarded as isolated craters scenario. When $R/a = 10$, corresponding to $\phi = 1\%$, finite element results shown by the square black makers almost overlap with that of $\phi = 0$. Actually, when $R/a = 3$ (i.e., $\phi = 11.1\%$ shown by the diamond blue makers), finite element result also agree very well with that from the pure prismatic specimen, suggesting that such a small crater with radius $a = R/3$ does not affect the overall behavior of the specimen under uniaxial compression test. In other words, crater arrays with $\phi \leq 11.1\%$ can be approximately treated as isolated craters where each crater does not affect its neighbors. Therefore, by fixing $R/a = 3$, simulations were carried out to account for the following four crater geometries: two SCS craters (see Figure 6.7 (a)) with $b/a = 2/3$

and 1; and other two CS craters with $b/a = 2/3$ and 1. All simulation were conducted using commercial FEM package ABAQUS 6.13 in which the built-in function *FLUID CAVITY was implemented to model the ideal gas behavior in the crater.

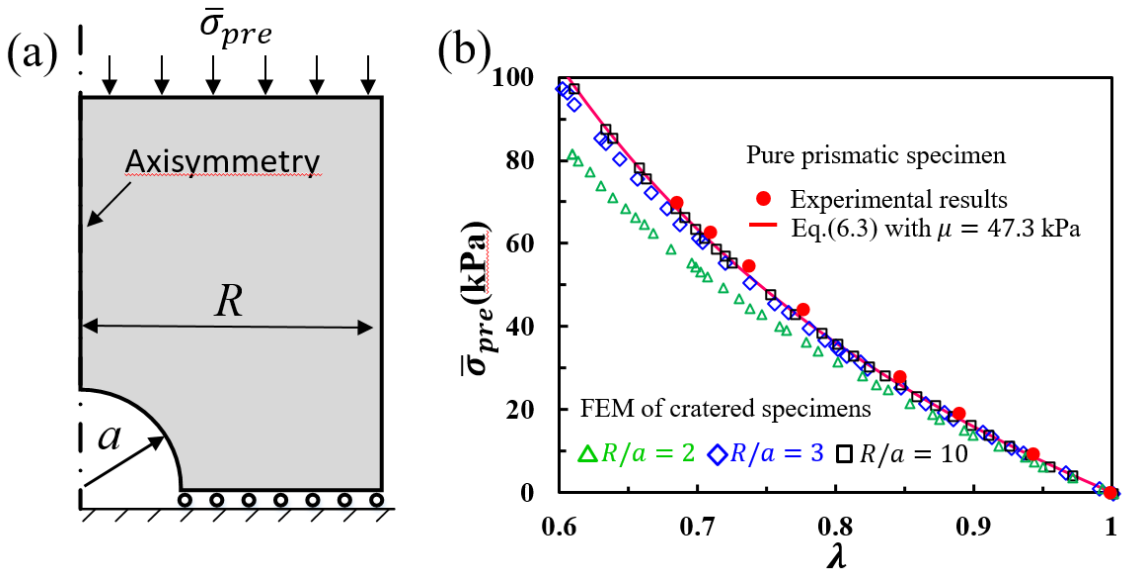

Figure 9.1 (a) Schematic of axisymmetric FEM model of isolated craters. (b) Preload-stretch relationship for pure prismatic specimen and cratered specimens. Hollow markers represent the finite element results for cratered specimen with different R/a ratios. Solid red dots are experimental data for pure prismatic specimen whose behavior can be successfully captured by a fitting curve from incompressible neo-Hookean material with shear modulus $\mu = 47.3$ kPa (shown by the red curve).

9.2 CRATER ARRAYS

In this section, we extend the simulation developed for isolated craters to crater arrays with patterns. Our focus is looking for the optimal design of the cratered surface that maximizes the suction force over a specific area, say the polymer sheet has total area A^t.

9.2.1 Simulation

Here we propose three designs. The first is the single crater and the other two are square-patterned array (SPA) and hexagon-patterned array (HPA), as illustrated in Figure 9.2. To better elucidate how crater area fraction and pattern affect the suction force, in what follows the crater geometry is fixed as a SCS crater with aspect ratio $b/a = 2/3$ and material properties is assumed to be incompressible neo-Hookean with shear modulus $\mu = 47.3$ kPa. Different from simulation for isolated craters where axisymmetric models were used, simulations for patterned craters call for three-dimensional models. Invoking the nature of its periodicity, a representative volume element of SPA and HPA, i.e., unit cell, is studied with periodic boundary conditions. The finite element simulation schemes are graphically expressed in Figure 9.2 (b) and Figure 9.2 (c), respectively. For SPA, the unit cell is a square containing a crater at the center. The side of the unit square and radius of crater are denoted as D_s and a, respectively. Geometric symmetries allow us to only consider a quarter of the unit. The *x* and *y* planes are symmetric plane as shown by dash-dotted line. The periodicity in both x and y directions dictates the square unit remains as a square under uniaxial compression. In other words, the displacement in the y direction of all nodes on $y = D_s$ plane are constrained to be the same, i.e., $u_y^{all} = u_y^r$

where superscript '*all*' represents all nodes on that plane and 'r' corresponds to the reference node which is highlighted by the red. Similarly, the displacement in the x direction of all nodes on $x = D_s$ plane is also identical, i.e., $u_x^{all} = u_x^r$. As for HPA, the unit cell is a hexagon which remains as a hexagon under uniaxial compression. Therefore, a 30°-60°-90° triangle suffices for the simulation by enforcing $u_y^{all} = u_y^r$ on $y = D_h$ plane and 60° plane remains 60°, i.e., $u_y^i = \sqrt{3}u_x^i$ where superscript 'i' denotes each individual node itself. It is worth noting that modeling a unit cell rather than the entire specimen is for the sake of simplicity. But one should be aware that such a simplification is only valid when the surface contains an infinite number of unit cells. In other words, this simplification is just an approximation for large crater arrays in which very few craters are near the surface margin where periodic boundary conditions are violated.

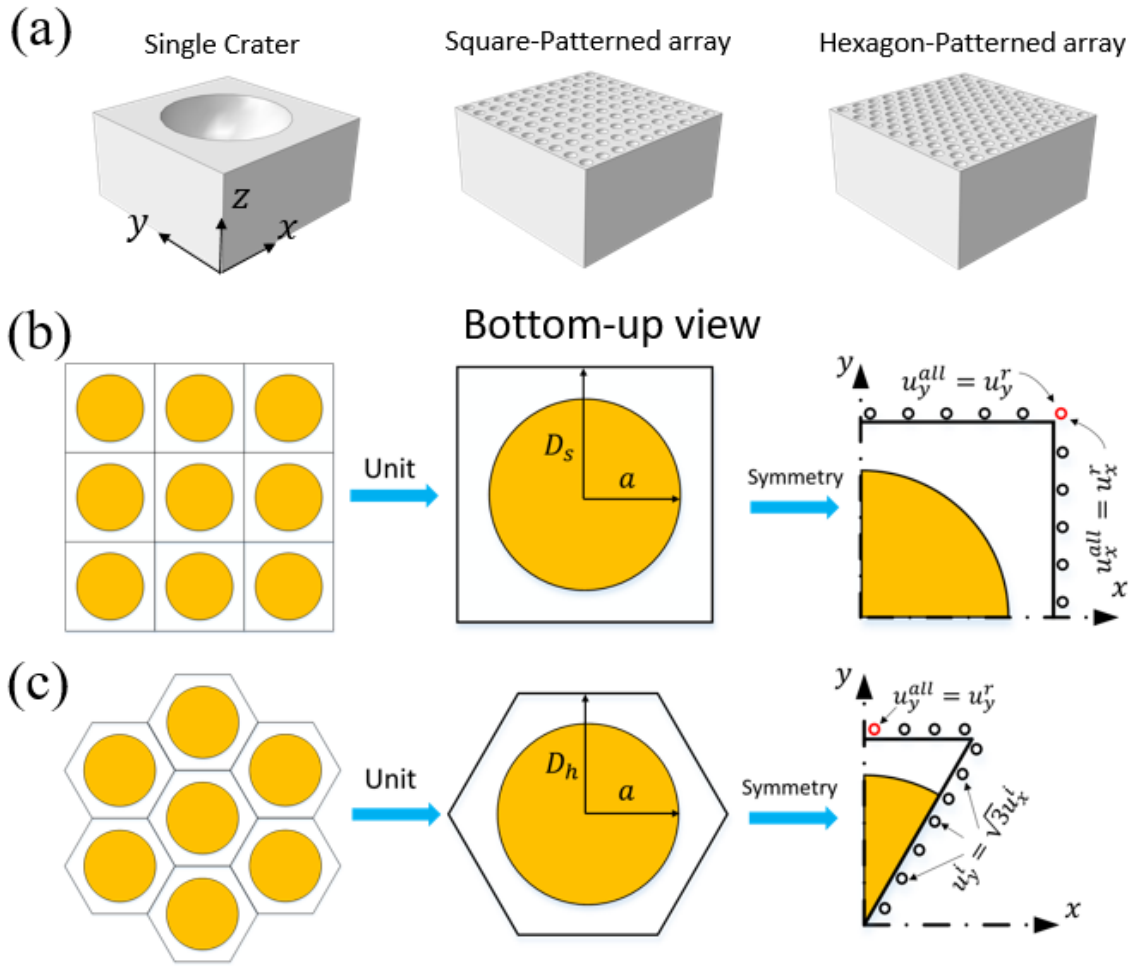

Figure 9.2 (a) Three designs for cratered surfaces: single crater, SPA, HPA. (b)-(c) Schematic of the representative volume element (RVE) used in simulation: (b) SPA; (c) HPA. Geometric periodicity and symmetry are implemented for simplification.

9.3 RESULTS

The finite element results of total suction (F^t) produced by three different cratered surfaces i.e., single crater, SPA and HPA, are given in Figure 9.3 (a)-(c). The total area the polymer surface are assumed to be the same for three designs, denoted as A^t. For single crater and SPA, the largest crater area fraction is $\pi/4 \approx 78.5\%$ thus we consider following $\phi = 8.73, 19.6, 34.9, 54.5, 64.9$ and 71.2 %, corresponding to $D_s/a = 3, 2, 1.5, 1.2, 0.1$ and 1.05; while for HPA, a higher crater area fraction $\phi = 80\%$ is also studied.

Figure 9.3 (a) clearly tells that when the crater area fraction is larger than the critical value, i.e., $\phi > \phi_c = 11.1\%$, single crater shows a non-monotonic suction-preload relation. The suction force first increase with preload and then drop as the preload further grows. When crater area fraction is high, e.g., 64.5% and 71.2%, the suction force dramatically decreases to zero when full closure is achieved. This is because, for a single crater with high ϕ, the overall structural stiffness is low due to the thin walls. As a result, there is no enough elastic energy stored in the deformed polymer matrix for the recovery of the crater and the crater sticks to the substrate at unloading, i.e., $A_2 = 0$ at State 2. The maximum suction force that a single crater can provide is around $0.17\ p_a A^t$, which occurs under $\bar{\sigma}_{pre} = 40$ kPa for $\phi = 54.5\%$ and $\bar{\sigma}_{pre} = 60$ kPa for $\phi = 34.9\%$, as shown in Figure 9.3.

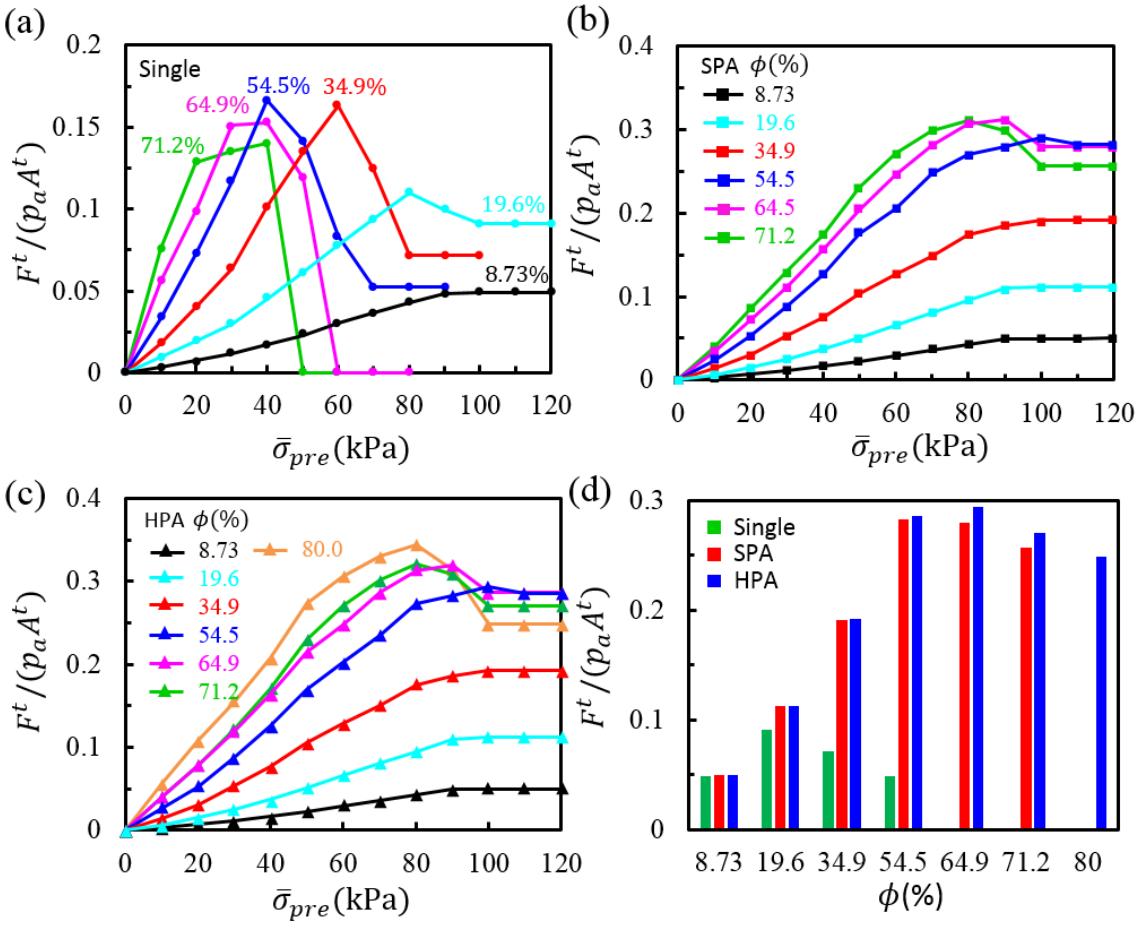

Figure 9.3 (a)-(c) Normalized total suction force as a function of preload $\bar{\sigma}_{pre}$ with (a) a single crater; (b) SPA; (c) HPA

SPA and HPA exhibit similar suction-preload relationship as plotted in Figure 9.3 (b) and Figure 9.3 (c), respectively. When the preload $\bar{\sigma}_{pre} \leq$ 80 kPa, larger crater area fraction leads to higher suction force for both SPA and HPA. The reasons are twofold. First, arrays with larger crater area fraction have lower structural stiffness, thus tend to have smaller crater volume at the end of loading under the same preload, i.e., small V_1 leads to large F according to Eq.(7.4). Second, larger crater area fraction means more craters are contributing to the total suction force. However, under larger preload, craters may attain full closure so that arrays with larger crater area fraction produce lower suction force due to the relatively small crater volume after unloading, i.e., small V_2 at Stage 2. For instance, for HPA with $\phi = 80$ %, the total suction force reaches maximum 0.34 $p_a A^t$at $\bar{\sigma}_{pre} =$ 80 kPa , i.e., suction-induced adhesive strength is 34 kPa in the air ($p_a = 101$ kPa) but drops to 0.24 $p_a A^t$ when $\bar{\sigma}_{pre} = 100$ kPa. After full closure is attained, vacuum is realized inside the crater and further preload will not enhance the suction force. For both SPA and HPA, we found the non-monotonic suction-preload relationship emerges when crater area fraction reaches 54.5%, as shown by the blue markers in Figure 9.3 (a) and Figure 9.3 (b). It is also worth noting that all three designs, i.e., a single crater, SPA and HPA, show exact the same suction performance when crater area fraction is lower than the critical value (e.g., $\phi = 8.53\%$ as shown by black markers in Figure 9.3 (a)-(c))below which all can be regarded as isolated.

The suction-based dry adhesion intrinsically depends on the preload. A fair comparison of suction forces generated by three patterns can be made under the same

preload. For example, by fixing $\bar{\sigma}_{pre} = 120$ kPa where full closure of craters are achieved for all three scenarios, suction forces as a function of crater area fractions is plotted in Figure 9.3. It clearly shows that SPA and HPA outperform a single crater, having a maximum suction force which is about three times higher than that produced by a single crater. Also, it is evident that suction forces have a non-monotonic dependency on the crater area fraction for all three cratered surfaces. At full closure, the optimal crater area fraction that yields highest suction force for SPA and HPA are 54.5% and 64.9%, respectively. One can also conclude that HPA shows a little bit higher suction force than that of SPA when they have the same crater area fraction.

9.4 CHAPTER SUMMARY

Suction forces generated by cratered surfaces depend on the crater gometry, crater area fraction, array pattern, and applied preload. In this chapter, we first established a loading-unloading framework for quantifying the suction produced by an isolated crater, i.e., craters are sparsely distributed using both numerical simulation and experimental approaches. The crater geometry including spherical-cap-shaped and cylinder-shaped craters with various height-to-radius ratios are investigated and the suction-preload relationship are quantitatively obtained. Then we extended the study from isolated craters to crater arrays where craters are can be closely packed. Two cratered arrays, i.e., square-patterned array and hexagon-patterned array, with various crater area fractions are systematically analyzed using finite element simulation. We found that the suction force has non-monotonic dependency on the crater area fraction. Overall, the hexagon-patterned array exhibits the best suction performance, having the maximum adhesive strength around 34 kPa in the air. Our results also show that full closure of the crater induced by large preload may impair the suction effect. To achieve the highest suction force, a moderately large preload is desired. This study provides an insight to the design of the cratered surfaces which may find remarkable applications such as dry adhesives for bio-tissues.

Chapter 10 Conclusions and Outlook

The last chapter summarizes this dissertation and proposes suggested directions for future research.

10.1 SUMMARY AND CONCLUDING REMARKS

In this dissertation, conformal electronics toward applications such as bio-electronics have been discussed. Two topics are covered: mechanics of conformability under vdW interaction, and crater-enabled dry adhesives.

Mechanics of Conformability

Conformability of a thin elastic membrane conforming to soft and rough substrate has been analytically quantified in Chapter 3. Three contact modes, i.e., non-conformed, partially conformed, and fully-conformed, can be readily predicted by the energy minimization method. The external compression/stretching has also been investigated in Chapter 4, where critical parameters for structural design are updated for a fully conformed scenario to take place. These two studies offer simple but effective guidelines for the optimization of conformable bio-electronics.

Crater-enabled Dry Adhesives

The adhesion mechanism of crater-enabled dry adhesives has been revealed via a framework of modeling suction effect. A variety of factors that may affect the suction force, such as the craters shape, matrix stiffness, crater area fraction, preload, surface tension, and dry/wet ambient environment, have been investigated in Chapter 6 to Chapter 9, using experiments, numerical simulation, and analytical approaches. Some key finding read as follows

- Craters are capable of producing stronger suction force under water rather than in air.
- In soft matrix, large suction forces require crater reinforcement to prevent capillarity-induced collapse of microscale craters.
- Under full closure, the maximum suction force of 30:1 PDMS SCS crater with height-to-radius ratio equals 2/3 is achieved when optimal crater area fraction is ~65%.

10.2 SUGGESTIONS FOR FUTURE WORK

Mechanics of Conformability

Current conformability analysis only focuses on a sinusoidally wavy surface, which has been markedly simplified for characterizing the morphology of soft substrate like skin. Actually, conformable electronics may encounter rough surfaces with different textures, for example, deep creases/grooves on the brain or spherical-doom retina in the eye. In addition to the widely used meshed, serpentine, and buckled patterning strategies, new structural design such as cutting may also be implemented to minimize folds or ridges of the electronics when conforming to different terrains. Theoretical analysis, experiments, and numerical simulations may be conducted in this direction.

Crater-enabled Dry Adhesives

First, the current modeling framework presumes a frictionless contact between the crater and substrate and the separation is governed by a uniform pull-off strength. Future work may take the friction into consideration and analyze the pull-off behavior with traction-separation law assigned at the interface. Second, it has been reported crater arrays with the exact same pattern, crater shape, and area fraction may exhibit different adhesion strength when the size of the crater is different. The comprehensive understanding of the size effect still remains unavailable yet which is indeed worth studying in the future.

References

[1] Paulsen, J. A., Renn, M., Christenson, K., and Plourde, R., "Printing conformal electronics on 3D structures with Aerosol Jet technology," Proc. 2012 Future of Instrumentation International Workshop (FIIW) Proceedings, IEEE, pp. 1-4.
[2] Blumenthal, T., Fratello, V., Nino, G., and Ritala, K., "Conformal printing of sensors on 3D and flexible surfaces using aerosol jet deposition," Proc. Nanosensors, Biosensors, and Info-Tech Sensors and Systems 2013, International Society for Optics and Photonics, p. 86910P.
[3] Kim, D. H., Lu, N., Ma, R., Kim, Y. S., Kim, R. H., Wang, S., Wu, J., Won, S. M., Tao, H., Islam, A., Yu, K. J., Kim, T. I., Chowdhury, R., Ying, M., Xu, L., Li, M., Chung, H. J., Keum, H., McCormick, M., Liu, P., Zhang, Y. W., Omenetto, F. G., Huang, Y., Coleman, T., and Rogers, J. A., 2011, "Epidermal electronics," Science, 333(6044), pp. 838-843.
[4] Lee, H., Choi, T. K., Lee, Y. B., Cho, H. R., Ghaffari, R., Wang, L., Choi, H. J., Chung, T. D., Lu, N., and Hyeon, T., 2016, "A graphene-based electrochemical device with thermoresponsive microneedles for diabetes monitoring and therapy," Nature nanotechnology, 11(6), pp. 566-572.
[5] Kim, S. J., Cho, K. W., Cho, H. R., Wang, L., Park, S. Y., Lee, S. E., Hyeon, T., Lu, N., Choi, S. H., and Kim, D. H., 2016, "Stretchable and transparent biointerface using cell‐sheet‐graphene hybrid for electrophysiology and therapy of skeletal muscle," Advanced Functional Materials, 26(19), pp. 3207-3217.
[6] Kabiri Ameri, S., Ho, R., Jang, H., Tao, L., Wang, Y., Wang, L., Schnyer, D. M., Akinwande, D., and Lu, N., 2017, "Graphene Electronic Tattoo Sensors," ACS nano, 11(8), pp. 7634-7641.
[7] Reeder, J., Kaltenbrunner, M., Ware, T., Arreaga‐Salas, D., Avendano‐Bolivar, A., Yokota, T., Inoue, Y., Sekino, M., Voit, W., and Sekitani, T., 2014, "Mechanically adaptive organic transistors for implantable electronics," Advanced Materials, 26(29), pp. 4967-4973.
[8] Choi, C., Choi, M. K., Liu, S., Kim, M. S., Park, O. K., Im, C., Kim, J., Qin, X., Lee, G. J., and Cho, K. W., 2017, "Human eye-inspired soft optoelectronic device using high-density MoS 2-graphene curved image sensor array," Nature communications, 8(1), p. 1664.
[9] Kim, D.-H., Viventi, J., Amsden, J. J., Xiao, J., Vigeland, L., Kim, Y.-S., Blanco, J. A., Panilaitis, B., Frechette, E. S., Contreras, D., Kaplan, D. L., Omenetto, F. G., Huang, Y., Hwang, K.-C., Zakin, M. R., Litt, B., and Rogers, J. A., 2010, "Dissolvable films of silk fibroin for ultrathin conformal bio-integrated electronics," Nature Materials, 9(6), pp. 511-517.
[10] Song, J. K., Son, D., Kim, J., Yoo, Y. J., Lee, G. J., Wang, L., Choi, M. K., Yang, J., Lee, M., and Do, K., 2017, "Wearable Force Touch Sensor Array Using a Flexible and Transparent Electrode," Advanced Functional Materials, 27(6).
[11] Lai, Y. C., Deng, J., Liu, R., Hsiao, Y. C., Zhang, S. L., Peng, W., Wu, H. M., Wang, X., and Wang, Z. L., 2018, "Actively Perceiving and Responsive Soft Robots Enabled by

Self‐Powered, Highly Extensible, and Highly Sensitive Triboelectric Proximity‐and Pressure‐Sensing Skins," Advanced Materials, 30(28), p. 1801114.
[12] Pang, C., Lee, G.-Y., Kim, T.-i., Kim, S. M., Kim, H. N., Ahn, S.-H., and Suh, K.-Y., 2012, "A flexible and highly sensitive strain-gauge sensor using reversible interlocking of nanofibres," Nature materials, 11(9), pp. 795-801.
[13] Chortos, A., Liu, J., and Bao, Z., 2016, "Pursuing prosthetic electronic skin," 15(9), p. 937.
[14] Kim, J., Lee, M., Shim, H. J., Ghaffari, R., Cho, H. R., Son, D., Jung, Y. H., Soh, M., Choi, C., and Jung, S. J. N. c., 2014, "Stretchable silicon nanoribbon electronics for skin prosthesis," 5, p. 5747.
[15] Kanao, K., Nakata, S., Arie, T., Akita, S., and Takei, K., 2017, "Human-interactive multi-functional electronic wallpaper integrated with sensors and memory," Materials Horizons, 4(6), pp. 1079-1084.
[16] Liu, X., Tang, C., Du, X., Xiong, S., Xi, S., Liu, Y., Shen, X., Zheng, Q., Wang, Z., and Wu, Y., 2017, "A highly sensitive graphene woven fabric strain sensor for wearable wireless musical instruments," Materials Horizons, 4(3), pp. 477-486.
[17] Kong, Y. L., Tamargo, I. A., Kim, H., Johnson, B. N., Gupta, M. K., Koh, T.-W., Chin, H.-A., Steingart, D. A., Rand, B. P., and McAlpine, M. C., 2014, "3D printed quantum dot light-emitting diodes," Nano letters, 14(12), pp. 7017-7023.
[18] Pan, C., Kumar, K., Li, J., Markvicka, E. J., Herman, P. R., and Majidi, C., 2018, "Visually Imperceptible Liquid‐Metal Circuits for Transparent, Stretchable Electronics with Direct Laser Writing," Advanced Materials, 30(12), p. 1706937.
[19] Zang, Y., Zhang, F., Di, C.-a., and Zhu, D., 2015, "Advances of flexible pressure sensors toward artificial intelligence and health care applications," Materials Horizons, 2(2), pp. 140-156.
[20] Xu, L., Gutbrod, S. R., Bonifas, A. P., Su, Y., Sulkin, M. S., Lu, N., Chung, H.-J., Jang, K.-I., Liu, Z., and Ying, M., 2014, "3D multifunctional integumentary membranes for spatiotemporal cardiac measurements and stimulation across the entire epicardium," Nature communications, 5, p. 3329.
[21] Dagdeviren, C., Su, Y., Joe, P., Yona, R., Liu, Y., Kim, Y.-S., Huang, Y., Damadoran, A. R., Xia, J., and Martin, L. W., 2014, "Conformable amplified lead zirconate titanate sensors with enhanced piezoelectric response for cutaneous pressure monitoring," Nature communications, 5, p. 4496.
[22] Yuk, H., Lu, B., and Zhao, X., 2019, "Hydrogel bioelectronics," Chemical Society Reviews.
[23] Yin, M. j., Zhang, Y., Yin, Z., Zheng, Q., and Zhang, A. P. J. A. M. T., 2018, "Micropatterned Elastic Gold‐Nanowire/Polyacrylamide Composite Hydrogels for Wearable Pressure Sensors," p. 1800051.
[24] Jing, X., Mi, H.-Y., Lin, Y.-J., Enriquez, E., Peng, X.-F., and Turng, L.-S., 2018, "Highly Stretchable and Biocompatible Strain Sensors Based on Mussel-Inspired Super-Adhesive Self-Healing Hydrogels for Human Motion Monitoring," ACS applied materials & interfaces.

[25] Song, Y. M., Xie, Y., Malyarchuk, V., Xiao, J., Jung, I., Choi, K.-J., Liu, Z., Park, H., Lu, C., and Kim, R.-H., 2013, "Digital cameras with designs inspired by the arthropod eye," Nature, 497(7447), p. 95.
[26] Sekitani, T., Nakajima, H., Maeda, H., Fukushima, T., Aida, T., Hata, K., and Someya, T., 2009, "Stretchable active-matrix organic light-emitting diode display using printable elastic conductors," Nature materials, 8(6), p. 494.
[27] Vosgueritchian, M., Tok, J. B.-H., and Bao, Z., 2013, "Stretchable LEDs: Light-emitting electronic skin," Nature Photonics, 7(10), p. 769.
[28] Wu, H., Huang, Y., Xu, F., Duan, Y., and Yin, Z., 2016, "Energy harvesters for wearable and stretchable electronics: from flexibility to stretchability," Advanced materials, 28(45), pp. 9881-9919.
[29] Tong, J., Xiong, S., Zhou, Y., Mao, L., Min, X., Li, Z., Jiang, F., Meng, W., Qin, F., and Liu, T., 2016, "Flexible all-solution-processed all-plastic multijunction solar cells for powering electronic devices," Materials Horizons, 3(5), pp. 452-459.
[30] Huang, Y., Wu, H., Xiao, L., Duan, Y., Zhu, H., Bian, J., Ye, D., and Yin, Z., 2019, "Assembly and Application of 3D Conformal Electronics on Curvilinear Surface," Materials Horizons.
[31] Miyamoto, A., Lee, S., Cooray, N. F., Lee, S., Mori, M., Matsuhisa, N., Jin, H., Yoda, L., Yokota, T., and Itoh, A. J. N. n., 2017, "Inflammation-free, gas-permeable, lightweight, stretchable on-skin electronics with nanomeshes," 12(9), p. 907.
[32] Kim, D.-H., Song, J., Choi, W. M., Kim, H.-S., Kim, R.-H., Liu, Z., Huang, Y. Y., Hwang, K.-C., Zhang, Y.-w., and Rogers, J. A. J. P. o. t. N. A. o. S., 2008, "Materials and noncoplanar mesh designs for integrated circuits with linear elastic responses to extreme mechanical deformations," 105(48), pp. 18675-18680.
[33] Lanzara, G., Salowitz, N., Guo, Z., and Chang, F. K. J. A. M., 2010, "A Spider‐Web‐Like Highly Expandable Sensor Network for Multifunctional Materials," 22(41), pp. 4643-4648.
[34] Yang, S., Ng, E., and Lu, N., 2015, "Indium tin oxide (ito) serpentine ribbons on soft substrates stretched beyond 100%," Extreme Mechanics Letters, 2, pp. 37-45.
[35] Hu, X., Dou, Y., Li, J., and Liu, Z., "Buckled Structures: Fabrication and Applications in Wearable Electronics," Small, 0(0), p. 1804805.
[36] Yang, S., Qiao, S., and Lu, N., 2016, "Elasticity Solutions to Nonbuckling Serpentine Ribbons," Journal of Applied Mechanics, 84(2), pp. 021004-021004-021009.
[37] Zhang, Y., Fu, H., Xu, S., Fan, J. A., Hwang, K.-C., Jiang, J., Rogers, J. A., Huang, Y. J. J. o. t. M., and Solids, P. o., 2014, "A hierarchical computational model for stretchable interconnects with fractal-inspired designs," 72, pp. 115-130.
[38] Zhang, Y., Xu, S., Fu, H., Lee, J., Su, J., Hwang, K.-C., Rogers, J. A., and Huang, Y., 2013, "Buckling in serpentine microstructures and applications in elastomer-supported ultra-stretchable electronics with high areal coverage," Soft Matter, 9(33), pp. 8062-8070.
[39] Hwang, I., Kim, H. N., Seong, M., Lee, S. H., Kang, M., Yi, H., Bae, W. G., Kwak, M. K., and Jeong, H. E., 2018, "Multifunctional Smart Skin Adhesive Patches for Advanced Health Care," Advanced healthcare materials, p. 1800275.

[40] Dong, W., Wang, Y., Zhou, Y., Bai, Y., Ju, Z., Guo, J., Gu, G., Bai, K., Ouyang, G., and Chen, S., 2018, "Soft human–machine interfaces: design, sensing and stimulation," International Journal of Intelligent Robotics and Applications, pp. 1-26.
[41] Wang, Y., Qiu, Y., Ameri, S. K., Jang, H., Dai, Z., Huang, Y., and Lu, N. J. N. F. E., 2018, "Low-cost, μm-thick, tape-free electronic tattoo sensors with minimized motion and sweat artifacts," 2(1), p. 6.
[42] Hyoyoung Jeong, L. W., Taewoo Ha, Ruchika Mitbander, Xiangxing Yang, Zhaohe Dai, Shutoa Qiao, Linxiao Shen, Nans Sun ,Nanshu Lu, 2019, "Modularized Stretchable Electronic Tattoos with Wireless Power and Near-Field Communication Capabilities," Submitted.
[43] Bae, W. G., Kim, D., Kwak, M. K., Ha, L., Kang, S. M., and Suh, K. Y., 2013, "Enhanced Skin Adhesive Patch with Modulus‐Tunable Composite Micropillars," Advanced healthcare materials, 2(1), pp. 109-113.
[44] Oh, J. H., Hong, S. Y., Park, H., Jin, S. W., Jeong, Y. R., Oh, S. Y., Yun, J., Lee, H., Kim, J. W., and Ha, J. S., 2018, "Fabrication of High-Sensitivity Skin-Attachable Temperature Sensors with Bioinspired Microstructured Adhesive," ACS applied materials & interfaces, 10(8), pp. 7263-7270.
[45] Webster, I., 1997, "Recent developments in pressure-sensitive adhesives for medical applications," International Journal of Adhesion and Adhesives, 17(1), pp. 69-73.
[46] Donkerwolcke, M., Burny, F., and Muster, D., 1998, "Tissues and bone adhesives—historical aspects," Biomaterials, 19(16), pp. 1461-1466.
[47] Creton, C., 2003, "Pressure-sensitive adhesives: an introductory course," MRS bulletin, 28(6), pp. 434-439.
[48] Czech, Z., and Kowalczyk, A., 2011, "Pressure-sensitive adhesives for medical applications," Wide Spectra of Quality Control, InTech.
[49] Amjadi, M., Sheykhansari, S., Nelson, B. J., and Sitti, M., 2018, "Recent Advances in Wearable Transdermal Delivery Systems," Advanced Materials, 30(7), p. 1704530.
[50] Jeong, J.-W., Yeo, W.-H., Akhtar, A., Norton, J. J. S., Kwack, Y.-J., Li, S., Jung, S.-Y., Su, Y., Lee, W., Xia, J., Cheng, H., Huang, Y., Choi, W.-S., Bretl, T., and Rogers, J. A., 2013, "Materials and Optimized Designs for Human-Machine Interfaces Via Epidermal Electronics," Advanced Materials, 25(47), pp. 6839-6846.
[51] Kim, D.-H., Ghaffari, R., Lu, N., Wang, S., Lee, S. P., Keum, H., D'Angelo, R., Klinker, L., Su, Y., and Lu, C., 2012, "Electronic sensor and actuator webs for large-area complex geometry cardiac mapping and therapy," Proceedings of the National Academy of Sciences, 109(49), pp. 19910-19915.
[52] Wang, C., Wang, C., Huang, Z., and Xu, S. J. A. M., 2018, "Materials and Structures toward Soft Electronics," p. 1801368.
[53] Chivers, R. A., 2001, "Easy removal of pressure sensitive adhesives for skin applications," International journal of adhesion and adhesives, 21(5), pp. 381-388.
[54] Konya, C., Sanada, H., Sugama, J., Okuwa, M., Kamatani, Y., Nakagami, G., and Sakaki, K., 2010, "Skin injuries caused by medical adhesive tape in older people and associated factors," Journal of clinical nursing, 19(9‐10), pp. 1236-1242.

[55] Matsumura, H., Ahmatjan, N., Ida, Y., Imai, R., and Wanatabe, K., 2013, "A model for quantitative evaluation of skin damage at adhesive wound dressing removal," International wound journal, 10(3), pp. 291-294.
[56] Autumn, K., Liang, Y. A., Hsieh, S. T., Zesch, W., Chan, W. P., Kenny, T. W., Fearing, R., and Full, R. J., 2000, "Adhesive force of a single gecko foot-hair," Nature, 405(6787), pp. 681-685.
[57] Geim, A. K., Dubonos, S. V., Grigorieva, I. V., Novoselov, K. S., Zhukov, A. A., and Shapoval, S. Y., 2003, "Microfabricated adhesive mimicking gecko foot-hair," Nat Mater, 2(7), pp. 461-463.
[58] Autumn, K., Dittmore, A., Santos, D., Spenko, M., and Cutkosky, M., 2006, "Frictional adhesion: a new angle on gecko attachment," Journal of Experimental Biology, 209(18), pp. 3569-3579.
[59] Mahdavi, A., Ferreira, L., Sundback, C., Nichol, J. W., Chan, E. P., Carter, D. J., Bettinger, C. J., Patanavanich, S., Chignozha, L., and Ben-Joseph, E., 2008, "A biodegradable and biocompatible gecko-inspired tissue adhesive," Proceedings of the National Academy of Sciences, 105(7), pp. 2307-2312.
[60] Tsai, C.-Y., and Chang, C.-C., 2013, "Auto-adhesive transdermal drug delivery patches using beetle inspired micropillar structures," J. Mater. Chem. B, 1(43), pp. 5963-5970.
[61] Pang, C., Koo, J. H., Nguyen, A., Caves, J. M., Kim, M. G., Chortos, A., Kim, K., Wang, P. J., Tok, J. B. H., and Bao, Z., 2015, "Highly Skin‐Conformal Microhairy Sensor for Pulse Signal Amplification," Advanced Materials, 27(4), pp. 634-640.
[62] Frost, S. J., Mawad, D., Hook, J., and Lauto, A., 2016, "Micro‐and Nanostructured Biomaterials for Sutureless Tissue Repair," Advanced healthcare materials, 5(4), pp. 401-414.
[63] Drotlef, D. M., Amjadi, M., Yunusa, M., and Sitti, M., 2017, "Bioinspired composite microfibers for skin adhesion and signal amplification of wearable sensors," Advanced Materials, 29(28), p. 1701353.
[64] Park, Y., Shim, J., Jeong, S., Yi, G. R., Chae, H., Bae, J. W., Kim, S. O., and Pang, C., 2017, "Microtopography‐guided conductive patterns of liquid‐driven graphene nanoplatelet networks for stretchable and skin‐conformal sensor array," Advanced Materials, 29(21), p. 1606453.
[65] Tramacere, F., Beccai, L., Kuba, M., Gozzi, A., Bifone, A., and Mazzolai, B., 2013, "The morphology and adhesion mechanism of Octopus vulgaris suckers."
[66] Akerboom, S., Appel, J., Labonte, D., Federle, W., Sprakel, J., and Kamperman, M., 2015, "Enhanced adhesion of bioinspired nanopatterned elastomers via colloidal surface assembly," Journal of the Royal Society, Interface, 12(102), p. 20141061.
[67] Choi, M. K., Park, O. K., Choi, C., Qiao, S., Ghaffari, R., Kim, J., Lee, D. J., Kim, M., Hyun, W., Kim, S. J., Hwang, H. J., Kwon, S. H., Hyeon, T., Lu, N., and Kim, D. H., 2016, "Cephalopod-Inspired Miniaturized Suction Cups for Smart Medical Skin," Adv Healthc Mater, 5(1), pp. 80-87.

[68] Lee, H., Um, D. S., Lee, Y., Lim, S., Kim, H. j., and Ko, H., 2016, "Octopus‐Inspired Smart Adhesive Pads for Transfer Printing of Semiconducting Nanomembranes," Advanced Materials, 28(34), pp. 7457-7465.
[69] Baik, S., Kim, D. W., Park, Y., Lee, T.-J., Ho Bhang, S., and Pang, C., 2017, "A wet-tolerant adhesive patch inspired by protuberances in suction cups of octopi," Nature, 546(7658), pp. 396-400.
[70] Chen, Y. C., and Yang, H., 2017, "Octopus-Inspired Assembly of Nanosucker Arrays for Dry/Wet Adhesion," ACS Nano, 11(6), pp. 5332-5338.
[71] Baik, S., Kim, J., Lee, H. J., Lee, T. H., and Pang, C., 2018, "Highly Adaptable and Biocompatible Octopus‐Like Adhesive Patches with Meniscus‐Controlled Unfoldable 3D Microtips for Underwater Surface and Hairy Skin," Advanced Science, p. 1800100.
[72] Kwak, M. K., Jeong, H. E., and Suh, K. Y., 2011, "Rational design and enhanced biocompatibility of a dry adhesive medical skin patch," Adv Mater, 23(34), pp. 3949-3953.
[73] Arzt, E., Enders, S., and Gorb, S., 2002, "Towards a micromechanical understanding of biological surface devices," Zeitschrift für Metallkunde, 93(5), pp. 345-351.
[74] Jagota, A., and Bennison, S. J., 2002, "Mechanics of adhesion through a fibrillar microstructure," Integrative and Comparative Biology, 42(6), pp. 1140-1145.
[75] Yao, H., and Gao, H., 2006, "Mechanics of robust and releasable adhesion in biology: Bottom-up designed hierarchical structures of gecko," Journal of the Mechanics and Physics of Solids, 54(6), pp. 1120-1146.
[76] Chan, E. P., Greiner, C., Arzt, E., and Crosby, A. J., 2007, "Designing model systems for enhanced adhesion," MRS bulletin, 32(06), pp. 496-503.
[77] Del Campo, A., Greiner, C., and Arzt, E., 2007, "Contact shape controls adhesion of bioinspired fibrillar surfaces," Langmuir, 23(20), pp. 10235-10243.
[78] Radhakrishnan, H., and Mesarovic, S. D., "Adhesive contact of elastic spheres revisited: numerical models and scaling," Proc. Proceedings of the Royal Society of London A: Mathematical, Physical and Engineering Sciences, The Royal Society, pp. 2231-2249.
[79] Kamperman, M., Kroner, E., del Campo, A., McMeeking, R. M., and Arzt, E., 2010, "Functional adhesive surfaces with “gecko” effect: The concept of contact splitting," Advanced Engineering Materials, 12(5), pp. 335-348.
[80] Varenberg, M., Murarash, B., Kligerman, Y., and Gorb, S. N., 2011, "Geometry-controlled adhesion: revisiting the contact splitting hypothesis," Applied Physics A, 103(4), pp. 933-938.
[81] Carbone, G., and Pierro, E., 2012, "Sticky Bio‐inspired Micropillars: Finding the Best Shape," Small, 8(9), pp. 1449-1454.
[82] Koenig, S. P., Boddeti, N. G., Dunn, M. L., and Bunch, J. S., 2011, "Ultrastrong adhesion of graphene membranes," Nat Nanotechnol, 6(9), pp. 543-546.
[83] Gao, W., and Huang, R., 2011, "Effect of surface roughness on adhesion of graphene membranes," Journal of Physics D: Applied Physics, 44(45), p. 452001.
[84] Persson, B., 2003, "On the mechanism of adhesion in biological systems," The Journal of chemical physics, 118(16), pp. 7614-7621.

[85] Persson, B., and Gorb, S., 2003, "The effect of surface roughness on the adhesion of elastic plates with application to biological systems," The Journal of chemical physics, 119(21), pp. 11437-11444.
[86] Scharfenberg, S., Rocklin, D., Chialvo, C., Weaver, R. L., Goldbart, P. M., and Mason, N., 2011, "Probing the mechanical properties of graphene using a corrugated elastic substrate," Applied Physics Letters, 98(9), p. 091908.
[87] Kim, D.-H., Ghaffari, R., Lu, N., and Rogers, J. A., 2012, "Flexible and stretchable electronics for biointegrated devices," Annual review of biomedical engineering, 14, pp. 113-128.
[88] Xu, L., Gutbrod, S. R., Bonifas, A. P., Su, Y., Sulkin, M. S., Lu, N., Chung, H. J., Jang, K. I., Liu, Z., Ying, M., Lu, C., Webb, R. C., Kim, J. S., Laughner, J. I., Cheng, H., Liu, Y., Ameen, A., Jeong, J. W., Kim, G. T., Huang, Y., Efimov, I. R., and Rogers, J. A., 2014, "3D multifunctional integumentary membranes for spatiotemporal cardiac measurements and stimulation across the entire epicardium," Nature Communications, 5, p. 3329.
[89] Yang, S., Chen, Y. C., Nicolini, L., Pasupathy, P., Sacks, J., Becky, S., Yang, R., Daniel, S., Chang, Y. F., Wang, P., Schnyer, D., Neikirk, D., and Lu, N., 2015, "Cut-and-Paste" Manufacture of Multiparametric Epidermal Sensor Systems," Advanced Materials, 27(41), pp. 6423-6430.
[90] Yeo, W. H., Kim, Y. S., Lee, J., Ameen, A., Shi, L., Li, M., Wang, S., Ma, R., Jin, S. H., and Kang, Z., 2013, "Multi‐Functional Electronics: Multifunctional Epidermal Electronics Printed Directly Onto the Skin " Advanced Materials, 25(20), pp. 2772-2772.
[91] Huang, X., Cheng, H., Chen, K., Zhang, Y., Zhang, Y., Liu, Y., Zhu, C., Ouyang, S.-c., Kong, G.-W., Yu, C., Huang, Y., and Rogers, J. A., 2013, "Epidermal Impedance Sensing Sheets for Precision Hydration Assessment and Spatial Mapping," Biomedical Engineering, IEEE Transactions on, 60(10), pp. 2848-2857.
[92] Webb, R. C., Bonifas, A. P., Behnaz, A., Zhang, Y. H., Yu, K. J., Cheng, H. Y., Shi, M. X., Bian, Z. G., Liu, Z. J., Kim, Y. S., Yeo, W. H., Park, J. S., Song, J. Z., Li, Y. H., Huang, Y. G., Gorbach, A. M., and Rogers, J. A., 2013, "Ultrathin conformal devices for precise and continuous thermal characterization of human skin," Nat Mater, 12(10), pp. 938-944.
[93] Choi, S., Park, J., Hyun, W., Kim, J., Kim, J., Lee, Y. B., Song, C., Hwang, H. J., Kim, J. H., Hyeon, T., and Kim, D. H., 2015, "Stretchable Heater Using Ligand-Exchanged Silver Nanowire Nanocomposite for Wearable Articular Thermotherapy," Acs Nano, 9(6), pp. 6626-6633.
[94] Hong, S., Lee, H., Lee, J., Kwon, J., Han, S., Suh, Y. D., Cho, H., Shin, J., Yeo, J., and Ko, S. H., 2015, "Highly Stretchable and Transparent Metal Nanowire Heater for Wearable Electronics Applications," Adv Mater, 27(32), pp. 4744-4751.
[95] Bandodkar, A. J., Molinnus, D., Mirza, O., Guinovart, T., Windmiller, J. R., Valdes-Ramirez, G., Andrade, F. J., Schoning, M. J., and Wang, J., 2014, "Epidermal tattoo potentiometric sodium sensors with wireless signal transduction for continuous non-invasive sweat monitoring," Biosens Bioelectron, 54, pp. 603-609.

[96] Huang, X., Liu, Y. H., Chen, K. L., Shin, W. J., Lu, C. J., Kong, G. W., Patnaik, D., Lee, S. H., Cortes, J. F., and Rogers, J. A., 2014, "Stretchable, Wireless Sensors and Functional Substrates for Epidermal Characterization of Sweat," Small, 10(15), pp. 3083-3090.
[97] Son, D., Lee, J., Qiao, S., Ghaffari, R., Kim, J., Lee, J. E., Song, C., Kim, S. J., Lee, D. J., Jun, S. W., Yang, S., Park, M., Shin, J., Do, K., Lee, M., Kang, K., Hwang, C. S., Lu, N. S., Hyeon, T., and Kim, D. H., 2014, "Multifunctional wearable devices for diagnosis and therapy of movement disorders," Nat Nanotechnol, 9(5), pp. 397-404.
[98] Wagner, T. J., and Vella, D., 2012, "The sensitivity of graphene "snap-through" to substrate geometry," Applied Physics Letters, 100(23), p. 233111.
[99] Carbone, G., and Decuzzi, P., 2004, "Elastic beam over an adhesive wavy foundation," Journal of applied physics, 95(8), pp. 4476-4482.
[100] Qiao, S. T., Gratadour, J. B., Wang, L., and Lu, N. S., 2015, "Conformability of a Thin Elastic Membrane Laminated on a Rigid Substrate With Corrugated Surface," Ieee T Comp Pack Man, 5(9), pp. 1237-1243.
[101] Carbone, G., Mangialardi, L., and Persson, B., 2004, "Adhesion between a thin elastic plate and a hard randomly rough substrate," Physical Review B, 70(12), p. 125407.
[102] Huang, Z. Y., Hong, W., and Suo, Z., 2005, "Nonlinear analyses of wrinkles in a film bonded to a compliant substrate," Journal Of the Mechanics And Physics Of Solids, 53(9), pp. 2101-2118.
[103] Xiao, J., Carlson, A., Liu, Z. J., Huang, Y., and Rogers, J. A., 2010, "Analytical and Experimental Studies of the Mechanics of Deformation in a Solid With a Wavy Surface Profile," Journal of Applied Mechanics, 77(1), p. 011003.
[104] Wang, S. D., Li, M., Wu, J., Kim, D. H., Lu, N. S., Su, Y. W., Kang, Z., Huang, Y. G., and Rogers, J. A., 2012, "Mechanics of Epidermal Electronics," J Appl Mech-T Asme, 79(3), pp. 031022-031022.
[105] Cheng, H., and Wang, S., 2013, "Mechanics of Interfacial Delamination in Epidermal Electronics Systems," Journal of Applied Mechanics, 81(4), pp. 044501-044501.
[106] Dong, W., Xiao, L., Zhu, C., Ye, D., Wang, S., Huang, Y., and Yin, Z., 2017, "Theoretical and experimental study of 2D conformability of stretchable electronics laminated onto skin," Science China Technological Sciences, 60, pp. 1-8.
[107] Xiao, J., Carlson, A., Liu, Z., Huang, Y., Jiang, H., and Rogers, J., 2008, "Stretchable and compressible thin films of stiff materials on compliant wavy substrates," Applied Physics Letters, 93(1), p. 013109.
[108] Johnson, K. L., 1995, "The adhesion of two elastic bodies with slightly wavy surfaces," International Journal of Solids and Structures, 32(3-4), pp. 423-430.
[109] Westergaard, H., 1939, "Bearing Pressures and Crack," Journal of applied mechanics, 66, pp. 49-53.
[110] Koiter, W., 1959, "An infinite row of collinear cracks in an infinite elastic sheet," Archive of Applied Mechanics, 28(1), pp. 168-172.
[111] Zilberman, S., and Persson, B., 2002, "Adhesion between elastic bodies with rough surfaces," Solid state communications, 123(3), pp. 173-177.

[112] Jeong, J. W., Kim, M. K., Cheng, H. Y., Yeo, W. H., Huang, X., Liu, Y. H., Zhang, Y. H., Huang, Y. G., and Rogers, J. A., 2014, "Capacitive Epidermal Electronics for Electrically Safe, Long-Term Electrophysiological Measurements," Adv Healthc Mater, 3(5), pp. 642-648.
[113] Yu, Y. L., Sanchez, D., and Lu, N. S., 2015, "Work of adhesion/separation between soft elastomers of different mixing ratios," J Mater Res, 30(18), pp. 2702-2712.
[114] Scharfenberg, S., Mansukhani, N., Chialvo, C., Weaver, R. L., and Mason, N., 2012, "Observation of a snap-through instability in graphene," Applied Physics Letters, 100(2), p. 021910.
[115] Pailler-Mattei, C., Bec, S., and Zahouani, H., 2008, "In vivo measurements of the elastic mechanical properties of human skin by indentation tests," Medical engineering & physics, 30(5), pp. 599-606.
[116] Tchvialeva, L., Zeng, H., Markhvida, I., McLean, D. I., Lui, H., and Lee, T. K., 2010, "Skin roughness assessment," Domenico Campolo ed., InTech, New Developments in Biomedical Engineering. Vukovar, Croatia., pp. 341-358.
[117] Meitl, M. A., Zhu, Z.-T., Kumar, V., Lee, K. J., Feng, X., Huang, Y. Y., Adesida, I., Nuzzo, R. G., and Rogers, J. A., 2006, "Transfer printing by kinetic control of adhesion to an elastomeric stamp," Nature materials, 5(1), pp. 33-38.
[118] Ameri, S., Ho, R., Jang, H., Wang, Y., Schnyer, D., Akinwande, D., and Lu, N., "Thinnest transparent epidermal sensor system based on graphene," Proc. Electron Devices Meeting (IEDM), 2016 IEEE International, IEEE, pp. 18.14. 11-18.14. 14.
[119] Brennan, C. J., Nguyen, J., Yu, E. T., and Lu, N. S., 2015, "Interface Adhesion between 2D Materials and Elastomers Measured by Buckle Delaminations," Advanced Materials Interfaces, 2(16), p. 1500176.
[120] Wang, L., and Lu, N., 2016, "Conformability of a thin elastic membrane laminated on a soft substrate with slightly wavy surface," Journal of Applied Mechanics, 83(4), p. 041007.
[121] Wang, L., Qiao, S., Ameri, S. K., Jeong, H., and Lu, N., 2017, "A Thin Elastic Membrane Conformed to a Soft and Rough Substrate Subjected to Stretching/Compression," Journal of Applied Mechanics, 84(11), p. 111003.
[122] Singh, A. K., Mehra, D. S., Niyogi, U. K., Sabharwal, S., and Khandal, R. K., 2011, "Polyurethane Based Pressure Sensitive Adhesives (PSAs) Using e-Beam Irradiation for Medical Application," Journal of Polymer Materials, 28(4).
[123] Cilurzo, F., Gennari, C. G., and Minghetti, P., 2012, "Adhesive properties: a critical issue in transdermal patch development," Expert opinion on drug delivery, 9(1), pp. 33-45.
[124] Czech, Z., Wilpiszewska, K., Tyliszczak, B., Jiang, X., Bai, Y., and Shao, L., 2013, "Biodegradable self-adhesive tapes with starch carrier," International Journal of Adhesion and Adhesives, 44, pp. 195-199.
[125] Singh, A. K., Mehra, D. S., Niyogi, U. K., Sabharwal, S., and Singh, G., 2014, "Breathability studies of electron beam curable polyurethane pressure sensitive adhesive for bio-medical application," Radiation Physics and Chemistry, 103, pp. 75-83.
[126] Kawahara, K., and Tojo, K., 2007, "Skin irritation in transdermal drug delivery systems: A strategy for its reduction," Pharmaceutical research, 24(2), p. 399.

[127] Christoffers, W. A., Coenraads, P. J., and Schuttelaar, M. L., 2014, "Bullous allergic reaction caused by colophonium in medical adhesives," Contact dermatitis, 70(4), pp. 256-257.
[128] Autumn, K., Sitti, M., Liang, Y. A., Peattie, A. M., Hansen, W. R., Sponberg, S., Kenny, T. W., Fearing, R., Israelachvili, J. N., and Full, R. J., 2002, "Evidence for van der Waals adhesion in gecko setae," Proceedings of the National Academy of Sciences, 99(19), pp. 12252-12256.
[129] Arzt, E., Gorb, S., and Spolenak, R., 2003, "From micro to nano contacts in biological attachment devices," Proceedings of the National Academy of Sciences, 100(19), pp. 10603-10606.
[130] Gao, H., and Yao, H., 2004, "Shape insensitive optimal adhesion of nanoscale fibrillar structures," Proceedings of the National Academy of Sciences of the United States of America, 101(21), pp. 7851-7856.
[131] Hansen, W. R., and Autumn, K., 2005, "Evidence for self-cleaning in gecko setae," Proc Natl Acad Sci U S A, 102(2), pp. 385-389.
[132] Autumn, K., Majidi, C., Groff, R., Dittmore, A., and Fearing, R., 2006, "Effective elastic modulus of isolated gecko setal arrays," Journal of Experimental Biology, 209(18), pp. 3558-3568.
[133] Kwak, M. K., Pang, C., Jeong, H. E., Kim, H. N., Yoon, H., Jung, H. S., and Suh, K. Y., 2011, "Towards the Next Level of Bioinspired Dry Adhesives: New Designs and Applications," Advanced Functional Materials, 21(19), pp. 3606-3616.
[134] Greiner, C., Arzt, E., and del Campo, A., 2009, "Hierarchical Gecko‐Like Adhesives," Advanced Materials, 21(4), pp. 479-482.
[135] del Campo, A., Greiner, C., Álvarez, I., and Arzt, E., 2007, "Patterned surfaces with pillars with controlled 3 D tip geometry mimicking bioattachment devices," Advanced Materials, 19(15), pp. 1973-1977.
[136] Murphy, M. P., Aksak, B., and Sitti, M., 2009, "Gecko‐Inspired Directional and Controllable Adhesion," Small, 5(2), pp. 170-175.
[137] Wang, Y., Hu, H., Shao, J., and Ding, Y., 2014, "Fabrication of well-defined mushroom-shaped structures for biomimetic dry adhesive by conventional photolithography and molding," ACS Appl Mater Interfaces, 6(4), pp. 2213-2218.
[138] Pease, R., 1981, "Electron beam lithography," Contemporary Physics, 22(3), pp. 265-290.
[139] Vieu, C., Carcenac, F., Pepin, A., Chen, Y., Mejias, M., Lebib, A., Manin-Ferlazzo, L., Couraud, L., and Launois, H., 2000, "Electron beam lithography: resolution limits and applications," Applied surface science, 164(1-4), pp. 111-117.
[140] Becker, H., and Heim, U., 2000, "Hot embossing as a method for the fabrication of polymer high aspect ratio structures," Sensors and Actuators A: Physical, 83(1), pp. 130-135.
[141] Del Campo, A., and Arzt, E., 2007, "Design parameters and current fabrication approaches for developing bioinspired dry adhesives," Macromolecular bioscience, 7(2), pp. 118-127.

[142] Carbone, G., Pierro, E., and Gorb, S. N., 2011, "Origin of the superior adhesive performance of mushroom-shaped microstructured surfaces," Soft Matter, 7(12), pp. 5545-5552.
[143] Marvi, H., Song, S., and Sitti, M., 2015, "Experimental investigation of optimal adhesion of mushroomlike elastomer microfibrillar adhesives," Langmuir, 31(37), pp. 10119-10124.
[144] Kim, T., Park, J., Sohn, J., Cho, D., and Jeon, S., 2016, "Bioinspired, Highly Stretchable, and Conductive Dry Adhesives Based on 1D-2D Hybrid Carbon Nanocomposites for All-in-One ECG Electrodes," Acs Nano, 10(4), pp. 4770-4778.
[145] Mannsfeld, S. C., Tee, B. C., Stoltenberg, R. M., Chen, C. V. H., Barman, S., Muir, B. V., Sokolov, A. N., Reese, C., and Bao, Z., 2010, "Highly sensitive flexible pressure sensors with microstructured rubber dielectric layers," Nature materials, 9(10), p. 859.
[146] Schwartz, G., Tee, B. C.-K., Mei, J., Appleton, A. L., Kim, D. H., Wang, H., and Bao, Z., 2013, "Flexible polymer transistors with high pressure sensitivity for application in electronic skin and health monitoring," Nature communications, 4, p. 1859.
[147] Buhl, S., Greiner, C., Campo, A. d., and Arzt, E., 2009, "Humidity influence on the adhesion of biomimetic fibrillar surfaces," International Journal of Materials Research, 100(8), pp. 1119-1126.
[148] Cadirov, N., Booth, J. A., Turner, K. L., and Israelachvili, J. N., 2017, "Influence of Humidity on Grip and Release Adhesion Mechanisms for Gecko-Inspired Microfibrillar Surfaces," ACS Applied Materials & Interfaces, 9(16), pp. 14497-14505.
[149] Pesika, N. S., Zeng, H., Kristiansen, K., Zhao, B., Tian, Y., Autumn, K., and Israelachvili, J., 2009, "Gecko adhesion pad: a smart surface?," Journal of Physics: Condensed Matter, 21(46), p. 464132.
[150] Cadirov, N., Booth, J. A., Turner, K. L., and Israelachvili, J. N., 2017, "Influence of Humidity on Grip and Release Adhesion Mechanisms for Gecko-Inspired Microfibrillar Surfaces," ACS Appl Mater Interfaces, 9(16), pp. 14497-14505.
[151] Smith, A. M., 1991, "Negative pressure generated by octopus suckers: a study of the tensile strength of water in nature," Journal of Experimental Biology, 157(1), pp. 257-271.
[152] Kier, W. M., and Smith, A. M., 2002, "The structure and adhesive mechanism of octopus suckers," Integrative and Comparative Biology, 42(6), pp. 1146-1153.
[153] Von Byern, J., and Klepal, W., 2006, "Adhesive mechanisms in cephalopods: a review," Biofouling, 22(5), pp. 329-338.
[154] Tramacere, F., Kovalev, A., Kleinteich, T., Gorb, S. N., and Mazzolai, B., 2014, "Structure and mechanical properties of Octopus vulgaris suckers," Journal of the Royal Society, Interface, 11(91), p. 20130816.
[155] Smith, A., 1996, "Cephalopod sucker design and the physical limits to negative pressure," Journal of Experimental Biology, 199(4), pp. 949-958.
[156] Nanni, G., Fragouli, D., Ceseracciu, L., and Athanassiou, A., 2015, "Adhesion of elastomeric surfaces structured with micro-dimples," Applied Surface Science, 326, pp. 145-150.

[157] Baik, S., Park, Y., Lee, T.-J., Bhang, S. H., and Pang, C., 2017, "A wet-tolerant adhesive patch inspired by protuberances in suction cups of octopi," Nature, 546(7658), pp. 396-400.
[158] Chen, Y.-C., and Yang, H., 2017, "Octopus-inspired assembly of nanosucker arrays for dry/wet adhesion," ACS nano, 11(6), pp. 5332-5338.
[159] Spolenak, R., Gorb, S., Gao, H., and Arzt, E., "Effects of contact shape on the scaling of biological attachments," Proc. Proceedings of the Royal Society of London A: Mathematical, Physical and Engineering Sciences, The Royal Society, pp. 305-319.
[160] Gao, H., Wang, X., Yao, H., Gorb, S., and Arzt, E., 2005, "Mechanics of hierarchical adhesion structures of geckos," Mechanics of Materials, 37(2-3), pp. 275-285.
[161] Yao, H., and Gao, H., 2006, "Mechanics of robust and releasable adhesion in biology: Bottom–up designed hierarchical structures of gecko," Journal of the Mechanics and Physics of Solids, 54(6), pp. 1120-1146.
[162] Mantriota, G., and Messina, A., 2011, "Theoretical and experimental study of the performance of flat suction cups in the presence of tangential loads," Mechanism and machine theory, 46(5), pp. 607-617.
[163] Liu, J., Tanaka, K., Bao, L., and Yamaura, I., 2006, "Analytical modelling of suction cups used for window-cleaning robots," Vacuum, 80(6), pp. 593-598.
[164] Chang, W.-Y., Wu, Y., and Chung, Y.-C., 2014, "Facile fabrication of ordered nanostructures from protruding nanoballs to recessional nanosuckers via solvent treatment on covered nanosphere assembled monolayers," Nano letters, 14(3), pp. 1546-1550.
[165] Choi, M. K., Park, O. K., Choi, C., Qiao, S., Ghaffari, R., Kim, J., Lee, D. J., Kim, M., Hyun, W., Kim, S. J., Hwang, H. J., Kwon, S.-H., Hyeon, T., Lu, N., and Kim, D.-H., 2016, "Cephalopod-Inspired Miniaturized Suction Cups for Smart Medical Skin," Advanced Healthcare Materials, 5(1), pp. 80-87.
[166] Akerboom, S., Appel, J., Labonte, D., Federle, W., Sprakel, J., and Kamperman, M., 2015, "Enhanced adhesion of bioinspired nanopatterned elastomers via colloidal surface assembly," Journal of The Royal Society Interface, 12(102).
[167] Afferrante, L., Carbone, G., Demelio, G., and Pugno, N., 2013, "Adhesion of Elastic Thin Films: Double Peeling of Tapes Versus Axisymmetric Peeling of Membranes," Tribology Letters, 52(3), pp. 439-447.
[168] Tramacere, F., Pugno, N. M., Kuba, M. J., and Mazzolai, B., 2015, "Unveiling the morphology of the acetabulum in octopus suckers and its role in attachment," Interface focus, 5(1), p. 20140050.
[169] Ge, D., Matsuno, T., Sun, Y., Ren, C., Tang, Y., and Ma, S., 2015, "Quantitative study on the attachment and detachment of a passive suction cup," Vacuum, 116, pp. 13-20.
[170] Lötters, J., Olthuis, W., Veltink, P., and Bergveld, P., 1997, "The mechanical properties of the rubber elastic polymer polydimethylsiloxane for sensor applications," Journal of Micromechanics and Microengineering, 7(3), p. 145.
[171] Brandrup, J., Immergut, E. H., Grulke, E. A., Abe, A., and Bloch, D. R., 1989, Polymer handbook, Wiley New York etc.

[172] Eshelby, J. D., 1957, "The Determination of the Elastic Field of an Ellipsoidal Inclusion, and Related Problems," Proceedings of the Royal Society of London. Series A. Mathematical and Physical Sciences, 241(1226), pp. 376-396.
[173] Liu, J.-L., and Feng, X.-Q., 2012, "On elastocapillarity: A review," Acta Mechanica Sinica, 28(4), pp. 928-940.
[174] Roman, B., and Bico, J., 2010, "Elasto-capillarity: deforming an elastic structure with a liquid droplet," J. Phys.: Condens. Matter, 22, p. 493110.
[175] Hui, C.-Y., and Jagota, A., 2013, "Surface tension, surface energy, and chemical potential due to their difference," Langmuir, 29(36), pp. 11310-11316.
[176] Henann, D. L., and Anand, L., 2010, "Surface tension-driven shape-recovery of micro/nanometer-scale surface features in a Pt 57.5 Ni 5.3 Cu 14.7 P 22.5 metallic glass in the supercooled liquid region: a numerical modeling capability," Journal of the Mechanics and Physics of Solids, 58(11), pp. 1947-1962.
[177] Huang, J., Mazzara, J., Schwendeman, S., and Thouless, M., 2015, "Self-healing of pores in PLGAs," Journal of Controlled Release, 206, pp. 20-29.
[178] Wu, S., 1971, "Calculation of interfacial tension in ploymer systems," J . Polym. Sci., C Polym. Symp., 34(1), pp. 19-31.
[179] Roe, R.-J., 1965, "Parachor and surface tension of amorphous polymers," The Journal of Physical Chemistry, 69(8), pp. 2809-2810.
[180] Qiao, S., Wang, L., Jeong, H., Gregory, J., Rodin, and Lu, N., 2017, "Suction effects in cratered surfaces," J. R. Soc. Interface
[181] Mancarella, F., Style, R. W., and Wettlaufer, J. S., 2016, "Interfacial tension and a three-phase generalized self-consistent theory of non-dilute soft composite solids," Soft matter, 12(10), pp. 2744-2750.
[182] Style, R. W., Wettlaufer, J. S., and Dufresne, E. R., 2015, "Surface tension and the mechanics of liquid inclusions in compliant solids," Soft Matter, 11(4), pp. 672-679.
[183] Yang, F., 2004, "Size-dependent effective modulus of elastic composite materials: spherical nanocavities at dilute concentrations," Journal of Applied Physics, 95(7), pp. 3516-3520.
[184] Lur′e, A. I., 1964, Three-dimensional problems of the theory of elasticity, Interscience Publishers.
[185] Zhu, J., Li, T., Cai, S., and Suo, Z., 2011, "Snap-through expansion of a gas bubble in an elastomer," The Journal of Adhesion, 87(5), pp. 466-481.
[186] Henann, D. L., and Bertoldi, K., 2014, "Modeling of elasto-capillary phenomena," Soft Matter, 10(5), pp. 709-717.
[187] Zimmermann, J., and Stommel, M., 2013, "The mechanical behaviour of rubber under hydrostatic compression and the effect on the results of finite element analyses," Archive of Applied Mechanics, 83(2), pp. 293-302.
[188] Wang, L., Qiao, S., and Lu, N., 2017, "Effects of surface tension on the suction forces generated by miniature craters," Extreme Mechanics Letters, 15, pp. 130-138.
[189] Qiao, S., Wang, L., Jeong, H., Rodin, G. J., and Lu, N., 2017, "Suction effects in cratered surfaces," Journal of The Royal Society Interface, 14(135), p. 20170377.